Durham E-Theses

Proton - proton scattering at high energies

Ali Hayaar Shehadeh

How to cite:

Shehadeh, Ali Hayaar (1976) Proton - proton scattering at high energies. Masters thesis, Durham University.

Use policy

The full-text may be used and/or reproduced, and given to third parties in any format or medium, without prior permission or charge, for personal research or study, educational, or not-for-profit purposes provided that:

- a full bibliographic reference is made to the original source
- a https://etheses.durham.ac.uk/id/eprint/9013/ is made to the metadata record in Durham E-Theses
- the full-text is not changed in any way

The full-text must not be sold in any format or medium without the formal permission of the copyright holders.

Please consult the full Durham E-Theses policy for further details.

Academic Support Office, The Palatine Centre, Durham University, Stockton Road, Durham, DH1 3LE
e-mail: e-theses.admin@durham.ac.uk Tel: +44 0191 334 6107
https://etheses.durham.ac.uk

PROTON - PROTON SCATTERING
AT
HIGH ENERGIES

by

Ali Haydar Shehadeh

The copyright of this thesis rests with the author.
No quotation from it should be published without
his prior written consent and information derived
from it should be acknowledged.

DURHAM UNIVERSITY
SCIENCE
15 APR 1976
SECTION
LIBRARY

Thesis submitted for the Degree of Master of Science in the University of Durham, February 1976.

PREFACE

The work presented in this thesis was carried out in the Department of Mathematics, University of Durham, under the supervision of Professor E.J. Squires to whom I would like to express my deep gratitude for continuous guidance, encouragement and help.

My sincere thanks are also due to all the people in this department for their different sorts of help, and for the brotherly atmosphere; in particular to Dr. W.J. Zakrzewski, Mr. G.T. Fairley, Mr. S.K.A.S. Yagoobi and Mr. M. Sarbishaei for discussions and help.

Lastly, I thank my parents and my family for all the opportunities they have given me, their continued interest and encouragement throughout my academic career.

ABSTRACT

This thesis deals with various aspects of proton-pronton scattering at high energies, in particular the recent CERN-ISR results.

In chapter one, first we discuss briefly the experimental situation of the total cross-sections and elastic scattering of hadrons on protons up to NAL energies. Then we give a general review of the methods which have been used for the determination of the total cross-section in the ISR. The main experimental features are summarized at the end of this chapter.

The results of chapter one motivated a new interest in asymptotic theorems. In chapter two we discuss some theoretical aspects which are model independent, and some physical predictions in the presence of an asymptotic growth of σ_t .

Chapter three is concerned with fitting the data with a variety of Regge pole and cut models. We consider various eikonal-type prescription for the cut strength.

In chapters four and five we re-examine the data using two phenomenlogical models; namely : the overlap function model and the geometrical scaling model, using mainly impact parameter language. It will turn out that geometrical scaling hypothesis can describe the main qualitative features of present data.

A number of interpretations have been proposed to explain the rise of σ_t in the ISR energy range. In chapter six we consider the question of the rising cross-section. We discuss two mechanisms proposed to explain the rise of σ_t , where in both mechanisms the rise of σ_t in the ISR energy range is interpreted as a threshold effect. Finally we end this work by examining the rise of σ_t in impact parameter space.

CONTENTS

Page

CHAPTER I Total cross-sections and elastic scattering at high energies 1

I.I Total cross-sections of hadrons on protons and elastic scattering. 1

1.2 Measurements of proton-proton total cross-sections at I.S.R. 2

1.3 Summary of I.S.R. results on proton-proton elastic scattering. 9

CHAPTER II Theoretical aspects of proton-proton scattering. 11

II.1 Bounds 11

II.1.1 Froissart bound 11

II.1.2 MacDowell-Martin bound 12

II.2 Physical predictions 12

II.3 Proton-proton absorption at ISR and Black disc. 14

CHAPTER III The pomeron in proton-proton scattering. 19

III.1 The data, α_{eff}. 20

III.2 A Regge pole model. 22

III.3 Regge cut models 24

III.4 Conclusions and Remarks. 30

CHAPTER IV Overlap function model 33

IV.1 S-channel unitarity relation 33

IV.2 Inelastic overlap function in momentum space. 36

IV.3 Inelastic overlap function in impact parameter space. 37

IV.4 Impact structure of inelastic diffraction. 40

IV.5 Summary and conclusions. 43

CHAPTER V Geometrical scaling in proton-proton scattering 45

V.1 Scaling law for the elastic differential cross-section in proton-proton scattering. 46

V.2 Further comparisons and tests. 49

V.3 The influence of the real part "Kroll's modification". 53

CHAPTER VI The origin of the rising cross-section 56

VI.1 Rising cross-section and triple pomeron 56

VI.2 Rising cross-section and $N\bar{N}$ production. 63

VI.3 Rising cross-section in impact parameter space. 67

VI.4 Conclusion 70

REFERENCES 72

TABLE AND FIGURE CAPTIONS 75

Tables 80

Figures 82

CHAPTER ONE

Total cr.ss. and elastic scattering at high energies

The plan of this chapter is as follows:-

1. Total cr.ss. of hadrons on proton and elastic scattering
2. Measurements of proton - proton total cr.s. at ISR
3. Summary of ISR results on p-p elastic scattering

1.1 Total cr.ss. of hadrons on proton.

The experimental situation on the energy dependence of the total cr.ss. of $\pi^{\pm}$, $K^{\pm}$, $P^{\pm}$ on P up to (SP) energies may be summarized as follows:-

(i) The $\pi^{\pm}$P, K^-P, PP total cr.ss. seem to have reached some kind of a plateau with little or no energy dependence.

(ii) The $\bar{p}$p cr.s. is decreasing while

(iii) K^+P cr.s. is increasing with energy.

But in the past few years with the advent of ISR facilities at CERN and the preliminary operation of the NAL 400 Gev machine, the horizon of high energy hadronic scattering have widened dramatically. In fact only (pp) cr.s. measured at extreme energies, this energy is available from the ISR where up to 30 Gev protons collide in their overall center of mass

$$\underset{30\ \text{Gev}}{\xrightarrow{\quad P1 \quad}} \quad \underset{30\ \text{Gev}}{\xleftarrow{\quad P2 \quad}} \qquad\qquad \underset{400\text{Gev}}{\xrightarrow{\qquad\qquad}} \bullet$$

$$S = (P_1+P_2) = (E_1+E_2) = 3600\ \text{Gev}^2 \qquad S = (1+400)^2 - (400)^2 \simeq 800\ \text{Gev}^2$$

ISR NAL

DURHAM UNIVERSITY
SCIENCE
15 APR 1976
SECTION

The results from ISR (which will be discussed in detail in Section 2) demonstrate that (pp) cr.ss. are rising in that energy range, the effect was found to be big, of the order 10% for an increase in energy by a factor of about 2.5 ($\sqrt{s}=23 \rightarrow \sqrt{s}=53$).

New data from NAL extend the measurements for the other five charge particles. All cr.ss. show a rise (Fig. 1) with the exception of the $\bar{p}p$ cr.s. which however doesn't decrease any more and has become flat at the highest NAL energy. These measurements demonstrate that rising cr.ss. is a general high energy phenomenon.

The fact that K^+P cr.s. demonstrate this phenomenon at the lowest energy is propably related to the fact that it is cr.s. is the smallest one, and suggest that the rising component is present at all energies but can reveal itself only when the Regge type terms $\sim E^{-\alpha}$ have become very small.

Finally, the difference of particle and antiparticle cr.ss. ($\Delta\sigma$) are shown in (Fig. 2)(1) demonstrating that $\Delta\sigma$ approaches Zero, approximately as $S^{-\frac{1}{2}}$, in agreement with Regge analysis, and pomeranchuk theorm.

1.2 Elastic Scattering

A collaboration of Michigan-ANL-FNAL-Indiana(2) has measured diffraction scattering at 100 and 200 Gev/c for all six changed particles up to $|t| \leqslant 1 \mathrm{Gev/c}^2$. In (Fig. 3) the various cr.ss. are superimposed, normalized to each other at t=0. The data have been fitted to an exponential behaviour in t over the t range $(0{\cdot}07 \leqslant |t| \leqslant 0.3)\ \mathrm{Gev}^2$ and the resulting slopes are shown in (Fig. 4) in combination with data at lower energies, fitted over the same t range. A rising slope is apparent for all particles except the antiproton. The antiproton is still expanding it's diffraction pattern but it's slope is approaching the proton slope, while the other five particles all show a shrinking diffraction pattern especially the exotic K^+P and PP reactions.

Recently (1975)$^{(3)}$ differential cr.ss. have been measured at Fermilab for $\pi^{\pm}P$, $K^{\pm}P$, and $P^{\pm}P$ elastic sca. at 50,70,100, 140, and 175 Gev/C incident momentum over the $|t|$ range 0.03 to 0.8 Gev^2, the results cannot be fit with a simple exponential, but maybe represented by

$$\frac{d\sigma}{dt} = A \exp(Bt + ct^2) \qquad (1)$$

This form gives a good representation of the data and a typical set of fits in show in Fig (5). The logarithmic slope b(t) is given by

$$b\,(|t|) = \frac{d}{dt}\left(\ln \frac{d\sigma}{dt}\right) = B - 2C\,|t| \qquad (2)$$

Fig. (6) shows these Logarithmic slopes at $|t| = 0.2\ Gev^2$ as a function of S. These values of b(0.2) connect smoothly to previous results at other energies. The $\pi^{\pm}$ and k^- slopes show little energy dependence, while the K^+ and proton slopes are gradually increasing.

2. Measurements of P-P total cr.s. at ISR

The experimental evidence for the rise of the p-p total cr.s. at ISR seems to be very strong and unquestionable. This general opinion stems from the fact that three different methods used for determination of the σ_t gave very consistent result.

In one method σ_t is obtained from the measurement of the differential elastic-scattering cr.s. by application of the optical theorm, in another the total number of p-p interactions is counted. In applying the first method two different approaches have been used to fix the absolute scale of the elastic cr.s. (a) measurement of the elastic cr.s. at very small momentum transfere where conlomh scattering is dominant and known in absolute value. (b) and determination of the machine Luminosity by the Van deer Meer Method.

(i) measurements of p-p total cr.s. by means of the coulomb scattering p-p elastic scattering have been measured$^{(4)}$ in the Coulomb-Nuclear interference region ($0.001 \leqslant |t| \leqslant 0.015$) for beam momentum of (11.8 + 11.8) and (15.4 + 15.4) Gev/c. In this experiment the elastic scattering rate N(t) was fitted to the formula.

$$N(t) \propto \frac{d\sigma}{dt} = \pi\, | f_c + f_m |^2 \qquad (3)$$

where f_c and f_n are the coulomb and the nuclear amplitudes respectively, the coulomb amplitude f_c is given by $f_c = -2\alpha \frac{G^2(t)}{|t|} \exp\left(i\alpha\phi\right)$ (4)

where α = fine structure constant $\simeq \frac{1}{137}$

$\alpha\phi$ = phase of coulomb amplitude $\simeq \alpha(\ln \frac{0.08}{|t|} - 0.577) \simeq 0.025$

$G(t)$ = proton form factor $\simeq (1-2.81|t|)$

while for the nuclear amplitude the familiar form

$$f_n = \frac{\sigma_t}{4\pi} (\rho + i) \exp(\tfrac{1}{2}bt) \quad (5)$$ was used

Then eq. (3) becomes

$$N(t) = K \left[\underbrace{\left(\frac{2\alpha}{t} \right)^2 G^4(t)}_{\text{Coulomb}} - \underbrace{(\rho+\alpha\phi)\frac{2\alpha}{\pi}\sigma_t \frac{G^2(t)}{|t|} \exp(\tfrac{1}{2}bt)}_{\text{C-N}} + \underbrace{\left(\frac{\sigma_t}{4\pi}\right)^2 (1+\rho^2) \exp(bt)}_{\text{Nuclear}} \right] (6)$$

From eq.(6) we can see that for $\sigma_t \simeq 40$ mb, the Coulomb and nuclear amplitude are equal for $\theta_c \simeq \frac{42}{P}$ (P is ISR momenta), At P = 15 Gev/c, $\theta_c \simeq 3$ mrad which corresponds to a displacement of the scattering proton 3 cm from the beam axis at the end of the ISR 10m long straight sections. So in order to enter considerably in coulomb region, we have to detect protons closer to the beam more than 3cm. (Fig. (7) shows a general layout of experimental apparatus used to detect particles scattered in the vertical plane.

Before discussing the results of this method, we have to note an important remark concerning eq. (4). In fact this eq. involves three assumptions:

(a) Spin dependent effects are negligible.

(b) The imaginary part of N-amplitude depends exponentially on the momentum transfere in the small $|t|$ region $|t| \leqslant 0.015$ Gev^2

(c) The real and the Imaginary parts have the same t dependence thus ρ is independent of momentum transfere.

The validity of assumption (a) may be justified as follows, experiments at lower energies have shown that spin-dependent effects, are small already at 1.5 Gev/c and the current picture of high energy, strong interaction renders very implasuible the increase of spin effects with energy, assumption (b) is consistent with previous measurements, however the validity of this assumption has been recently questioned. Assumption (c) is consistent with result at lower energies, moreover ρ is very small thus the experiment is not sensitive to it's (t) dependence.

Fig(8) shows two angular distribution in the Coulomb-Nuclear interference region at 11.8 and 15.4 Gev/c. The solid lines indicate the differential cross. obtained by using the best fit for σ_t and ρ, while the dashed lines indicate the separate contributions of Coulomb and Nuclear amplitude.

The values of σ_t and ρ as a result of the overall fits to the data at each energy are shown in the table below (table 1)

ISR momentum Gev/c	equ.Lab. momentum Gev/c	σ_t	ρ
11.8	290	38.9 ± 0.7	$+0.02 \pm 0.05$
15.4	500	40.2 ± 0.8	$+0.03 \pm 0.06$

In the fit three parameters, σ_t , ρ, and K in eq.(6) were left as a free parameter, while the slope b was taken from previous measurements, since the present experiment doesn't cover a wide enough -t- range to permit an accurate determination of b.

In Fig (9) the values of ρ obtained in this experiment were plotted together with data at lower energies, the ratios ρ were found to be slightly positive (Table 1), the analysis of all high energy data from IHEP, Fermilab, and ISR indicates that ρ goes from negative tc positive values, crossing zero at about (280 ± 60) Gev/c

(ii) In this method(7) the total p-p cr.ss. have been obtained by measuring elastic scattering at angles around 6 mrad at c.m energies of 23, 31, 45, 63 Gev, and by applying the optical theorm. The steps of the procedure are the following.

(a) measuring the elastic differential rate $\frac{\Delta R_{el}}{\Delta \Omega}$, in a known solid angle $\Delta \Omega$ and in the vertical plane around $\theta = 6$ mrad, which corresponds to a momentum transfere $t = p^2 \theta^2$ (p is ISR Momentum)

(b) Determination of the elastic differential cr.ss. by means of the Luminosity using Van der Meer method

$$\frac{d\sigma}{d\Omega} = \frac{1}{L} \frac{\Delta R_{el}}{\Delta \Omega} \qquad (7)$$

(c) having obtained the elastic differential cr.ss. at angles 6 mrad, the Coulomb contribution which varied from ~ 5% at (11.8 + 11.8) Gev/c to 0.2% at (26.6 + 26.6) Gev/c, was subtracted, and the extrapolation of the nuclear scattering differential cr.s.

$$\frac{d\sigma}{dt} = \frac{\pi}{p^2} \frac{d\sigma}{d\Omega} \qquad (8)$$

to the forward direction was performed using the formula

$$\frac{d\sigma}{dt} = \left(\frac{d\sigma}{dt}\right)_{t=0} e^{bt} \qquad (9)$$

(d) Application of the optical Theorm

$$\sigma_t = \frac{4\pi}{p} \frac{1}{\sqrt{1+\rho^2}} \sqrt{\left(\frac{d\sigma}{d\Omega}\right)_{t=0}} = \frac{4\pi}{p} \frac{1}{\sqrt{1+\rho^2}} \frac{1}{\sqrt{L}} \sqrt{\frac{\Delta R_{el}}{\Delta \Omega}\, \varepsilon} \qquad (10)$$

where

$$\varepsilon = e^{b|t|}$$

The ratio ρ has been previously measured (by method i) and the average value between $\sqrt{s} = 23$ and $\sqrt{s} = 31$ Gev was found to be -0.025 ± 0.035, since the value is compatable with zero, this value has been assumed in eq. (10). Also the effect of a sizeable real part on σ_t is very small, for $-0.5 \leqslant \rho \leqslant 0.2$ one has variation of σ_t with $|\Delta\sigma_t| \leqslant 0.2$mb which is much smaller than the errors quoted in table (2). (see next page)

This method has been applied at the four standard ISR energies with the results collected in the table (2).

The main conclusion of this experiment is that the p-p total cr.s. increases by about $\Delta\sigma_t = (4.1 \pm 0.7)$ mb in ISR energy range. The present ISR data alone may be fitted by a linear increase with $\ln s$, on the other hand Fig. (10) indicate that σ_t goes through a shallow minimum around $S_o = 200$ Gev^2 where $\sigma_t = \sigma_c = (38.4 \pm 0.3)$ mb Thus over a wider energy range $100 \leqslant s \leqslant 2800$ Gev^2 the data can be fit to the expression $\sigma = \sigma_c + \sigma_1 \left(\ln \frac{s}{s_o}\right)^{\nu}$ (11) where $\sigma_1 = (0.9 \pm 0.3)$ mb, $\nu = 1.8 \pm 0.4$, such an increase of σ_t with energy agrees, within a large errors and over this energy range with the Froissart limit $\nu = 2$, which corresponds to the maximum rate of interactions allowed by unitarity.

(iii) The pisa-stony$^{(9)}$ Brook collaboration has measured the total interaction rate R_t and obtained directly the total cr.s. by using the Luminosity measured with the Van der Meer method.

$$\sigma_t = \frac{R_t}{L} \qquad (12)$$

The values σ_t obtained by methods (i), (ii), and (iii) are plotted together in Fig. (10). The agreement between the sets of data is very good.

Let us finally mention to a new method for measuring σ_t by simultaneously measuring the total collision rate (method iii) and the elastic scattering differential cr. s. in the diffraction

TABLE (2)

Elastic differential and total cr.ss. measured by the CERN-Roma Collaboration (7)

$\sqrt{s}$ Gev	t $Gev^2 \times 10^{-3}$	$d\sigma/dt$ mb/Gev^2	b* Gev^{-2}	b/t/ $\varepsilon = e$	$(d\sigma/dt)_{t=0}$ mb/Gev^2	σ_t mb	** σ_{el} mb	$\sigma_{in} = \sigma_t - \sigma_{el}$ mb
23.4	8.1	71.0 ± 1.5	11.8	1.10±0.004	78.1±1.7	39.1±0.4	6.8±0.2	32.3±0.4
30.5	13.5	71.0 ± 1.6	12.3	1.18±0.007	83.8±1.9	40.5±0.5	7.0±0.2	33.5± 0.4
44.8	17.5	73.8 ± 1.7	12.8	1.25±0.010	92.3±2.2	42.5±0.5	7.5±0.3	35.0± 0.5
52.8	23.0	70.6 ± 1.8	13.1	1.35±0.014	95.4±2.6	43.2±0.6	7.6±0.3	35.6± 0.5

* The values of (b) used in eq. (10) and shown in table (2) were obtained from previous measurement,(8) taken together with new values obtained at $\sqrt{s}$ = 45 Gev and $\sqrt{s}$ = 53 Gev with the apparatus described in method (i).

** The elastic cr.ss. were computed using the extrapolated values of the forward cr.s. with the qouted slopes for $|t| \leqslant 0.1$ Gev^2, and an exponential behaviour of smaller slopes for $|t| \geqslant 0.1$ Gev^2, as measured by Barbiellini et al (8).

region (method ii) one has by eliminating L between eq. (12) and eq. (10).

$$\sigma_t = \left(\frac{4\pi}{p}\right)^2 \frac{\varepsilon\,(\Delta R_{el}/\Delta\Omega)}{R_t} \qquad (13)$$

In this case the measurement of σ_t does not depend on the luminosity of the ISR, thus removing one of the largest uncertainties on the cr.s. measurement. The results of this fourth method confirm the previous measurements.

3. Summary of ISR results on p-p elastic scattering

Fig. (11) shows pp elastic scattering data at large momentum transfere from ISR (8) together with some lower energy points. The qualitative experimental properties of pp scattering data over the ISR energy range can be summarized as follows:-

(a) shrinking forward peak

The slope parameter $B_0 \equiv \frac{d\sigma}{dt}\left(\ln \frac{d\sigma}{dt}\right)_{t=0}$ rises by about 10% in the ISR energy range.

(b) $\ln \frac{d\sigma}{dt}$ has concave curvature for $|t| \simeq 0.15$ Gev^2

So that at the highest ISR energy the slope equals (13.1 ± 0.3) Gev^{-2} for $(0.01 \leqslant |t| \leqslant 0.15)$ and $(10.8 \pm 0.2$ Gev^{-2} for $0.17 \leqslant |t| \leqslant 0.31$

(c) Diffraction minima in $\frac{d\sigma}{dt}$ at $t = -1.4$

The differential elastic cr.s. shows a clear minimum at $|t| \simeq 1.4$ Gev^2. In ISR interval the position of the minimum displaced by (0.08 ± 0.11) Gev^2 towards smaller momentum transfere, passing from (1.45 ± 0.10) Gev^2 at $\sqrt{s} = 31$ Gev to (1.37 ± 0.03) Gev^2 at $\sqrt{s} = 53$ Gev.

(d) The real part of the nuclear amplitude in the forward direction is very small ($\rho = \mathrm{Re}/\mathrm{Im} = 0.025 \pm 0.035$) for $23 \leqslant \sqrt{s} \leqslant 31$ Gev

(e) The total cr.s. increase by about (10 ± 2) % in the ISR energy range.

(f) The elastic cr.s. increase by (12 ± 4)%, if 10% increase of the forward slope is assumed. Indeed one has (apart from small corrections due to (b)) $\sigma_{el} \sim \frac{\sigma_t^2}{b}$, so that a slower increase if b with energy implies a faster increase of σ_{el}.

(g) $\sigma_{inelastic} = \sigma_t - \sigma_{el}$ increases by about 10% passing from (32 ± 0.4) to (35 ± 0.5) mb.

(h) Constant cr.ss. and slope ratios

$$\frac{\sigma_{el}}{\sigma_t} \simeq 0.175 \, , \qquad \frac{B_0}{\sigma_t} \simeq 6.296 \qquad \text{Gev}^2/\text{mb}$$

independent of s.

CHAPTER TWO

Theoretical aspects of p-p scattering

The recent results from ISR (I) and the suggestion of a possible $(\ell n\, s)^2$ growth of σ_t (eq (11) - I) motivated a new interest in asymptotic theorems, and models which saturate the Froissart bound. In the first section of this chapter we recall the Froissart bound and the MacDowell-Martin bound, in the second one we give some physical predictions in presence of an asymptotic growth of σ_t, and finally we study in section 3 the p-p absorption at ISR.

I. Bounds

(1.1) Froissart bound

Starting from the existence$^{(11)}$ of a cut off in the partial wave series (Lukaszuk & Martin 1967)

$$L_{max} = \frac{k}{2m_\pi} \,\mathrm{Log}\; s \qquad (1)$$

and using for σ_t the formula

$$\sigma_t = \frac{4\pi}{k^2} \sum_{0}^{L_{max}} (2\ell+1)\, \mathrm{Im}\; f_\ell(s,0) \qquad (2)$$

Since Im f_ℓ is constrained to the range $\quad 0 \leqslant \mathrm{Im}\; f_\ell \leqslant 1$

eq (2) becomes
$$\sigma_t \leqslant \frac{4\pi}{k^2} \sum_{0}^{L_{max}} (2\ell+1) \qquad (3)$$

We find the Froissar t bound

$$\sigma_t \leqslant \frac{\pi}{m_\pi^2} \quad (\mathrm{Log}\; s)^2 \qquad (4)$$

The factor $\frac{\pi}{m_\pi^2}$ is of the order of 60 mb, which is two order of magnitude greater than the coefficient of the $\mathrm{Log}^2 s$ term in (eq (11) - I)

(1.2) MacDowell-Martin Bound

This bound on the[13] forward elastic slope parameter B_0

$$B_0 \geqslant \frac{1}{18\pi} \frac{\sigma_t^2}{\sigma_{el}} \qquad (5)$$

We test (5) against the data on p-p elastic scattering. At "SP" energies and above the ratio σ_{el}/σ_t for p-p is about 0.175, taking this value and the total cr.ss. from Fig (10) we find

$$B_{\text{minimum}} = \sigma_t^2/18\pi\sigma_{el} \simeq 10.1 \text{ to } 11.3 \quad (\text{Gev}/c)^{-2}$$

from the bottom to the top of the ISR energy range. While the experimental values of B(S,0) over the same energy range are 11.5 ± 0.6 to 12.6 ± 0.8 $(\text{Gev}/c)^{-2}$. The experimental results are only slightly (10 - 15%) greater than the lower bound.

Unfortunately the fact that the data are close to the bound gives no useful information about the impact parameter profile of the elastic amplitude, for example with either a black disc ($\sigma_{el}/\sigma_t \leqslant 1/2$) or a Goussian ($\sigma_{el}/\sigma_t \leqslant 1/4$), the slope parameter is given by the same formula

$$B_0 = \frac{1}{16\pi} \frac{\sigma_t^2}{\sigma_{el}} \qquad (6)$$

2. Physical Predictions

(2.1) Behaviour of σ_{el} , when σ_t grows.

(i) $\sigma_t \sim \text{Log}^2 s$, This implies $\sigma_{el} \sim \text{Log}^2 s$ the proof goes as follows:

Total cr.s. and elastic cr.s. are related through Schwarz inequality

$$\left| \sum_0^{L_{max}} (2l+1)\, \text{Im}\, f_l \right|^2 \leqslant L_{max}^2 \times \sum_0^{L_{max}} (2l+1) \left|\text{Im}\, f_l\right|^2 \leqslant L_{max}^2 \times \sum_0^{L_{max}} (2l+1) \left|f_l\right|^2 \qquad (7)$$

which gives

$$\left[\frac{s}{4\pi}\sigma_t\right]^2 \leqslant \frac{s}{4\pi} L_{max}^2\, \sigma_{el} \qquad (8)$$

Now using (1) we find

$$\sigma_{el} \geqslant \frac{4m_\pi^2}{\pi}\, \sigma_t^2 / \text{Log}^2 s \qquad (9)$$

The width of the diffraction peak ΔT may be defined by

$$\Delta T \simeq \left| \frac{F(s,0)}{s} \right|^2 / \sigma_{el} \qquad (10)$$

which implies that $\Delta T \sim 1/\mathrm{Log}^2 s$ (11)

if σ_t and σ_{el} behave like $\log^2 s$

(ii) $\sigma_t \sim \log s$

In this case the predictions concerning elastic cr.s. are somewhat changed, one can accept a constant elastic cr.s. with a width

$\Delta T \sim [\mathrm{Log}\ s]^{-2}$ or an elastic cr.s. behaving like Lags with a width $\Delta T \sim (\mathrm{Log}\ s^{-1}$

(2.2) Rising cr.s. and the real part of the scattering amplitude.

The ratio ρ between the real and the imaginary part of the scattering amplitude is related to the total cr.s. through a dispertion relation, in 1965 Khuri & Kimoshita proved that for a cr.s. which rises indefinitely as a power of $\mathrm{Log}\ E$ the ratio ρ goes to zero from above. For even signature amplitude F^+ (E) (which is the average between p-p and $\bar{p}$-p amplitudes), if σ_t behaves like Lag E, then F^+ (E) (which is dominantly imaginary) behaves like

$$F^+(E) \sim iE\,(\mathrm{Log}\,E)^{\beta} \qquad (12)$$

But it is easy to see that the expression (12) does not have the good crossing properties since $\mathrm{Log}\ (Ee^{i\pi}) = \mathrm{Log}\ E + i\pi$. The correct one is

$$F^+(E) \sim iE\left(\mathrm{Log}\,E - \frac{i\pi}{2}\right)^{\beta} \simeq iE(\mathrm{Log}\,E)^{\beta} + \frac{\pi\beta}{2}(\mathrm{Log}\,E)^{\beta-1} \qquad (13)$$

and then

$$\rho = \mathrm{Re}\,F^+ / \mathrm{Im}\,F^+ = +\frac{\pi\beta}{2}\,\frac{1}{\mathrm{Log}\,E} \qquad (14)$$

If we assume in addition that the odd signature amplitude is negligible at high energies since $\sigma_{\bar{p}p} - \sigma_{pp}$ seems to decrease fast, one sees that eq (14) apply to the proton-proton amplitude itself.

Various dispersion relation calculations of the forward real part have been done after ISR results. In which indefinitely rising cr.s. were introduced. In Fig (9)$^{(6)}$ the dashed line represents the results of such calculations in which it was assumed that asymptoticaly $\sigma_{\bar{p}p}=\sigma_{\bar{p}p}$ = 40 mb, while the continuous line represents the case of a cr.s. rising as (Log E)^2. It is clear from this figure that the recent experimental points agree better with the continuous line. Fig. (12)$^{(6)}$ shows the results obtained by Bantel & Diddens where it was assumed that above a certain value of the laboratory energy E, the total cr.s. becomes constant. These calculations indicated that measurement of the real part of p-p amplitude at the highest available energy (2000 Gev equivalent) is sensitive the behaviour of the total p-p cr.s. up to energies of order of 10,000 Gev.

3. p-p absorption at ISR and Black disc.

The energy dependence of the total, inelastic, and elastic cr.ss. are illustrated in Fig (13) (12). The inelastic cr.s. increases slowly and monotonically from about 6 Gev/c to 1500 Gev/c Laboratory momentum. The elastic cr.s. on the other hand shows a different behaviour, it is larger than the inelastic one at small energies, then decreases and then increases again. Such a behaviour can be considered quite natural, because at low energies the (real) potential scattering is large, while with increasing energy it is contribution goes to zero, so that only the (Imaginary) contribution of diffraction scattering, shadow of the inelastic processes, survives.

For the rest of this section we will use impact parameter language, where first we study briefly the black disc picture, and then we turn to the absorption at ISR.

(3.1) Black disc (6)

The elastic amplitude F(s,t) for small angle, and high energy elastic scattering may be written as:-

$$F(s,t) = \frac{2}{\pi} \int a\,da\; e^{i\vec{q}\cdot\vec{a}}\; f(s,a) \qquad (15)$$

where $q = \sqrt{-t}$ is the bi-momentum transfere, f(s,a) is the partial wave amplitude. From unitarity condition f(s,a) is given by

$$f(s,a) = \frac{i}{2}\left(1 - e^{2i(\delta_R + \delta_{Im})}\right) = \frac{i}{2}\left(1 - \eta\, e^{2i\delta_R(s,b)}\right) \qquad (16)$$

where $\eta = e^{-2\delta_{Im}}$ represents the fraction of the incident wave which is not absorbed. For no absorption $\eta = 1$, and for total absorption $\eta = 0$

Now by introducing the hypothesis that at very high energy elastic scattering is essentially diffractive ($\delta_R = 0$), eq (16) becomes

$$\mathrm{Im}\, f(s,a) = 1 - \eta/2 \qquad (17)$$

which gives

$$0 \leqslant \mathrm{Im}\, f(s,a) \leqslant 1/2 \qquad (18)$$

At the same time Im f(s,a) is constrained (from analyticity) to the range

$$\mathrm{Im}\, f(s,a) \leqslant e^{-(a - \beta a_0 \ln \frac{s}{\tilde{s}})/a_0} \qquad 6\ \beta \leqslant 1 \qquad (19)$$

Since σ_t is given by $\sigma_t = 8\pi \int a\,da\; \mathrm{Im}\, f(s,a)$ (20)

we see that the maximum value of σ_t is obtained when the partial waves amplitude Im f(s,a) follows the limits (18) and (19) as it is shown in the following figure.

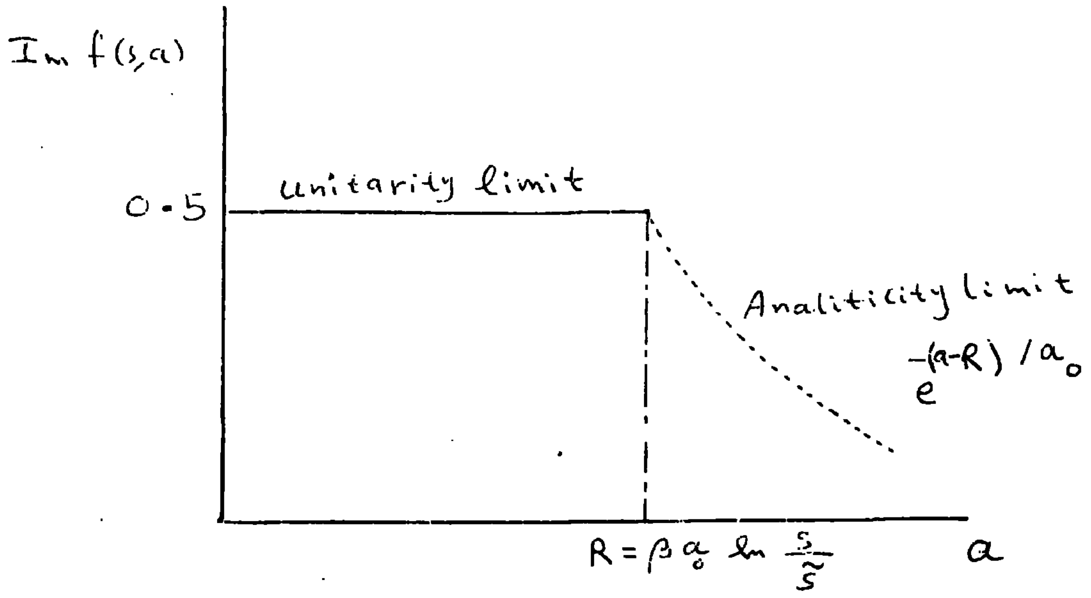

This is the black disc of Radius $R = \beta a_0 \ln \frac{s}{\tilde{s}}$ which increases at maximum as $\ln s$ so that the total cr.s. cannot increase faster than $\ln^2 s$.

On the "Diffractive" hypothesis (eq. (17) and from unitarity, σ_t, σ_{el} and σ_{inel} can be written in the forms.

$$\sigma_t = 4\pi \int_0^\infty a\, da\, (1-\eta) \quad (21)$$

$$\sigma_{el} = 2\pi \int_0^\infty a\, da\, (1-\eta)^2 \quad (22)$$

$$\sigma_{in} = 2\pi \int_0^\infty a\, da\, (1-\eta^2) \quad (23)$$

we saw that the Froissart bound is diffractively saturated when the partial waves up to a radius R are fully absorbed (i.e. when $\eta \ll 1$), in this limit we have $\sigma_{el} \simeq \sigma_{in} \simeq \sigma_t/2 \simeq \pi R^2$

This is certainly not the case in the ISR where we have seen (I-3-h) that $\sigma_{el}/\sigma_t \simeq 0.17$ in ISR energy range.

(3.2) proton-proton absorption at ISR.

In Fig. (14)$^{(12)}$ Amaldi has drawn the elastic differential cr.ss. at the two extreme ISR energies, making use of all the available information. By introducing the usual simplifying hypothesis that the real part of the amplitude is zero at all momentum transfere (with the exception of the diffraction minimum), and f(s,a) is also pure imaginary (eq (15) becomes

$$\mathrm{Im}\, F(s,t) = \frac{2}{\pi} \int a\, da\; e^{i \vec{q} \cdot \vec{a}}\; \mathrm{Im}\, f(s,a) \qquad (24)$$

From Fig (14) and by inverting eq (24) one can work out the partial wave amplitude Im f(s,a) as a function of the p-p impact parameter at the minimum and maximum ISR energies. The results of these calculations are illustrated in Fig. (15)(12), it is evident from this figure that at ISR the amplitude is quite far from its maximum limit (Im f(s,a) $\leqslant \frac{1}{2}$). Since the saturation of the Froissart bound is obtained when, for a certain range of impact parameter this maximum limit is reached, we conclude that the increasing cr.s. at ISR has nothing to do with the saturation of the Froissart bound.

The "opaqueness" $\Omega(a) = 2\,\delta_I$ is related to the Im f(s,a) through the relation $\mathrm{Im}\, f(s,a) = \left(1 - e^{-\Omega(a)}\right)/2$ (25)

The opaqueness profiles obtained from the curves of Fig (15) are plotted in Fig. (16)(12). The central absorption $(1 - e^{-\Omega(0)})$ is about 75% in the ISR energy range, and $\Omega(a)$ is too small to give a flat behaviour of the partial wave amplitude Im f(s,a,), as would be necessary in order to observe the Froissart regime.

Since the Froissart bound is not saturated in the ISR energy range, it comes no surprise that the slope of the forward elastic peaks Bo increases approximately as lns, while it must have a symptotic growth $B_0 \sim \ln^2 s$.

Fig (16) contains another important information. By comparing the shape of $\Omega(a)$ and $\Delta\Omega(a)$, we find that, in the ISR energy range the opaqueness increment has an average radius of about 1 fm, and it is more peripheral than the opaqueness itself. This is quite natural, since Fig (14) shows that the increase in the elastic cr.s. comes mainly from the small momentum transfere which corresponds to large impact parameter.

In Conclusion: The dynamics of the inelastic processes must be able not only to explain the increase of σ_{inel} but must also produce an increase of opaqueness which is mainly peripheral.

CHAPTER THREE

The pomeron in proton-proton scattering

Introduction

The asymptotic cr.s. is supposed to be dominated by an even signature pole, with vacuum quantum numbers, and intercept $\alpha(0) = 1$ (because the Froissart bound restricts all J-plane singularities to $\alpha(0) \leqslant 1$) which is called the pomeron. Since no particles have been identified with the pomeron, and since in most processes it occurs together with several normal Reggeons, it has been hard to determine the nature of this singularity. Fortunately we have now good opportunity to learn about the pomeron from p-p system both because (i) ISR provides super high energy uniquely for this system (ii) The contribution of the secondary Regge exchanges "R" to the imaginary part of the amplitude is small (This is because pp scattering has no resonances i.e. with exotic (di-baryon) quantum numbers, then according to the two component theory of duality, one finds $\sum_{i} \mathrm{Im}\, R_{i} \simeq 0$.

This chapter is concerned with fitting pp scattering data for $10 \leqslant S \leqslant 3000 \ \mathrm{Gev}^2$ with Regge pole and cut models. In the first section a parameterrization of the data at low and serpukhov energies are given. A variety of Regge pole and cut models are reviewed in sections 2 & 3, only two types of models are able to explain the data over the whole energy range satisfactorily. The first one has pomeronpole with trajectory $\alpha_{P}(t) = 1.06 + 0.25\, t$, and a non-shrinking "core" term. The second has a flat pomeron trajectory $\alpha_{P}(t) = 1.06$ for all t, and strong eiknal-models cuts, which explain both the shrinkage at low $|t|$ and the lake of it at large $|t|$.

Finally a various speculations which relate the fact that $\alpha_{\mathbb{P}}(0) > 1$ to the small triple-pomenon coupling and other remarks are discussed briefly in section 4 .

1. The data, α_{eff}

It is well known that up to $S = 60\ \mathrm{Gev}^2$ the total cr.ss. can be parameterized by

$$\sigma_t(s) = \sigma(\infty) + A\, S^{-1/2} \qquad (1)$$

$\sigma(\infty)$ represents the pomeron pole, the second term represents the contributions of secondary trajectories, where we have used the approximation that the intercepts of the secondary trajectories are given by

$$\alpha_{P'} = \alpha_{A_2} = \alpha_{\omega} = \alpha_{\rho} \simeq 1/2 \qquad (2)$$

In the process pp ⟶ pp the trajectories are $\mathbb{P} + P' - \rho - \omega + A_2$ since the difference between pp and pm cr.ss. are very small, we neglect I = 1 exchange (A_2 , ρ). On the other hand the fall in σ_t (p-p) at low energies means that the p and w cannot be exactly exchange degenerate.

The data from total cr.ss. experiments at serpukhov energies (50 $\leqslant S \leqslant 120\ \mathrm{Gev}^2$) indicate that modification in this Regge pole picture eq (1) of linearity in $S^{-1/2}$ are necessary, and the vacuum Regge cut was introduced.

$$\sigma_t(s) = \sigma(\infty) + A\, s^{-1/2} - \frac{\beta}{C + \mathrm{Log}\, S} \qquad (3)$$

The final term represents a destructive $\mathbb{P} \otimes \mathbb{P}$ cut, which approximately cancels the fall of the $s^{-1/2}$ term in serpukhov region, and gives the levelling-off of the total cr.ss. observed in that region. But the rapid rise in σ_t (pp) at ISR is too great to be accommodated by eq. (3), clearly one needs a strong cuts which then have difficulty at small s. An alternative explanation, which we will explore in Sec. 2 & 3 is that $\alpha_{P}(o) > 1$, of course if continued indefinitely such a behaviour would violate the Froissart bound, but eikonalization could prevent this.(14)

Fig. (17)(10) shows $\frac{d\sigma}{dt}$ (pp) from ISR together with some lower energy points. From these data we can calculate the effective trajectory, α_{eff}, defined as usualy by

$$\mathrm{Log}\frac{d\sigma}{dt} = (2\alpha_{eff} - 2)\,\mathrm{Log}\,S + F(t) \qquad (4)$$

The effective trajectory for pp scattering obtained from ISR data is shown in Fig. (18) it is essentially a straight line

$$\alpha_{eff} = 1.06 + 0.25\ t \qquad (5)$$

for $|t| < 1.2\ \mathrm{Gev}^2$, followed by a jump to α_{eff} (t) $\simeq 1.0$ for $|t| > 1.8\ \mathrm{Gev}^2$ reflecting the energy independent of the large $|t|$ data. The effective trajectory for pp scattering for $S < 50\ \mathrm{Gev}^2$ shows a different behaviour. Fig (19), it has the form $\alpha_{eff} \simeq 1.06 + 0.4\ t$ (6) for all $|t|$ except in the shoulder region.

From Figs (18,19) we conclude that we are observing mainly the pomeron pole out to $|t| \simeq 1.2\ \mathrm{Gev}^2$, and possibly at larger $|t|$ at low S but that something quite different controls the large $|t|$, high S, behaviour.

In the following models, the helicity flip is neglected, and so for each process there is just a single scattering amplitude, A(s,t) normalized such that

$$\frac{d\sigma}{dt} = \frac{0.3893}{16\pi s^2}\,|A(s,t)|^2 \qquad (7)$$

$$\sigma_t(s) = \frac{1}{s}\,\mathrm{Im}\,A(s,0) \qquad (8)$$

2. A Regge pole model

Fit (i)

The effective Regge trajectory at ISR energies constructed in Sec. (i) strongly suggests that the small angle diffraction scattering may be associated with the exchange of a Regge pole with intercept $>$ 1. To incorporate the slope break at $|t| \simeq 0.15\,\mathrm{GeV}^2$ there must be two exponentials in the pomeron residue. So we put

$$A^{\mathbb{P}}(s,t) = -G_{\mathbb{P}}\left(e^{-\frac{1}{2}i\pi}s\right)^{\alpha_{\mathbb{P}}(0)} e^{C_{\mathbb{P}}t}\left[(1-x)+x\,e^{a_1 t}\right] \qquad (9)$$

where
$$C_{\mathbb{P}} = a_{\mathbb{P}} + \alpha'_{\mathbb{P}}\left(\log s - \tfrac{1}{2}i\pi\right) \qquad (9')$$

To account for the low energy data, we must add the non-diffractive contributions associated with the P' and w trajectories. These we write as

$$A^{R} = -G_{R}\left(e^{-\frac{1}{2}i\pi}s\right)^{\alpha_R(0)} e^{C_R t}\left[\alpha_R(t) \pm i\beta e^{a_3 t}\left(1+\frac{t}{t_0}\right)\right] \qquad (10)$$

Here $\pm$ refers to pp, $\bar{p}p$ respectively, and the cross over of the pp and $\bar{p}p$ differential cr.ss. has been built into the w contribution, and the trajectories are assumed degenerate.

To account for the diffraction minimum, and the essentially non-shrinking, energy independent $\frac{d\sigma}{dt}$ for $|t| > 2.0\,\mathrm{GeV}^2$ at ISR, we will add an additional term with a destructive phase relative to the pomeron pole, which we shall refer to as the "core"

$$A^{C}(s,t) = G_c\left(e^{-\frac{1}{2}i\pi}s\right)^{\alpha_c(0)} e^{C_c t} \qquad (11)$$

where
$$C_c \equiv a_c + \alpha'_c\left(\log s - \tfrac{1}{2}i\pi\right) \qquad (11')$$

$\alpha'_c = 0$, because of the lack of shrinkage.

The sum of eqs. (9, 10, 11) gives the excellent fit (i) shown in Figs. (20), table (1). It is clear from this fit that with eqs. (9, 10, 11) we can readily explain all the data except for $\frac{d\sigma}{dt}$ (pp) for low S, large $|t|$. The core term which fits this large $|t|$ region at high S is too small at low s, more important is the fact that $\frac{d\sigma}{dt}$ shrinks at low s, but not at high S. One may think that since α_{eff} at large $|t|$ in Fig (19) seems to be a continuation of the pomeron we can replace eq. (9) by

$$A^{\mathbb{P}}(s,t) = -G\left(e^{-\frac{1}{2}i\pi}s\right)^{\alpha_{\mathbb{P}}^{(0)}} e^{c_{\mathbb{P}}t}\left[(1-x-y)+x e^{a_1 t}+y e^{a_2 t}\right] \qquad (12)$$

where the final term is responsible for large $|t|$, and has a negative sign to produce a dip at $|t| \simeq 1.4\ \mathrm{Gev}^2$. But it is impossible to get the correct energy dependence of the large $|t|$ data with eq. (12), because the pomeron slope at small $|t|$ is $\alpha'_{\mathbb{P}} \simeq 0.25$, whereas Fig (19) shows that $\alpha'_{\mathbb{P}} \simeq 0.4$ for large $|t|$. Instead we tried$^{(10)}$ adding to eq. (9) an effective pomeron term

$$A^{\mathbb{P}_1}(s,t) = y\left(e^{-\frac{1}{2}i\pi}s\right)^{\alpha_{\mathbb{P}_1}^{(0)}} e^{c_{\mathbb{P}_1}t} \qquad (13)$$

with trajectory $\alpha_{\mathbb{P}_1}(t) = 1.0 + 0.47t$, to represent the effective pomeron trajectory at large $|t|$, and low S.

Fit. (ii)

The total amplitude now is given by

$$f(PP) = A^{\mathbb{P}} + A^{R} + A^{C} + A^{\mathbb{P}_1}$$

and the sum of eqs. (9, 10, 11, 13) gives the excellent description of the data shown in Fig. (21) Table (1).

An important remark concerning the effective pomeron term is that, though eq. (13) is negligible for $|t| \ll 1.4\ \mathrm{Gev}^2$, and eq. (9) is unimportant for $|t| \gg 1.4\ \mathrm{Gev}^2$ but in the shoulder region at low energy both terms contribute significantly to $\frac{d\sigma}{dt}$, and the slope of the curve depends crucially on their phase difference $\alpha_{\mathbb{P}}(1.4) \simeq (0.7$, $\alpha_{\mathbb{P}_1}(1.4) \simeq 0.5)$. Thus eq. (13) cannot be regarded as simply the continuation to larger $|t|$ of eq. (9), with a bend in the pomeron pole trajectory. If it were there would be a zero in the pomeron contribution at $|t| \simeq 1.4$ Gev^2, and hence a dip in $\frac{d\sigma}{dt}$. However if eq. (13) is regarded as just an "effective trajectory" which has substantial contributions from cuts, this phase difference is quite acceptable.(10)

Fit. (iii)

It is also possible to use the R term to explain the large t, low s data, if one takes the view that if the p' and/or w effective trajectory is rather flat, which may be the case either because their trajectories are flatter than those of ρ and A_2 or because for some reason, Regge cut effects are more important for p' and/or w more than for ρ and A_2 exchange.

The total amplitude this time is given by

$$f\,(PP) = A^{\mathbb{P}} + A^{C} + A^{R}$$

where

$$A^R = -G_R\left(e^{-\frac{1}{2}i\pi}\, s\right)^{\alpha_R(0)} e^{C_R t}\left[\alpha_R(t) \pm i\beta\, e^{a_3 t}\left(1+\frac{t}{t_0}\right) + \beta_1 e^{a_4 t}\right] \qquad (14)$$

The additional term here is out of phase with the $\mathbb{P}$ at $|t| \simeq 1.4$ Gev^2 and gives the required 'shoulder', as it is shown in Fig. (22).

The differences between fits. (ii) and (iii) are not important, as far as the pomeron is concerned, because in both cases we have at ISR energies the pomeron term eq. (9), supplemented by the "core" eq. (11)

The above fits leave us with two problems (i) is it necessary to have $\alpha_{\mathbb{P}}(0) > 1$? and if so how is this compatible with unitarity? What is the origin of the "core"?. It might be expected that Regge cuts are relevant to both problems which we examine next.

3. Regge Cut Models

According to the eikonal model the full impact parameter amplitude is:-

$$\chi\,(s,b) = \frac{i}{\lambda}\left[1 - e^{i\lambda\,\chi^{\mathbb{P}}(s,b)}\right] \qquad (15)$$

where λ = 1 in the conventional eikonal model, but we have included the possibility of an enhancement factor, as in the absorption model.

One of the advantages of eikonalization is that, by imposing s-channel unitarity on the input via eq. (15), one ensures that the amplitude satisfies the Froissart bound even if the input pole does not. Thus if we write the pomeron pole as

$$A^{\mathbb{P}}(s,t) = -G_{\mathbb{P}}\left(e^{-\frac{1}{2}i\pi}s\right)^{\alpha_{\mathbb{P}}(0)} e^{c_{\mathbb{P}}t} \tag{16}$$

The eikonal function is

$$\chi^{\mathbb{P}}(s,b) = \frac{1}{8\pi s}\int_{-\infty}^{0} A^{\mathbb{P}}(s,t)\,J_0(b\sqrt{-t})\,dt \tag{17}$$

$$= \frac{iG_{\mathbb{P}}}{8\pi c_{\mathbb{P}}}\left(e^{-\frac{1}{2}i\pi}s\right)^{\alpha_{\mathbb{P}}(0)-1} e^{-b^2/4c_{\mathbb{P}}} \tag{18}$$

hence if $b^2 < b_0^2 \equiv 4\alpha'(\alpha_{\mathbb{P}}(0)-1)\,\mathrm{Log}^2 s$ then $\chi^{\mathbb{P}}(s,b) \xrightarrow[s\to\infty]{} i\infty$, but if

$b^2 > b_0^2$, $\chi^{\mathbb{P}}(s,b) \xrightarrow[s\to\infty]{} 0$ so from eq. (15) we find

$$\chi(s,b) \to \frac{i}{\lambda} \quad \text{for} \quad b^2 < b_0^2 \tag{19}$$

$$\chi(s,b) \to 0 \quad \text{for} \quad b^2 > b_0^2 \tag{20}$$

With the usual eikonal formula, the scattering amplitude A(s,t) is given by

$$A(s,t) = \frac{4\pi s}{\lambda}\int_0^{\infty} i\left[1 - e^{i\lambda\chi^{\mathbb{P}}(s,b)}\right] J_0(b\sqrt{-t})\,b\,db \tag{21}$$

$$= \sum_{n=1}^{\infty} -\frac{G_{\mathbb{P}}\left(e^{-\frac{1}{2}i\pi}s\right)^{\alpha_{\mathbb{P}}(0)}}{n.n!} \times \left[\frac{-\lambda G_{\mathbb{P}}\left(e^{-\frac{1}{2}i\pi}s\right)^{\alpha_{\mathbb{P}}(0)-1}}{8\pi c_{\mathbb{P}}}\right]^{n-1} e^{c_{\mathbb{P}}t/n} \tag{21'}$$

which gives (eq. 21)

$$\sigma_t = \frac{1}{s}\,\mathrm{Im}\,A_{el}(s,0) \longrightarrow \frac{8\pi\alpha'}{\lambda}\left(\alpha_{\mathbb{P}}(0)-1\right)\mathrm{Log}^2 s \tag{22}$$

Thus saturating the Froissart bound, however this behaviour sets in only for Log S $\gg \frac{a_{\mathbb{P}}}{\alpha'_{\mathbb{P}}} \simeq 20$

In the following models we shall only consider multi-pomeron cuts, where the intercept of the pomeron $\alpha_{\mathbb{P}}(0)$ and the enhancement factor "λ" will be taken as parameters.

3.1 $\alpha_{\mathbb{P}}(0) = 1$ and strong cuts.

From eq. (21') with $\alpha_{\mathbb{P}}(0) = 1$ we find

$$\sigma_t = \frac{1}{s}\, \mathrm{Im}\, A(s,0) \longrightarrow G\left[1 - \frac{\lambda G}{32\pi\alpha' \mathrm{Log}\, s} + \cdots\right] \tag{23}$$

hence, as long as the input Regge trajectory has a slope, as demanded by shrinkage of the forward $d\sigma/dt$, the predicted σ_t will rise with energy because the destructive $\mathbb{P} \otimes \mathbb{P}$ cut contribution decreases like $(\alpha' \mathrm{Log}\, s)^{-1}$. To obtain the actual amount of rise (4.5 mb) at ISR we need roughly $G_p = 85$ mb, $\lambda = 1.5$, but then it is hard to fit the data at lower energies, even with a substantial R term. More important, the very strong cuts results in a dip at $|t| \simeq 0.5$ instead of 1.4 Gev^2, even with more complicated structure for the pole residue it is impossible to get the dip out to $|t| \simeq 1.4$ Gev^2, if the cuts are strong enough to reproduce the σ_t rise.

3.2 $\alpha_{\mathbb{P}}(0) > 1$ and weak cuts.

Once we allow $\alpha_{\mathbb{P}}(0) > 1$ the rise in the total cr.s. can be blamed mainly on the pole, and so the cuts can be weaker. We may thus hope to adjust their strength so as to ensure that the dip in $d\sigma/dt$ occurs in the correct place.

The contribution of a $\mathbb{P} \otimes \mathbb{P}$ cut may be written$^{(15)}$

$$A^{\mathbb{P}\mathbb{P}}(s,t) = \frac{i}{16\pi s^2} \iint dt_1\, dt_2\, A^{\mathbb{P}}(s,t_1)\, A^{\mathbb{P}}(s,t_2)\, N^2_{\mathbb{P}\mathbb{P}}(t,t_1,t_2)\, \frac{\sigma(K)}{K^{1/2}} \tag{24}$$

where the Gribov vertex $N_{\mathbb{P}\mathbb{P}}(t,t_1,t_2) = \sqrt{\lambda}$ in the enhanced absorption model

Thus with $A^{\mathbb{P}}$ given by eq. (9) we find

$$A^{\mathbb{P}\mathbb{P}}(s,t) = \frac{\lambda G_{\mathbb{P}}^2}{16\pi}\left(e^{-\frac{1}{2}i\pi} s\right)^{2\alpha_{\mathbb{P}}(0)-1} \Bigg[(1-x^2)\,\frac{e^{c_{\mathbb{P}}t/2}}{2c_{\mathbb{P}}} + \tag{25}$$

$$+ 2x(x-1)\,\frac{\exp[c_{\mathbb{P}}(c_{\mathbb{P}}+a_1)t/(2c_{\mathbb{P}}+a_1)]}{2c_{\mathbb{P}}+a_1} + x^2\,\frac{\exp[(c_{\mathbb{P}}+a_1)t/2]}{2(c_{\mathbb{P}}+a_1)}\Bigg].$$

By adjusting λ we can make eq. (25), eq. (9) interfer destructively at $|t| \simeq 1.4$ Gev^2 and get a dip. But then, since the logarithmic slope of the cut is roughly half that of the pole the flatness of the pp data for $|t| > 1.4$ Gev^2 cannot be reproduced.

This defect may be remedied by inserting a t dependence into $N_{\mathbb{P}p}$. Limiting ourselves to exponentials, we can put

$$N^2_{\mathbb{P}p} = \lambda\, e^{b_1 t + b_2 (t_1 + t_2)} \tag{26}$$

giving

$$A^{\mathbb{P}\mathbb{P}}(s,t) = \frac{\lambda G^2_{\mathbb{P}}}{16\pi} \left(e^{-1/2 i\pi} s\right)^{2\alpha_{\mathbb{P}}(0)-1} e^{b_1 t} \left[(1-x)^2 \frac{\exp\left[(c_{\mathbb{P}}+b_2)/2\right]}{2(c_{\mathbb{P}}+b_2)} + \right.$$
$$\left. + 2x(1-x) \frac{\exp\left[(c_{\mathbb{P}}+b_2)(c_{\mathbb{P}}+b_2+a_1)t/(2c_{\mathbb{P}}+2b+a_1)\right]}{2c_{\mathbb{P}}+2b_2+a_1} + x^2 \frac{\exp\left[(c_{\mathbb{P}}+b_2+a_1)t/2\right]}{2(c_{\mathbb{P}}+b_2+a_1)} \right] \tag{27}$$

Thus both b_1 and b_2 may be used to bring the t dependence of the cut into line with the data. The contribution of higher order $\mathbb{P} \otimes \mathbb{P} \otimes \mathbb{P}$ cut in this model make no difference for $|t| < 5$ Gev^2 becuase λ is very small ($\lambda \simeq$ 0.07).

The sum of eqs. (27) (9) (10) gives the excellent description of the data shown in table (2) and Figs (23),$^{(15)}$, with either b_1 or b_2 non-zero, and the position of the $\mathbb{P} \otimes \mathbb{P}$ branch point at $\alpha_2(t)$ = 1.14 + 0.11t is in quite good accord with the energy dependence at large $|t|$, "Fig (23-b)".

An important remark concerning unitarity in this model is that, from eq. (19) we find that the Imaginary part of the impact parameter amplitude

$$\mathrm{Im}\, \chi(s,b) \longrightarrow 1/\lambda \text{ as } s \longrightarrow \infty \text{ for } b^2 < b_0^2$$

So the central partial waves violate the unitarity bound, $\mathrm{Im}\, \chi > 1$ for $\lambda < 1$. But with our parameters this occurs only for $s > 10^8$ Gev^2

So there need be no modification of the behaviour $\sigma_t(s) \sim s^{\alpha_{P}(0)-1}$ for the anticipated future. However the weak cuts used in this model are insufficient to ensure the satisfaction of unitarity asymptotically, and one must expect additional corrections when much higher energies are achieved.

3.3 $\alpha_{P}(0) > 1$, $\alpha'_{P} = 0$, and strong cuts.

In this model the pomeron is non-shrinking, and the structure of $d\sigma/dt$ comes from a complicated overlap of terms. The various $|t|$ regions of Fig. (17) cannot be identified, even approximately with single scattering, double scattering etc. even the small $|t|$ regions depend in an essential way on the superposition of various terms in the series.

If the pomeron residue is parameterized by a single exponential, it is impossible to fit the data, because the dip is too close in at $|t| \simeq 0.6\ \mathrm{GeV}^2$, but if the pomeron residue is given a two exponential, a very good fit of σ_t and $d\sigma/dt$ up to the second maximum can be obtained, however for $|t| > 2$ the fit falls much below the data, with 3 exponential in the residue

$$A^{P}(s,t) = -G_{P}\left(e^{-\frac{1}{2}i\pi} s\right)^{\alpha_{P}(0)} e^{c_{P}t}\left[(1-x-y) + x e^{a_1 t} + y e^{a_2 t}\right] \tag{28}$$

Used in eq. (17) together with the Reggeon term eq. (14), a good fit of all ISR data can be obtained (Fit (iv), table (1), Fig. (24)). It is only deficiencies are that the dip at $|t| \simeq 1.4$ is perhaps not quite sharp enough, and it falls below the data for $|t| > 3\ \mathrm{GeV}^2$.

The shrinkage mechanism in this model is quite different from other models. It stems entirely from interference between the various terms in the series, since the n-particle exchange term $\sim s^{1+\Delta n}$. The model also has no difficulty in reproducing the lack of shrinkage of the $|t| > 1.8$ Gev^2 ISR $d\sigma/dt$, and the dip depends on the cooperation of many terms, as it is shown in the figure below

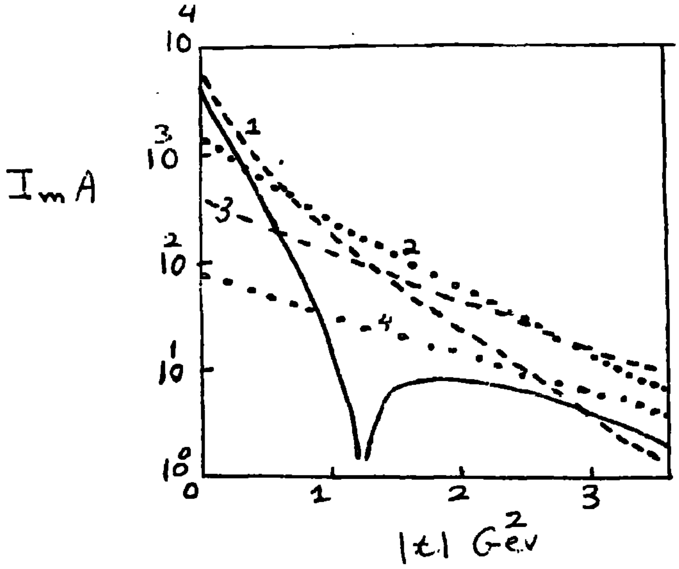

The contribution of the first of our terms in the multiple scattering series of fit. (iv). The first & third terms are positive, while the second & fourth are negative. The solid line is the sum of the series.

Though this model is certainly quite compatible with the data, but as several parameters were needed for the input pomeron residue it was unclear whether one was really doing more than finding an eikonal decomposition of the data. Also we know that this sort of fixed pole ($\alpha'_{\mathbb{P}} = 0$) is hard to reconcile with t channel unitarity. It seems more reasonable that the small $|t|$ shrinkage should be due to the slope of the input pole.

4. Conclusions and Remarks

4.1 Summary of these Fits.

(a) From the above fits and the variations on them we conclude that $\alpha_{P}^{(o)} > 1$, i.e. the rise of $_{t}$ at ISR cannot be due to cuts alone.

(b) The $|t| < 1.4$ Gev^2 data are consistent with a pomeron pole $\alpha_{P}(o) = 1.06 + 0.25\ t$ without multiple scattering correction but a "core" term for large $|t|$.

(c) In the model of sub section (3.2) we saw that the destractive core term needed to explain the large $|t|$ data, and the diffraction minimum, can in fact be constructed as a $P \otimes P$ cut provided one is willing to allow the cuts to be very weak ($\lambda \simeq 0.07$, more than a factor of 10 smaller than the eikonal/absorption prescription), and provided also that one allows arbitrary structure in the pomeron - particle couplings (i.e. the Gribove vertices). Ref (15) applied this model also to πP, KP and predicted that a similar minima should be observed in meson-baryon scattering at FNAL somewhere in the region $1.5 < |t| < 2.5$ Gev^2.

4.2 Carrigan break

Close inspection of ISR data by means of an effective Regge trajectory has shown that the division of the forward elastic scattering into t regions separated by the "Carrigan break" is wholly artifical,$^{(17)}$ as the energy dependence of $d\sigma/dt$ shows a smooth behaviour across this so-called break. This structure has been interpreted as a threshold effect,$^{(14)}$ or due to pomeron renormalization, but not due to pole / cut interference, since its position seems to be energy independent.

4.3 $\alpha_{P}^{(c)} > 1$ and the peripheral nature of $\Delta \mathrm{Im}\, \chi$.

The behaviour of the pomeron makes it easy to understand why the part of the ISR cr.s. increases with s is peripheral. $(d\sigma/dt)_{t=0}$ is increasing because $\alpha_{P}(0) > 1$, but because of the shrinkage, $d\sigma/dt$ constant, where $\alpha_{P}(t) = 1$, i.e. for $|t| \simeq 0.25$, and is decreasing for large $|t|$. Hence the change $\Delta \frac{d\sigma}{dt}$, has a zero at $|t| \simeq 0.25$, which means that the difference between the impact parameter amplitudes $\Delta \chi$ (s,b) is somewhat peaked at $b \simeq 0.8$ fm, as it is shown in Fig. (25)$^{(10)}$. Thus the peripheral nature of $\Delta \mathrm{Im}\, \chi$ is a perfect Regge pole effect with $\alpha_{P}(0) > 1$.

4.4 The smallness of $\alpha_{P}(0)-1$ and the smallness of the triple-pomeron coupling.

Out conclusion that $\alpha_{P}(0) \simeq 1.06$ seems to accord well with various recent speculations about how the various partial cr.ss. build up the total cr.s., and hence the structure of the pomeron.$^{(18, 19)}$.

Re (19) proposed a perturbative view of the pomeron. In the zeroth order perturbative approximation the pomeron is generated by the sum of purely inelastic (non-diffractive) channels. Diffractive events of large masses represent the first order, and give the order of magnitude of the expansion parameter $g \ln \frac{s}{\bar{s}}$ (g is the triple pomeron coupling). Double and higher diffractive events will become detectable at even higher energies and will contribute with higher powers of $\ln$ s. After summation of the peturbation series, our pomeron pole has intercept (1+g). The amount of the re-normalization being proportioned to the triple pomeron coupling since

$$\sigma_t(s) = G\, s^{\Delta} = G\, e^{\Delta \ln s} = G + G\, \Delta \ln s + \dots \qquad (29)$$

Thus the smallness of the amount by which $\alpha_{P}(0)$ lies above 1 is due to the smallness of the triple pomeron coupling. Of course, the renormalized pole at $\alpha_{P}(0) = 1+ \Delta$ cannot be the leading J-plane singularity of the full scattering amplitude, which must have $\alpha_{P}^{max}(0) \leqslant 1$.

But absorptive corrections can produce a set of cancelling Regge cuts,(21,21) and the leading trajectories then turn out to be of the Schwartz type

$$\alpha(t) = 1 + R_0\sqrt{t}\,, \qquad R_0^2 \equiv 4\alpha'_{P}\,\Delta \tag{30}$$

However, these corrections will not be evident until Log s $\gg \frac{b}{\alpha'}$ which we are very far from reaching.

CHAPTER FOUR

Overlap Function Model

This chapter is devoted to studying, within the framework of the shadow scattering approach, the implication of increasing p-p total cr.s. and diffractive structure of p-p elastic scattering (I) on the inelastic overlap function and its form in t and b-space. The material is organized as follows.

1. S-channel unitarity relation
2. inelastic overlap function in momentum space
3. inelastic overlap function in impact parameter space.
    - 3.1 G (s,b) (HENZI et al Re. 28)
    - 3.2 G (s,b) (H.I. Miettinen Re. 24 & 33)
4. Impact structure of inelastic diffraction.
    - 4.1 G (s,b) (N. Sakai & J.N.J. White Re. 22,23)
    - 4.2 Two component analysis of the inelastic overlap function "Unabsorbed overlap function"
5. Summary & Conclusions.

1. S-channel unitarity relation

It is widely believed that diffraction is the shadow of absorption due to the existence, at high energies, of many open inelastic channels. Unitarity in the s-channel gives

$$\mathrm{Im}\langle f|T_{el}|i\rangle = \sum_{el}\langle f|T^{\dagger}_{el}|i'\rangle\langle i'|T_{el}|i\rangle + \sum_{inel}\langle f|T^{\dagger}|n\rangle\langle n|T|i\rangle \qquad (1)$$

i' = elastic states

n = inelastic states

or

$$\tau_{tot}(s,t) = \tau_{el}(s,t) + \tau_{in}(s,t) \qquad (2)$$

which defines the overlap function τ . In the forward direction eq. (2) is the well known optical theorem, the overlap functions are thus normalized

$$\tau_{tot}(s,0) = \sigma_{tot} , \quad \tau_{el}(s,0) = \sigma_{el} , \quad \tau_{in}(s,0) = \sigma_{in} \tag{3}$$

According to eq. (1) the imaginary part of the elastic amplitude is built up by two parts : the second term on the right hand side gives the shadow of the inelastic channels open, the first term is that of the elastic scattering itself. Thus eq (1) is a non-linear integral equation for the elastic amplitude. By making use of angular momentum conservation, we write it in impact parameter space.$^{(24)}$

$$\mathrm{Im}\, h_{el}(s,b) = \frac{1}{4}\left| h_{el}(s,b)\right|^2 + G_{in}(s,b) \tag{4}$$

Here b is the impact parameter of the collision, and $h_{el}(s,b) \equiv T_{fi}(s,b)$. If the phase of the elastic amplitude is known, we can solve eq. (4) for Im h_{el} in terms of G (s,b). Assuming for example, that Re h_{el} (s,b) = 0, we find.

$$\mathrm{Im}\, h_{el}(s,b) = 2\left(1 - \sqrt{1 - G_{in}(s,b)}\right) \tag{5}$$

negative sign in front of the square root in order to agree with the assumption (above) that elastic scattering is "caused" by the presence of the inelastic processes. With this normalization the unitarity bounds are

$$0 \leqslant G_{in}(s,b) \leqslant 1 , \qquad 0 \leqslant \mathrm{Im}\, h_{el}(s,b) \leqslant 2$$

The eq. (5) connects the inelastic and total overlap functions at the same impact parameter. This follows from angular momentum conservation, and makes the impact parameter representation very convenient for the study of unitarity effects.

The functional dependence of the total and elastic overlap function (eq. (5)) on the inelastic overlap function is shown in Fig. (26). When the amount of absorption is small the imaginary part of the elastic amplitude is built up mainly by the inelastic channels. However when the absorption approaches its maximum value, the elastic overlap function increases very rapidly and provides an important contribution to the elastic amplitude. Finally, when the amount of absorption approaches the upper unitarity limit, the elastic and inelastic overlap functions become equal.

The three terms of eq. (4) have a simple physical interpretation. They tell us how the total, elastic and inelastic cr.ss. are distributed as a function of the impact parameter.

$$\left.\begin{aligned} d\sigma_{tot}/d^2b &= 2\left(1-\sqrt{1-G_{in}}\right) \\ d\sigma_{el}/d^2b &= \left(1-\sqrt{1-G_{in}}\right)^2 \\ d\sigma_{in}/d^2b &= G_{in} \end{aligned}\right\} \qquad (6)$$

$$\sigma_i = \int_0^\infty d^2b \, \frac{d\sigma_i}{d^2b} \qquad (7)$$

, and s channel unitarity now reads

$$d\sigma_{tot}/d^2b = d\sigma_{el}/d^2b + d\sigma_{in}/d^2b \qquad (8)$$

"Here b is the two-dimensional impact parameter vector"

The study of solution (eq.(5)) with eq. (7) make it easy to understand the experimental observed ratios of $\frac{\sigma_{el}}{\sigma_{tot}}$, $\frac{B_0}{\sigma_{tot}}$ (Bo is the elastic slope parameter for $|t| \leqslant 0.15$). For example, for the "Black disc" model

$$G_{in}(s,b) = \begin{cases} 1 & 0 \leqslant b \leqslant R \\ 0 & b > R \end{cases} \qquad (9)$$

we find

$$\sigma_{el} / \sigma_{tot} = \tfrac{1}{2} \qquad (10)$$

On the other hand, if G (s,b) is approximately Gaussian (as we shall see later)

we find

$$0 \leqslant \sigma_{el} / \sigma_{tot} \lesssim 0.185 \qquad (11)$$

where this inequality corresponds to

$$0 \leqslant G\ (s,b) \text{ at } b = 0 \leqslant 1 \qquad (12)$$

If G (s,b) is assumed Gaussian exactly with maximum strength allowed by unitarity the following Van Hove limits are obtained (see Fig. (27)).

$$\sigma_{el} / \sigma_{tot} = 0.185 \quad (\text{experiment} \simeq 0.175)$$

$$(13)$$

$$b_{c} / \sigma_{tot} = 0.296 \quad (\text{experiment} \simeq 0.296)$$

So we conclude that the small ratio of elastic to inelastic scattering follows from the strong suppression of the elastic shadow when the absorption deviates from the upper unitarity limit.

2. Inelastic overlap function in momentum transfer space (25)

The inelastic overlap function $\mathcal{T}_{in}$ (s,t) can be directly solved from the experimental data. With a reasonable assumption of the elastic phase one can solve the Im T and Re T from the measured differential cr.s. and computes the elastic overlap integral by integrating over angular variables. Finally $\mathcal{T}_{in}$ (s,t) is obtained from

$$\mathcal{T}_{in}(s,t) = \mathrm{Im}\ T_{el}(s,t) - \mathcal{T}_{el}(s,t) \qquad (14)$$

This procedure has been applied to proton-proton data by the authors of Re (25) and the results are shown in Fig. (28). The results shown have been calculated by neglecting the real part of the elastic amplitude at all t values. Repeating the calculations with different phase assumptions they found that the results at small t are insensitive to the assumed phase, whereas at large t they are sensitive. A striking observation is that $\mathcal{T}_{in}$ changes sign at $t_0 \simeq -0.6\ \mathrm{Gev}^2$, the existence of the zero does not depend on the assumed elastic phase, and even the position of the zero is roughly independent of the phase "as long as the amplitude is dominantly imaginary in the forward direction". This observation means that the phases of the production amplitude cannot be neglected in computing $\mathcal{T}_{in}(t)$ because the zero of $\mathcal{T}_{in}(t)$ is sensitive not only to the absolute values but also to the phase.

The solid curve of Fig. (28) represents the parameterization of de Groot and Miettinen which contains a central and a peripheral component.

$$\mathcal{T}_{in}(t) = \sigma_D f_D(t) J_0(R\sqrt{-t}) + \sigma_\pi f_\pi \frac{2J_1(R\sqrt{-t})}{R\sqrt{-t}} \qquad (15)$$

The Central component ($\sim J_1(R\sqrt{-t})$ due to non-diffractive production, and the more peripheral component ($\sim J_0(R\sqrt{-t})$ due to diffractive processes. Both terms contain a modulating function of the momentum transfer, which takes into account that the non-diffractive (diffractive) production does not happen in a black disc (in a ring) of radius R, but in interaction volumes which have smooth edges.$^{(6)}$

Since the peripheral component is responsible for the forward peak in $d\sigma_{el}/dt$ it would connected naturally with the increasing cr.s. However here one should remember that the identification of the peripheral or central contribution with diffractive production is a matter of opinion, and a better understanding can come in going to b-space.

3. Inelastic overlap function in impact parameter space

(3.1) $G_{in}(s,b)$ (Henzi & Valin (28))

The first step in attempting to account for ISR data in terms of $G_{in}(s,b)$ was done by Heckman & Henzi (31). At that time the most comprehensive data available were the small $|t|$ data which revealed the slope-break at $|t| \simeq 0.13$ GeV^2 in $d\sigma_{el}/dt$. In Re (31) it was shown that this slope variation in $d\sigma_{el}/dt$ is accounted by $G_{in}(s,b) \equiv d\sigma_{in}/d^2b$ being a Gaussian in b-space, or equivalently by $d\sigma_{in}/dt$ being an exponential in t-space. The effect originating from the non-linearity of the relation.

$$d\sigma_{el}/dt = \left|\sqrt{\pi}\int_0^\infty \left(1-\sqrt{1-G}\right) J_0(b\sqrt{-t})\, b\, db\right|^2 \qquad (16)$$

The more recent data on $d\sigma_{el}/dt$ at large $|t|$ revealing the diffraction dip are not compatible with $d\sigma_{in}/d^2b$ being Gaussian exactly. To describe this dip structure, Henzi & Valin proposed a small correction "edge" term which produces a flattening (relative to the Gaussian) of the overlap function at small b.

$$G(s,b) = G_{Gau} + G_{edg} = P\, e^{-b^2/4B} + P_1\, b^2\, e^{-b^2/4B_1} \qquad (17)$$

The main results of Henzi & Valin analysis are the following

(i) Within uncertainties resulting from the experimental errors, the parameters p, P_1 and B_1 are energy independent, and $P\left(= \frac{d\sigma_{in}}{d^2b} \text{ at } b=0\right) \simeq$ 0.95 through ISR energies.

(ii) On the other hand "B" shows a clear cut increase with energy and the range of the Gaussian $\sqrt{4B}$ increases from 1 fm at the lowest ISR energy by 5% through ISR energies. (see Figs (29)).

(iii) $0 \leqslant G_{edg} \lesssim 0.1 \times G_{Gau}$ throughout impact parameter space and through ISR energies, and the maximum of G_{edg} is at $b = \sqrt{4B_1} \simeq$ 0.65 fm and G_{edg} has a width around this value of similar magnitude.

One particular consequence of (iii) is that the upward concavity of $d\sigma_{el}/dt$ is still due mainly to G_{Gau} form of $G_{in}(s,b)$ and unitarity mechanism as in eq. (16). On the other hand this Gaussian form of $G_{in}(s,b)$ at large b may not suffice to completely reproduce the local slope change in $\frac{d\sigma_{el}}{dt}$($\simeq$1.6) around t $\simeq$ - 0.13. In other words $G_{in}(s,b)$ has a tail at large b beyond that of the dominant Gaussian as we shall see next.

(3.2) $G_{in}(s,b)$ (H.I. Miettinen, (24, 33))

The inelastic overlap function extracted by Miettinen & Pirila (24) from direct Fourier - Bessel transformation of $d\sigma_{el}/dt$ at $\sqrt{S} = 53^{\text{Gev}}$ is shown in Fig (30a, 30b) together with the amplitude $\text{Im}h_{el}$ (s.b) and the eikonal Ω (s,b) defined by

$$h_{el}(s,b) = 2\left(1 - e^{-\Omega(s,b)}\right) \qquad (18)$$

The results of repeating the above analysis at the other ISR energies s = 21, 30, and 44 Gev are shown in Fig. (31a, 31b). The results of these analysis may be summarized as follows.

(i) Im $h_{el}(s,b)$ is very nearly a Gaussian over the b^2 range from 0 to 2 $(\text{fm})^2$, at larger impact parameter it levels off, this large b tail is directly related to the sharp break of the $d\sigma_{el}/dt$ at t $\simeq$ -0.13 Gev^2.

(ii) $G_{in}(s,b)$ bends down near b = 0, in t space, this corresponds to a zero of $\sigma_{in}(s,t)$ around t $\simeq$ - 0.6 Gev^2. Its interesting to notice that if $G_{in}(s,b)$ would not level off near b = 0, it would violate the unitarity limit. This suggest that absorptive effects are at least partially responsible for the small b flatting.

(iii) at b = 0, the value of $G_{in}(s,b)$ is (94 ±1)% of the maximum value allowed by unitarity (the black disc limit), it stays constant though the ISR energy range. The pronton gets bigger but not blacker as the energy increases.

(iv) The rise of the total cr.s. comes from a relatively narrow region around 1 fm.

(v) $G_{in}(s,b)$ has a central profile which peaks at $b = 0$

4. Impact Structure of inelastic diffraction

(4.1) $G(s,b)$ (N. Sakai & J.N.J. White (22))

As we have seen in the last sub-section that elastic scattering has a central profile, however inelastic diffraction, in which one or both of the colliding particles get excited, is probably a shadow process. We may then ask : what is its impact parameter distribution? Does it also peak at $b = 0$?

This problem has been studied in detail by Sakai and White (22) using ISR data (at $s = 930\ \text{Gev}^2$) on σ_{tot} & $d\sigma_{el}/dt$ and $\frac{d^2\sigma}{dt\,dM^2}$ (diffractive) as input. The unitarity now reads

$$Im\, h_{el}(s,b) = \frac{1}{4}\left|H_{el}(s,b)\right|^2 + G_D(s,b) + G_{ND}(s,b) \qquad (19)$$

where $G_d(s,v)$ and $G_{nd}(s,b)$ are the overlap functions for diffractive and non-diffractive final states and each satisfies $G(s,b) \geqslant 0$. The main results of this investigation are the following.

(i) The assumption of s-channel helicity conservation for the diffractive process leads to a diffractive overlap function which is central (root mean square radius $\simeq$ 0.5 fm)

(ii) The assumption of t-channel helicity conservation for the diffractive process leads to a peripheral profile for the diffractive overlap function (r.m.s. radius $\simeq$ 1 fm)

(iii) For both cases non-diffractive processes are peripheral (r.m.s. radius $\simeq$ 1 fm).

The experimental data of low mass diffractive production is known to be in rough agreement with t-channel helicity conservation and to completely disagree with s-channel helicity conservation. However the assumption of exact t-channel helicity conservation is actually not at all crucial for obtaining a peripheral G_d (s,b). Any combination of amplitudes with a "reasonable" amount of s-channel helicity flip amplitudes would give a peripheral result for G_d (s,b).

Finally the impact parameter distribution of the various overlap functions of eq. (19) are plotted in Fig. (32) for $\sqrt{s} = 30.5$ Gev in the case of t-channel helicity conservation.

4.2 Two Component Analysis of the inelastic overlap function

"Unabsorbed overlap function" (26, 27)

The measurements of the inclusive proton spectra at the NAL and the ISR show that at high energies inelastic diffraction and non-diffractive production populates different regions of the phase space. If we consider their contributions to the elastic amplitude separately, unitarity gives.

$$\mathrm{Im}\, T_{fi} = \tau_{el}(s,t) + \tau_{d}(s,t) + \tau_{nd}(s,t) \tag{20}$$

In the forward direction τ_d and τ_{nd} are well known, and they represent the two inelastic cr.s. components (e.g. at 200 Gev/c we have $\tau_d(s,0) = \sigma_D \simeq 7\ \mathrm{mb}\ \&\ \tau_{nd}(s,0) = \sigma_{\pi} \simeq 25\ \mathrm{mb}$).

Away from the forward direction one would like to ask how do these terms build up the t-dependence of the elastic amplitude, Does the two-component model valid for non-zero t values?

Analysis of this type have been done recently by the authors of Ref (26) using unabsorbed overlap function (as we saw earlier, the occurrence of zero in τ_{in} (s,t) at $t \simeq -0.6\ \mathrm{Gev}^2$ strongly suggests that absorptive corrections are important). The unabsorped overlap function H^0 (s,b) is defined through the unitarity relation (assuming the elastic amplitude is purely imaginary).

$$H_{el}(s,b) = |H_{el}(s,b)|^2 + S_{el}\, \overset{0}{H}_{in}(s,b) \tag{21}$$

$$= |H_{el}(s,b)|^2 + (1-2H_{el})\, \overset{0}{H}_{in}(s,b) \tag{22}$$

which gives
$$\overset{0}{H}_{in}(s,b) = \left[\frac{1-H_{el}(s,b)}{1-2H_{el}(s,b)}\right] H_{el}(s,b) \tag{23}$$

where with these normalization unitarity bounds are $0 \leqslant H_{in}(s,b) \leqslant \frac{1}{4}$

Inami et al (26) have constructed $\overset{0}{H}_{in}$ from the ISR data on $d\sigma/dt$ via eq. (23). At each energy the resulting $\overset{0}{H}_{in}$ is well fitted by the sum of two Gaussian in b-space or equivalent two exponential in t-space.

$$\overset{0}{H}_{in}(s,b) = \overset{0}{H}_{1}(s,b) + \overset{0}{H}_{2}(s,b) \tag{24}$$

$$= A_1 e^{-c_1 b^2} + A_2 e^{-c_2 b^2} \tag{25}$$

This simple decomposition suggest a two components interpretation, but before making any connection with diffractive and non-diffractive components, we must construct the correct amplitudes $H_{in:1}$ & $H_{in:2}$ which are given by

$$H_{in}(s,b) = \overset{0}{H}_{in}(s,b) - 2H_{el}(s,b)\, \overset{0}{H}_{in}(s,b) \tag{26}$$

In fact the properties of $H_{in:1}$, $H_{in:2}$, $\tau_{in:1}$ and $\tau_{in:2}$ deduced from this analysis over ISR energy range (at s = 550, 940, 2020, and 2840 GeV^2) are similar to those which one might expect from diffractive and non-diffractive components.

(i) $\tau_{in:1}$ (s, o) contributes almost a constant to σ_{in}, rising from 23.2 to 24.4 mb through the ISR energy range. $\tau_{in:1}$ (s, t) shows also significant shrinking with increasing energy; these properties of $\tau_{in:1}$ agree with multiperipheral expectations. On the other hand $\tau_{in:2}$ (s, t) has little shrinkage and its part of σ_{in} rises strongly with energy from 7.9 to 10.5 mb. These values ($\tau_{in:1}$ (s, o), $\tau_{in:2}$ (s, o)) lie so close to estimates of the non-diffractive and diffractive cr.ss. from triple-Regge analysis$^{(32)}$, and the association of $\tau_{in:1}$ (s, t) and $\tau_{in:2}$ (s, t) with the multiperipheral and diffractive component is strongly suggested.

(ii) In impact parameter space H^2_{in} (s, b) i.e. H_d (s, b), is central rather than peripheral, and it increases with energy. On the other hand the shrinkage causes H_{nd} (s, b) to decrease with energy for small b. However the contributions of these two components produce a net increase in H_{in} (s, b) which is peripheral, in agreement with the previous analysis (See Fig. (33a, 34 f)).

5. Summary & Conclusions

(i) The experimental data looked at in impact parameter space shows two properties: The long tail in b, which is directly related to the t slope increase, and the lack of any large deviation from a pure Gaussian shape in b at small b, which is directly related to the dip in $d\sigma_{el}/dt$ occurring at a large t where the cr.s. is very small.

(ii) The energy dependence of G_{in} (s, b) reveals two important results : the value of G_{in} (s, b = o) is essentially constant through ISR energy range, and the observed rise of proton - proton total cr.s. comes from the region around 1 fm.

$$\Delta\sigma_{in} = \int_0^\infty \Delta G_{in}(s,b)\, d^2b \qquad (27)$$

(iii) If the s-channel upper unitarity were saturated in a domain around b = o, then the increase of G_{in} (s, b) would necessarily have to be peripheral. Since the peripherality phenomenon does not originate from a saturation of this nature, we conclude that this phenomenon is a dynamical effect.

(iv) The inelastic overlap function of (Henzi & Valin) incorporates Geometrical scaling. On the other hand, in the inelastic overlap function of Inami et al, Geometrical scaling only happens approximately and by accident. Fig. (34) shows how the increase (s, b) through the ISR range is made up : only because of big cancellations between D and ND parts. However the question of Geometrical scaling will be regarded in detail in Chapter V.

(v) Why does the amount of s wave absorption stay constant at b = o, and why at the 94% level? If the diffractive overlap function G (s,b) is peripheral (the case of t-channel helicity conservation), does the increment of G (s, b) have the same peripheral nature? These questions and others will be examined in Chapter (VI).

CHAPTER FIVE

GEOMETRICAL SCALING IN PROTON - PROTON SCATTERING

Some time ago Dias de Deus$^{(36)}$ has suggested a scaling law for the inelastic overlap function of hadronic scattering reactions at high energies.

$$G(s,b) = G\ (b/R(s)) \tag{1}$$

Where R(s) is the interaction radius of hadrons involved, and contains all the energy dependence. This Geometrical scaling which was originally proposed in order to explain the observation of multiplicty scaling in inelastic collision (KNO-Scaling)$^{(42)}$, has a very interesting consequence for elastic scattering. Neglecting real part and spin effects, it follows from unitarity that the imaginary part of the impact parameter amplitude scales too

$$F(b,s) = F(b/R(s)) \tag{2}$$

Eq. (2) implies at once the scaling behaviour

$$d\sigma/dt = R^4 f\ (R^2 t) \tag{3}$$

$$\sigma_t \propto \sigma_{in} \propto \sigma_{el} \propto B\ (t=0) \sim R^2 \tag{4}$$

$$t_0 \sim R^{-2} \tag{5}$$

Where t_0 is the position of any particular feature "dip, maximum, break", and B is the slope parameter B (s, t) = d ($\ln d\sigma/dt$) / dt.

The t_0 property above is part of a more general prediction, that the shape of $d\sigma/dt$ does not change with s, - only the ordinate and abscissa change scale, as in eq. (3). In Sec. 1 and 2 of this chapter we derive a scaling low for the elastic differential cross section, from the geometrical scaling of the inelastic overlap function in the limit $\rho \longrightarrow 0$ (ρ is the ratio $\frac{\text{Re F}}{\text{Im F}}$), then we make a concrete comparisons and tests of geometrical scaling predictions eqs. (3,4,5) with proton-proton scattering data. The influence of the real part will be discussed in the final section.

1. Scaling law for the elastic differential cross section in pp scattering.(35)

Geometrical scaling of the inelastic overlap function states that:

$$G_{in}(b^2, s) \xrightarrow[s \to \infty]{} G_{in}(\beta) \qquad (6)$$

where

$$\beta \equiv \pi b^2/\sigma_{in} \qquad (7)$$

is the scaling variable.

In the shadow scattering limit, i.e. when the real part of the amplitude approximately vanishes at each impact parameter we have

$$\left[1 - \sqrt{1 - G_{in}(s, b^2)}\right]^2 = G^2_{el}(s, b^2) \qquad (8)$$

where $G^2_{el}(b^2, s)$ is the elastic overlap function. From eq. (8) we find that the geometrical scaling in the inelastic overlap function, implies geometrical scaling in the elastic one.

Since the ratio ρ of the forward real to imaginary part of the amplitude is consistent with being close to zero, $|\rho| \leqslant 1\%$. This makes it plausible to think that shadow scattering unitarity limit reach at ISR, at least for small angles. Using that approximation and neglecting spin effects we can show that geometrical scaling implies for the function

defined as
$$\Phi(s,\tau) \equiv \frac{1}{\sigma_{in}^{2}(s)} \frac{d\sigma_{el}}{d|t|} = \frac{1}{\sigma_{in}(s)} \frac{d\sigma_{el}}{d\tau} \qquad (9)$$

where

$$\tau = |t|\sigma_{in} \qquad (10)$$

The existence of the scaling limit

$$\Phi(s,\tau) \xrightarrow[\rho \to 0]{s \to \infty} \Phi(\tau) \qquad (11)$$

This scaling limit can be derived directly from unitarity

$$d\sigma_{el}/dt = \frac{4}{\pi} \left| \int_0^\infty db^2 \left(1 - \sqrt{1 - G_{in}(b^2, s)}\right) J_0(b\sqrt{|t|}) \right|^2 \qquad (12)$$

$$= \frac{4}{\pi} \left| \int_0^\infty db^2 \; G_{el}(s, b^2) \; J_0(b\sqrt{|t|} \right|^2$$

using

$$G_{el}(s, b^2) \xrightarrow[s \to \infty]{\text{Shadow}} G_{el}(\beta) \qquad (13)$$

eq. (12) gives

$$\Phi(\tau) = \frac{1}{4\pi} \left| \int_0^\infty d\beta \, G_{el}(\beta) \, J_0\left(\sqrt{\frac{\beta\tau}{\pi}}\right) \right|^2 \qquad (14)$$

Let us now make a quantitative comparison of the scaling limit(11) with the ISR data. This is shown in Figs. (35, a, b). The two curves in Fig. (35,a) represent the elastic differential cross section as a function of t at the lowest and highest ISR energies, the change of the curve with energy is clearly seen. On the other hand Fig. (35, b) shows the plot of

$$\Phi(s,\tau) \equiv \frac{1}{\sigma_{in}} \frac{d\sigma_{el}}{d|t|}$$

as a function of τ , for the same two curves of Fig. (35, a). The points every where fall into a unique curve showing that the scaling law (11) is in quantitative agreement with the data.

We end this section by giving some examples of models which possess Geometrical scaling.

(i) Froissart-saturating models:

If an amplitude asymptotically follows the Froissart bound:

$$\sigma_t \sim \ln^2 s$$

Then from the principles of axiomatic field theory, it was found(43) that in this case the amplitude must be an entire function of τ

$$\lim_{s\to\infty} F(s,t)\,/\,F(s,0) = f(\tau) \tag{15}$$

Thus those Eikonal models which asymptotically predict saturation of the Froissart bound, must satisfy, asymptotically, τ scaling. However the present data being on the one hand already consistent with τ scaling, are on the other hand not consistent with the black disc limit $\sigma_{el}/\sigma_{in} = 1$ predicted in most of the eikonal models. A more realistic value of σ_{el}/σ_{in} can be given by optical models, such as Grey disc model & Gaussian overlap function model.

(ii) Optical Models:

Optical models with fixed opacity can have geometrical scaling, but dynamical reasons for the radius and opacity remain to be found. In the case of Grey disc model we have

$$G_{el}(s,b^2) = (1-a)\,\Theta\,(R^2-b^2) \tag{16}$$

where geometrical scaling requires "a" to be constant. The elastic and inelastic cross sections are given by

$$\sigma_{el}/\sigma_{in} = \int_0^\infty d\beta \;\; G_{el}^2\,(\beta, s) \tag{17}$$

$$\sigma_{in} = \pi \int_0^\infty db^2 \, G_{in}(s, b^2) \tag{18}$$

From eqs. (16) (18) we find

$$\sigma_{in} = \pi R^2 (1 - a^2) \tag{19}$$

and eq. (16) can be written now in the form

$$G_{el}(s, \beta) = (1-a)\, \theta(1 - \beta(1-a^2)) \tag{20}$$

Using eq. (20) in eq. (17) we find

$$\sigma_{el} / \sigma_{in} = (1-a)/(1+a) \tag{21}$$

(a = o corresponds to a black disc)

Again Using eq. (20) in the scaling function eq. (14) gives

$$\Phi(\tau) = \frac{\sigma_{el}}{\sigma_{in}} \frac{1}{\tau} \left\{ J_1\left(\sqrt{\frac{\tau}{\pi(1-a^2)}}\right) \right\} \tag{22}$$

This example illustrates the way τ scaling can be introduced. The same sort of analysis in other optical models, gives constant σ_{el}/σ_{in}, and the τ scaling. However as we mentioned above in such models the dynamical reasons for the radius R(s) and opacity "constant" remain to be found.

2. Further Comparisons and Tests

Here we make a concrete comparison and tests of geometrical scaling predictions eqs. (3, 4, 5), with high energy proton-proton data. If the proton radius R(s) grows with energy, then geometrical scaling accounts for the growth of σ_t, constant cross sections and slope ratios σ_e/σ_t, B/σ_t

and the shrinkage of the forward elastic peak. The combined ISR data on σ_t , σ_{el} , and B_0 are compatible$^{(13)}$ with a $\ln S$ growth of R^2 (See Fig. 36).

$$R^2 = R_0^2 + R_1^2 \ln S$$

$$R_0 = 0.84, \; R_1 = 0.22 \text{ "fm"} \qquad (23)$$

Fig. (37, a, b) shows σ_{el}/σ_t , B/σ_t data, the predictions of geometrical scaling that these ratios remain constant, seems to hold down to about 100 Gev/c, below which σ_{el}/σ_t starts to rise and B/σ_t starts to fall. It is hard to see whether the pomeron term has geometrical scaling at lower momenta, since secondary terms get more important there.

The location of the diffraction dip, is predicted by geometrical scaling to move in towards smaller $|t|$ as σ_t increases.

$$t_{Dip} = \frac{c}{\sigma_t}. \qquad (24)$$

Also the ratio of $d\sigma/dt$ at the secondary maximum to $d\sigma/dt$ at t = o is predicted to be constant. Hence the rise of the secondary maximum is predicted to be

$$\left(\frac{d\sigma}{dt}\right)_{sec.Max.} = K\sigma_t^2 \qquad (25)$$

Comparison of eqs. (24) and (25) with the ISR data are made in Fig. (38).

Compatibility of slope parameters with geometrical scaling is conveniently examined through the relation.

$$\alpha_{eff}(s,t) - 1 = \left(1 + B\frac{t}{2}\right) d\ln R^2 / d\ln S \qquad (26)$$

The derivation of eq. (26) is straightforward. From geometrical scaling constraint eq. (3) we find

$$\frac{\partial}{\partial \ln s}\left(\ln\frac{d\sigma}{dt}\right) = \left[t\frac{\partial}{\partial t}\left(\ln\frac{d\sigma}{dt}\right) + 2\right]\frac{d\ln R^2}{d\ln S} \quad (27$$

Since the slope parameter, and the effective regge trajectory are given respectively by

$$B(s,t) \equiv \frac{\partial}{\partial t}\left(\ln \frac{d\sigma}{dt}\right) \tag{28}$$

$$2\alpha_{eff}(s,t) - 2 \equiv \frac{\partial}{\partial \ln s}\left(\ln \frac{d\sigma}{dt}\right) \tag{29}$$

In terms of these quantities eq. (27) gives eq. (26).

The left hand side of eq. (26) "effective regge trajectory" is relatively well determined by the data. We will treat the right hand side ($\alpha_{eff}(B, t)$) as the prediction of geometrical scaling for this quantity. We show in Fig. (39), $\alpha_{eff}(B,t)$ deduced from eq. (26) assuming the dependence of eq. (23).

$$R^2 = 0.765 + 0.048 \ln S \tag{30}$$

The empirical $\alpha_{eff}(s,t)$ calculated directly from the data are compared. The good agreement of $\alpha_{eff}(s,t)$ and $\alpha_{eff}(B,t)$ is evidence of geometrical scaling behaviour.(34)

Finally we would like to mention to an important remark concerning the quantity

$$\alpha_{eff}(s,0) = \varepsilon = \frac{d \ln R^2}{d \ln S} \tag{31}$$

This quantity is a critical parameter since it sets the scale for the geometrical scaling prediction. According to eq. (30) we find

$$\alpha_{eff}(s,0) = \frac{d \ln R^2}{d \ln s} = \frac{0.048}{0.765 + 0.048 \ln s} \tag{32}$$

$$\simeq 0.045$$

Some Problems

In Ref. (41, 39), A. Martin has done the same exercise as above. He found that $\alpha_{eff}(s,t)$ and $\alpha_{eff}(B,t)$ are not in agreement. This happens because his determination of the critical parameter ε

$$\alpha_{eff}(s,t) = \varepsilon\left(1+\frac{1}{2}Bt\right) \tag{33}$$

comes from a fit to the total cross section of the form

$$\sigma_t = A\, s^{\varepsilon} + B\, s^{-1/2} \tag{34}$$

A fit of this form down to S = 15 Gev^2 gives $\varepsilon = 0.07$. A comparison of the empirical $\alpha_{eff}(s,t)$ and $\alpha_{eff}(B,t)$ with $\varepsilon = 0.07$" is shown in Fig. (40). It is apparent from this figure that geometrical scaling predicts roughly 50% more energy dependence than is seen, and the geometrical scaling hypothesis disagrees with the data from $|t| \approx 0.4$ to 1.25 $(\text{Gev}/c)^2$.

Similar in compatibilities(37) of slope parameters with geometrical scaling are seen in the table below. Whereas the slope in the very extreme forward direction (B_0 and B_1) are compatible with geometrical scaling, the slope B_2 is not. This problem is not removed by Kroll's modification "which we discuss next" since the value of the real part of the amplitude in this t range are too small to effect the results.

$\sqrt{s}$	σ_t	$B_0(t\to 0)$	$B_1(\lvert t\rvert < 0.15)$	$B_2(.15 \leq \lvert t\rvert \leq .4)$
23.5	39.1 ± .4	11.8	11.57 ± .30	10.42 ± .17
30.6	40.5 ± .5	12.3	11.87 ± .28	10.91 ± .22
44.9	42.5 ± .5	12.8	12.87 ± .20	10.83 ± .20
52.8	43.2 ± .6	13.1	12.40 ± .30	10.80 ± .20

3. The Influence of the Real Part. "Kroll's modification"

In many investigations (e.g. Chapter IV), the overlap function of proton-proton scattering have been studied at ISR energies neglecting the real part and spin effects. The next step towards a complete analysis is the inclusion of the real part. The authors of Ref. (44) have calculated the real part using a dispersion relation between the modulus and the phase of the crossing symmetric part of the amplitude and assuming Regge behaviour for the crossing add part. Fig. (41) shows the principal behaviour of the real part in t and b space. Using these results, the inelastic overlap function has been evaluated via the unitarity relation

$$G_{in} = \mathrm{Im}\,\tilde{F} - \frac{1}{4}|\tilde{F}|^2 \qquad (35)$$

where $\tilde{F}$ denotes the impact parameter amplitude, and the resulting overlap function has the same features which we knew before "the tail at large b, the peripheral increase with energy". The most interesting point here is the energy dependence of G_{in} and $\mathrm{Im}\,\tilde{F}$ at b = o. This is shown in Fig. (42). From this figure one reads that G_{in} – and not Im $\tilde{F}$ – is constant from 50 to 1500 Gev/c, while Im F at b = o is constant only in the ISR region. The difference between both functions is due to the real part. Solving eq. (35) for Im$\tilde{F}$ we find

$$\mathrm{Im}\,\tilde{F} = 2\left\{1 - \sqrt{1 - G_{in} - \frac{1}{4}(\mathrm{Re}\,\tilde{F})^2}\right\} \qquad (36)$$

Although the real part is small, it is not negligible in eq. (36) at b = o because " $1-G_{in}$ " at b = o is small too. However at larger b Re $\tilde{F}$ is completely negligible so that both functions behave similarly.

From the above analysis it turns out the G_{in} (and not Im $\tilde{F}$) exhibits geometrical scaling above 50 Gev. From this geometrical scaling follows only

$$\sigma_{in} \sim R^2 \tag{37}$$

whereas all other relations

$$\sigma_t\,,\ \sigma_{el}\,,\ B_0\,,\ \sim R^2 \tag{38}$$

which follows from perfect geometrical scaling are disturbed by the real part, as we shall see next.

(i) The total cross section.

Expanding eq. (36) with respect to $\sqrt{1-G_{in}}$ gives

$$\mathrm{Im}\,\tilde{F} \simeq 2\left\{1-\sqrt{1-G_{in}}\right\} + \frac{1}{4}\,\frac{\mathrm{Re}\,\tilde{F}^2}{\sqrt{1-G_{in}}} \tag{39}$$

The first term in the right hand side scales if G_{in} does

$$\mathrm{Im}\,\tilde{F} = \mathrm{Im}\,\tilde{F}_{GS} + \frac{1}{4}\,\frac{\mathrm{Re}\,\tilde{F}^2}{\sqrt{1-G_{in}}} \tag{40}$$

Hence

$$\mathrm{Im}\,F = \mathrm{Im}\,F_{GS}\left\{1+\frac{p}{8\,\mathrm{Im}\,F_{GS}}\int b\,db\,J_0(b\sqrt{-t})\,\frac{\mathrm{Re}\,\tilde{F}^2}{\sqrt{1-G_{in}}}\right. \tag{41}$$

(where p is the momentum of the incoming particle in the stationary target system)

At t = o, the real part gives a positive correction to Im F "stronger at smaller energies, weaker at higher energies" which makes σ_t behaves not similar to σ_{in} and produces actually a minimum in σ_t around 150 Gev (see Fig. (43)).

(ii) The slope parameter

If the slope parameter is given by

$$B = 2\,\frac{1}{\mathrm{Im}\,F}\,\frac{d}{dt}\,\mathrm{Im}\,F\Big/_{t=0} \tag{42}$$

eq. (41) gives

$$B = 2\,\frac{1}{\mathrm{Im}\,F}\,\frac{d}{dt}\,\mathrm{Im}\,F_{GS} + \frac{p}{16\,\mathrm{Im}\,F}\int b^3 db\,\frac{\mathrm{Re}\,\tilde{F}^2}{\sqrt{1-G_{in}}} \tag{43}$$

Since the first term on the right hand side dominates, we find

$$B = B_{GS}\,\frac{\mathrm{Im}\,F_{GS}}{\mathrm{Im}\,F} \simeq B_{GS}\left\{1 - \frac{p}{8\,\mathrm{Im}\,F_{GS}}\int b\,db\,\frac{\mathrm{Re}\,\tilde{F}^2}{\sqrt{1-G_{in}}}\right. \tag{44}$$

So, the real part gives the same amount of correction to B_{GS} and $\sigma_{t:GS}$ but positive correction to $\sigma_{t:GS}$ and negative one to B_{GS}. This makes σ_t flatter than σ_{in}, and B steeper than σ_{in}, and gives

$$\sigma_t B/\sigma_{in} \sim B_{GS} \sim R^2 \tag{45}$$

This relation is tested in Fig. (44). It can be seen that it works very well. However at ISR energies, the real part is relatively small, and both types of geometrical scaling that is Gs of G_{in} and Gs of Im F, agree within the errors.

CHAPTER SIX

The origin of the rising cross-section

In this chapter we consider the question of the rising cross-section. A possible explanation of this rise ($500 \lesssim s \lesssim 3000$ Gev^2) is the presence of threshold effects. In the first section we show that the contribution to the total cross-section of single diffractive dissociation into high missing mass (M) exhibits a logarithmic threshold increase with energy.(19, 32, 18) The delayed threshold of this effect arises from the simultaneous constraints M^2, S/M^2 both large, and probably correspond to a threshold energy somewhat below $S \simeq 200$ Gev^2.

In Section 2, we discuss another possible threshold mechanism "Nucleon-Anti Nucleon" production(47, 56, 57). The delayed threshold in this case is due to the heavy masses of the $N\bar{N}$ pairs. In section 3 the question of the rising cross-section is re-examined (with theresults of Chapter IV in mind) in impact parameter-space. And finally we present our conclusion in section 4.

1. Rising cross-section and triple pomeron.

In view of the success of the "two component model" in accounting for the observed properties of high energy multi particle production, it was natural to try and see whether it can also account dynamically for the total cross-section behaviour. The fact that the diffractive component "with a large rapidity gap" is considerably smaller than the short-range-correlation component "no large rapidity gaps" suggests the possibility of a perturbative expansion of the high energy total cross-section.(19-18) (45)

If we assume that the (SRC) is described by a "bare pomeron" (by bare pomeron we mean the physical pomeron that governs the cross-section at intermediate energies, while we regard the re-normalized one, as the one which governs the asymptotic behaviour) one predicts a recurrence of the pomeron pole at high energies, as in the figure below. The triple pomeron contribution is the first term in this recurrence series, and therefore confirmation of its presence and an estimation of its magnitude goes a long way towards specifying the series. This series "renormalize" the position of the input pomeron pole. However, because of the smallness of the triple-pomeron coupling we need only to consider single diffraction into high mass, in the ISR energy range.

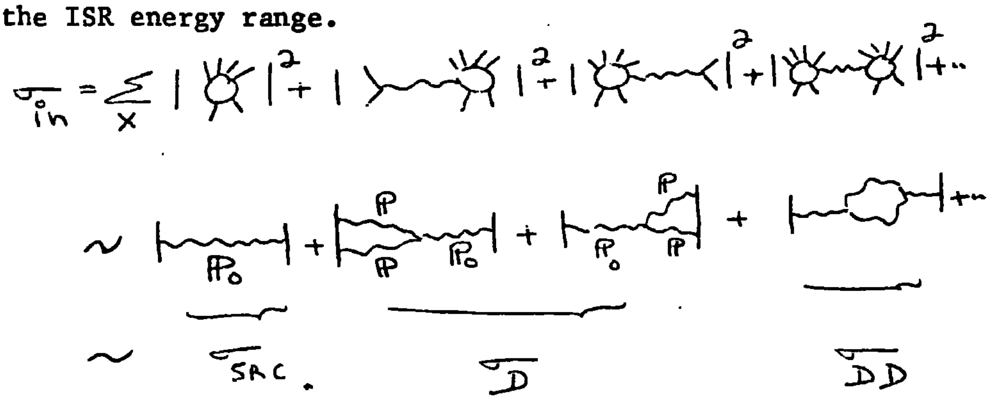

"Fig. 1 "

The (SRC) component "Zeroth order in the triple pomeron coupling" has the following contribution to the total cross-section

$$\sigma_{SRC} = \beta^2_{pp\mathbb{P}}(0)\, s^{\alpha_0(0)-1} \tag{1}$$

This term accounts for the approximately constant proton-proton cross-section in the region 30-100 Gev^2. However at higher energies diffractive dissociation into high-mass states becomes possible. The triple Regge expression for this gives (taking $\mathbb{P}_0 \simeq \mathbb{P}$).

$$\sigma_D = 2 \int_{M_0^2}^{M_1^2} dM^2 \int_{-\infty}^{t_{min}} dt\, \frac{s_0}{s^2}\, \frac{G_{\mathbb{P}}(t)}{16\pi} \left(\frac{s}{M^2}\right)^{2\alpha_{\mathbb{P}}(t)} \left(\frac{M^2}{s_0}\right)^{\alpha_{\mathbb{P}}(0)} \tag{2}$$

$$G_{\mathbb{P}}(t) = \beta^2_{pp\mathbb{P}}(t)\,\beta_{pp\mathbb{P}}(0)\,|\xi_{\mathbb{P}}(t)|^2\,g_{\mathbb{P}\mathbb{P}\mathbb{P}}(t) \tag{3}$$

$$t_{min} \simeq -m^2 (M^2/s)^2$$

m being the nucleon mass

where $\beta_{pp\mathbb{P}}(t)$ is the pomeron, proton coupling, $\xi_{\mathbb{P}}$ is the pomeron signature factor, and $g_{\mathbb{P}\mathbb{P}\mathbb{P}}(t)$ is the triple pomeron coupling.

The factor 2 in eq. (2) arises from the fact that either proton may be diffractively scattered.

The lower limit " M_0^2 " should be chosen high enough to make the pomeron dominance an adequate approximation in eq. (2). The upper limit comes from the fact that we are considering terms with one large rapidity gap.(18) If we let Δ be the minimum gap length which defines a large rapidity gap, then this implies $M_1^2 < rS$ where

$$r \simeq e^{-\Delta} \tag{4}$$

eq. (2) becomes "replacing also $t_{min} \simeq 0$ ".

$$\sigma_D = 2\int_{M_0^2}^{rS} dM^2 \int_{-\infty}^{0} dt\, \frac{s_0}{s^2}\, \frac{G_{\mathbb{P}}(t)}{16\pi} \left(\frac{s}{M^2}\right)^{2\alpha_{\mathbb{P}}(t)} \left(\frac{M^2}{s_0}\right)^{\alpha_{\mathbb{P}}(0)} \tag{5}$$

Assuming a linear trajectory for small t with

$$\alpha_{P_0}(0) \simeq \alpha_{\mathbb{P}}(0) \simeq 1 \tag{6}$$

$$\alpha_{\mathbb{P}}(t) \simeq 1 + \alpha'_{\mathbb{P}}\,t$$

The integration of eq. (5) over M^2 gives:

$$\sigma_D = \frac{2}{(16\pi)(2\alpha'_{\mathbb{P}})} \int_{-\infty}^{0} dt \, \frac{G_{\mathbb{P}}(t)}{t} \left\{ \left(\frac{s}{M_0^2}\right)^{2\alpha'_{\mathbb{P}} t} - r^{-2\alpha'_{\mathbb{P}} t} \right\} \tag{7}$$

Assuming a rapid fall off of the couplings $G_{\mathbb{P}}(t)$, we can expand the term in brackets about $t \doteq 0$ in eq. (7), and we find:

$$\sigma_D = \frac{2}{16\pi} \overline{G_{\mathbb{P}}(t)} \ln \frac{rs}{M_0^2} \tag{8}$$

where

$$\overline{G_{\mathbb{P}}(t)} \equiv \int_{-\infty}^{0} dt \, G_{\mathbb{P}}(t) \tag{9}$$

We see from eq. (8) that the cross-section of single diffractive dissociation into high masses, shows a logarithmic rise with energy, regardless of the function form of $G_{\mathbb{P}}(t)$. This result is correct to a good approximation over a finite energy range. The detailed functional form of $G_{\mathbb{P}}(t)$ will, however, affect the asymptotic behaviour for very large s. If we choose vanishing triple pomeron coupling i.e.

$$G_{\mathbb{P}}(t) = -G'_{\mathbb{P}}(0) \, t \, e^{bt} \tag{10}$$

eq. (7) gives

$$\sigma_D = \frac{2 G'_{\mathbb{P}}(0) \ln (rs/M_0^2)}{16\pi \left[b + 2\alpha'_{\mathbb{P}} \ln\left(\frac{s}{M_0^2}\right)\right]\left[b - 2\alpha'_{\mathbb{P}} \ln r\right]} \tag{11}$$

Thus vanishing of the triple pomeron coupling, prevents an unbounded increase of σ_D and avoid eventual violation of the Froissart bound.

But the analysis of the data "e.g. Roy & Roberts. Ref 32" shows no evidence for the vanishing of $G_{I\!P}(t)$, at least down to $t \simeq -0.05$ Gev^2. In fact rather than any tendency to turn over, the data seems to show a sharping at small t values. If we choose a non-vanishing triple pomeron i.e.

$$G_{I\!P}(t) = G_{I\!P}(0)\, e^{bt} \tag{12}$$

eq. (7) gives

$$\frac{\sigma}{D} = \frac{2 G_{I\!P}(0)}{32\pi\alpha'_{I\!P}} \ln \frac{b + 2\alpha'_{I\!P}\ln\left(\frac{s}{M_0^2}\right)}{b - 2\alpha'_{I\!P}\ln r} \tag{13}$$

which gives asymptotically " i.e $2\alpha'\ln s \gg b$ " a slow ln (lns) increase. But to extent that

$$2\alpha'_{I\!P}\ln\frac{s}{M_0^2} \ll b \tag{14}$$

(Which seems likely to be satisfied at NAL and perhaps at ISR energies, because of the small values of α'), both eqs. (13) (11) give a direct logarithmic increase, as in eq. (8). When the energy increases from s1 to s2, eq. (8) gives:

$$\Delta\frac{\sigma}{D} = \frac{2}{16\pi}\,\overline{G_{I\!P}(t)}\,\ln\frac{s_2}{s_1} \tag{15}$$

Let us now illustrate how this lns increase in eq. (15) comes about using the Feynman variable X,

$$X = 1 - \frac{M^2}{s} \tag{16}$$

Since the upper limit for M^2 is $\overset{*}{M}^2 < rs$, we find that the lower cut-off "X_o" in X plot is independent of the energy:

$$X_o = 1 - \frac{\overset{*}{M}^2}{s} \simeq 1 - \frac{rs}{s} = 1 - r = 1 - e^{-\Delta} \qquad (17)$$

On the other hand the upper limit in x plot is given by

$$X_i^{max} = 1 - \frac{M_o^2}{S_i} \qquad \text{" } M_o^2 \text{ fixed"} \qquad (18)$$

So for the energy S_1 the region of integration is from X_o to X_1, while for the energy S_2, the region of integration is from X_o to X_2, i.e. as S increases the threshold on a $\frac{M^2}{s}$ plot moves closer to zero, (we are integrating up closer to X = 1). This means that the triple pomeron term, picks up an extra contribution giving an appreciable increase to σ_D (Fig. 45).

According to the analysis of "Roy & Roberts, Ref. 32, and Amati et al, Ref. 19", the net increase "$\Delta\sigma_D$" respectively is

$$\Delta\sigma_D\,(P_{Lab} = 200 \longrightarrow 2000\ GeV/c) = 3.3\ mb$$

$$\Delta\sigma_D\,(2800 \quad 6 \quad 600\, GeV^2 \qquad) = 2.7\ mb$$

Taking into account the numbers obtained by various people who have played this type of game, it may be tempting to suggest diffraction as the mechanism for the total cross-section rise. However, even if we grant the numerical equality $\Delta\sigma_D \simeq \Delta\sigma_{in}^{o}$, [$\Delta\sigma_{in}$ over the same energy range is 3.8 ± 0.8), the situation is still far from clear as we shall see from the following models.

(i) D. Amati et al:(19)

In this model we have

$$\alpha_{\mathbb{P}}(0) = 1 \quad , \quad g_{\mathbb{P}\mathbb{P}\mathbb{P}}(0) \neq 0 \qquad (19)$$

This gives a constant σ_{ND} and the entire rise in the inelastic cross-section comes from σ_D. The lns term in σ_D, together with higher order terms (double and higher diffractive events will become detectable at even higher energies and will contribute with higher powers of lns), will inevitably lead to a renormalization of the pomeron trajectory and to a violation of the Froissart bound. This problem was treated in Ref. 19, by introducing elastic absorption in order to restore the Froissart bound, without effecting the energy dependence appreciably at ISR.

(ii) Blankenbeder.(55) (32)

This model can also be described by the series expansion of Fig. 1, it has an explicit prescription for taking into account absorption due to the elastic and diffractive channels. The elastic diffraction causes absorption is already rather generally believed. Blankenbecler(55) argued that also inelastic diffraction should give rise to absorption. This mean, in essence, that one subtracts from σ_{ND} of Fig. 1, the terms of Fig. 2 below, corresponding to initial state absorption, and an identical set of diagrams for final state absorption.

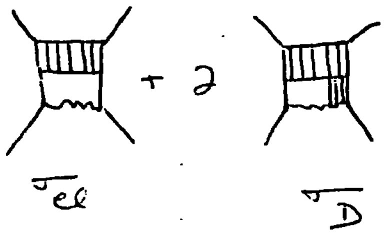

Fig (2) : Absorptive corrections to the cross-section, according to the model of Blankenbecler.(55)

Thus σ_{ND} is given by

$$\sigma_{ND} = \beta^2_{PP\mathbb{P}}(0)\; s^{\alpha_{\mathbb{P}}(0)-1} - 2\left[\sigma_{el} + \sigma_{D}\right] \tag{20}$$

So, if $\alpha_{\mathbb{P}}(0) = 1$ and if σ_D would rise, then the inelastic cross-section would go down and not up. In order to prevent σ_{inel} from going down, one needs an alien mechanism "non-diffractive" which must give an increase more than σ_D to re-produce the rise in σ_{inel}. This mechanism could be the opening up of new non-diffractive channels which amounts to assuming a bare pomeron intercept $\alpha_{\mathbb{P}}(0) > 1$.

(iii) Bishari et al.$^{(54)}$

In this model, we start with $\alpha_{\mathbb{P}}(0)$ less than unity, so we get asymptotically a consistent solution. The non-diffractive cross-section now is given by

$$\sigma_{ND} = \beta^2_{PP\mathbb{P}}(0)\; s^{\alpha_{\mathbb{P}}(0)-1} \simeq \beta^2_{PP\mathbb{P}}(0)\; s^{-\Delta} \tag{21}$$

And the rise in the diffractive cross-section, is exactly compensated by the fall in the non-diffractive cross-section. Thus the entire rise in σ_{incl} has to be attributed to some alien source - e.g. Nucleon - Anti Nucleon production.

2. Rising cross-section $\rightsquigarrow$ $N\bar{N}$ production

As we mentioned in the preceding section, the work of Blankenbecler has given sufficient reasons for believing that, the rise of proton-proton total cross-section at ISR is non-diffractive in origin. On the other hand, the analysis of M. Antinucci,$^{(58)}$ shows that the $\bar{P}$ production cross-section increases by $\sim$ 6mb at ISR. This observation led several authors$^{(47,56,57}$

to the suggestion that this might be the cause of the total cross-section rise. Here we study this phenomenon assuming that the production of $N\bar{N}$ takes place Multiperipherally.$^{(47)}$

To start with let us consider the following decomposition of the non-diffractive proton-proton total cross-section

$$\sigma_{ND}^{tot} = \sigma^{(0)} + \sigma(N\bar{N}) \tag{1}$$

$$\sigma(N\bar{N}) \equiv \sum_{i=1}^{\infty} \sigma^{(i)} \tag{2}$$

Where we have assumed in eq. (1), that $N\bar{N}$ production is purely non-diffractive, "Since both the $N\bar{N}$ production and diffraction are small, at ISR we ignor their interference". The superscript in eqs. (1) (2) denotes the number of $N\bar{N}$ pairs present in the final state.

The behaviour of $\sigma(N\bar{N})$

To estimate the $\sigma(N\bar{N})$, we consider the multiplicity sum rule,

$$\langle n\rangle_{\bar{N}}\,\sigma_{tot} = \sum_{i=1}^{\infty} i\,\sigma^{(i)} \tag{3}$$

$$= \int dp\left(\frac{d\sigma_{\bar{p}}}{dp} + \frac{d\sigma_{\bar{n}}}{dp}\right) \tag{4}$$

It is more useful for our purpose here to define a different average multiplicity by normalizing with respect to $\sigma(N\bar{N})$.

$$\langle N\rangle\,\sigma(N\bar{N}) = \sum_{i=1}^{\infty} i\,\sigma^{(i)} \tag{5}$$

$$= \langle n \rangle_{\bar{N}} \, \sigma_{tot} \qquad (6)$$

Assuming that $\frac{d\sigma_{\bar{p}}}{dp}$ and $\frac{d\sigma_{\bar{n}}}{dp}$ are nearly equal, eq. (4) gives

$$\langle N \rangle \sigma(N\bar{N}) \simeq 2 \int dp \, \frac{d\sigma_{\bar{p}}}{dp} \qquad (7)$$

The quantity $\langle N \rangle$ is the average number of $N\bar{N}$ pairs produced for events in which at least one pair is produced, hence $\langle N \rangle \geqslant 1$. Following the analysis of ref. (58), the right hand side of eq. (7) is shown in fig. (46). Therefore, once $\langle N \rangle$ is known, $\sigma(N\bar{N})$ can be found.

Assuming that $\langle N \rangle$ remains near unity, it follows from Fig. (46) that for $s \lesssim 500$ Gev^2 $\sigma(N\bar{N})$ is less than 4mb, and for $s \simeq 3000$ Gev^2, it can be as large as 10.2 mb. Thus the increase $\Delta\sigma$ in $\sigma(N\bar{N})$ over the ISR energies is approximately 5-6 mb. However $\Delta\sigma(N\bar{N})$ will be less if $\langle N \rangle$ increases above unity.

Fig. (46) has another important piece of information: the $\bar{p}$ production is negligible below $s \simeq 100$ Gev^2. This delayed threshold, and the assumption that $\langle N \rangle$ remains near unity up to ISR energies can be understood by assuming the $N\bar{N}$ production takes place multiperipherally.

Fig. (47.a) shows the production of a $N\bar{N}$ pair in the central region "the $\bar{p}$ distribution is strongly peaked toward the central region". The MP kinematics can be described by a (highly simplified) constraint,

$$\left(\frac{s_1}{s_0}\right)\left(\frac{M^2}{s_0}\right)\left(\frac{s_2}{s_0}\right) \simeq \frac{s}{s_0} \qquad (8)$$

If we take the threshold for each sub-energy ~ 4 Gev^2, the MP threshold for single $N\bar{N}$ pair production is ~ 64 Gev^2" with $s_0 = 1$ Gev^2". This rough estimate is numerically too low. Typically only above $s = 200$ Gev^2 $N\bar{N}$ production is important.$^{(53)}$

The configuration for producing $2 N\bar{N}$ pairs, Fig (47.b), can be analysed in the similar manner, and one finds that the dynamical threshold in this case is at $s \simeq 3500$ Gev^2, just beyond the highest ISR energies.

The behaviour of $\sigma^{(o)}$.

Since $N\bar{N}$ production is small below the NAL energies, the success of the two-component picture indicates that $\sigma^{(o)}$, the component of σ_{ND} without $N\bar{N}$ pairs, is already smoothly behaved at $s \sim 200$ Gev^2. Therefore the production of pions and kaons alone generate a "bare pomeron" with intercept α_o, where both theoretical arguments and numerical estimates indicate that this bare pomeron has to be below $J = 1.$(56) This α_o is the bare pomeron used in the perturbative treatment of high energy collision at ISR.(56.18) The important question now is: how $\sigma^{(o)}$ behaves as we move into the ISR energy range. Chung- I Tan(47) argued (from the additive property of the MP models, together with the observation that $\sigma^{(o)}$, is already smoothly behaved at NAL), that an increase in $N\bar{N}$ production does not lead to a corresponding decrease in the rest of the non-diffractive cross-section.

Decomposition of the intercept of the pomeron

Fig (48) shows σ_{ND}, $\sigma(N\bar{N})$, $\sigma^{(o)}$ (according to the analysis of D. Morrison "σ_{ND}", and Chung-I Tan "$\sigma(N\bar{N})$", ref. 47). From this figure we see that the energy dependence of $\sigma^{(o)}$ from 3 to 3000Gev^2 can be characterized by

(i) A Regge term with an effective intercept $\bar{\alpha} \simeq 0.82$ for $s \leqslant 30$ Gev^2.

(ii) a reasonably flat region between 30 and 130 Gev^2.

(iii) another Regge term with an intercept $\alpha_o \simeq 0.87 - 0.92$ for s between 130 and 3000 Gev^2.

Since the intercept of the pomeron is decomposed into the contributions of different hadrons produced through the MP chain, the above picture, if correct, provides an explicit illustration on how the pomeron is "dressed" by the opening of new channels. It owes its "birth" to the pion production, yielding an intercept $\bar{\alpha} \simeq 0.82$ (the naked pomeron). Due to the $K\bar{K}$ production after 30 Gev^2, it is "renormalized" upward to α_0 by approximately 0.1 unit in J-plane, (the bare pomeron). Eventually, $N\bar{N}$ and other possible heavy particle production "renormalized" this bare pomeron to a "slightly - dressed one", $\alpha_{\mathbb{P}}$.

If it happens that the sum of $\alpha_{\mathbb{P}}(0, \pi)$ and $\alpha_{\mathbb{P}}(0, K\bar{K})$ almost saturate unitarity, so that with $\alpha_{\mathbb{P}}(0, N\bar{N})$ added, $\alpha_{\mathbb{P}}(0)$ would exceed unity, the $N\bar{N}$ production or part of it would cause superficial violation of the Froissart bound transiently, i.e. the behaviour of σ_t over the ISR energy range is a transient, rather than asymptotic phenomenon.

3. Rising cross-section in impact parameter space.

The results of Chapter IV "overlap function model" clearly provides strong constraints on models which proposed to explain the rise of the total cross-section at ISR. Any model proposed to explain this rise, must also be able to explain its impact parameter distribution (the observed rise of the proton-proton total cross-section comes from the region around $b \simeq 1$ fermi). Here we examine the two mechanisms of section 1 & 2 and some others from this point of view.

(i) central dynamics - peripheral rise$^{(24)}$

According to this mechanism the peripheral nature of the overall increment of the inelastic overlap function is interpreted as due to the sum of

1. a new central channel$_s$ opening up "which cause the rise of σ_{inel}". and
2. a typical Regge term "i.e. $\frac{d\sigma_{el}}{dt}$ shrinks, σ_{inel} stays constant", which gives in impact parameter space a decreasing central absorption together with expanding radius.

Figs. (49,a,b,c) show how the new central channels could easily compensate the decrease of the central absorption and make the overall increment of the inelastic overlap function, ΔG_{in} (s, b), peak at 1 fermi.

The extraordinary constancy of G_{inel} (s, b = o) "0.94" at ISR which comes from the new channels opening up and the shrinkage of the bulk of the cross-section, can be re-produced by using pomeron pole $\alpha_{P}(t) = 1.06 + 0.35\, t$. To clarify this point we refer to Fig. (50) which shows G_{inel} (s, b = o) as a function of the energy. The figure also shows a curve calculated using the above pomeron pole (the central production is effectively described by talking the pomeron intercept to be above one). From this curve we see that G_{in} (s, b = o) is decreasing at low energies, and passing though a broad minimum (0.94) at ISR energies. At energies above ISR G_{in} (s, b = o) will probably rise and finally slowly saturate the unitarity limit.

(ii) Geometrical scaling.

Geometrical scaling states that (Chapter V)

$$G_{in}(s,b) \longrightarrow G_{in}\left(\frac{b}{R(s)}\right)$$

We saw in Chapter V that the data satisfy Geometrical scaling, e.g. the four curves of figure (31 a) which represent G_{in} (s, b) at $\sqrt{s}$ = 21, 31, 44 and 53 Gev, can be put on the top of each other, if we scale them by a suitable s dependent radius. However, in spite of the experimental success of Geometrical scaling, we don't know whether it is systemic or an accident. For instance, the constancy of G_{in} (s, b = o) according to the above mechanism, only happens because of the big cancellation between the central channels and Regge behaviour term.

(iii) $N\bar{N}$ production.

We saw in section 2, with the context of MP model that this phenomenon could even account for the whole observed increase in σ_{in}. However, in impact parameter-space it is hard to see, if the model can describe properly the impact structure of ΔG_{in} (s,b), since it is not even known if the model can fit the shape of G_{in} (s,b)$^{(24)}$.

Alternatively, from geometrical picture point of view, in which heavy particles (e.g. $N\bar{N}$) are expected to be produced in a "head-on" collision. The peripherality of ΔG_{incl} (s,b) can be obtained from this central $N\bar{N}$ production, with the compensation mechanism described in (i).

(iv) Inelastic diffraction.

The inelastic diffractive overlap function of Sakai & White (Chapter IV) has a peripheral impact parameter structure (in the case of t-channel helicity conservation). This fits well with the picture of diffraction being the cuase for the rise of σ_{incl}. However, even if the overlap function G_D (s, b) is peripheral, this by no means would guarantee the peripherality of ΔG_D (s, b). If ΔG_D (s, b) has the same peripheral nature as G_D (s, b), a qualitative understanding of the mechanism which attributes the rise in σ_{incl} to inelastic diffraction, can be obtained. No quantitative calculations of the increment of the diffractive overlap function exist at present.

On the other hand the "Two component analysis of the inelastic overlap function" (Chapter IV), suggests a central diffractive component and a multiperipheral one. The multiperipheral component is more peripheral and shows significant shrinking with increasing energy.

The peripheral nature of the overall increment of the inelastic overlap function can be interpreted again as due to the increasing central component together with the shrinking multiperipheral part. Thus although the rise in inelastic cross-section can be attributed to a central diffractive component, the net increase can still be peripheral.

4. Conclusion

In conclusion we feel that it may well be that there is no simple explanation for the rise of the total cross-section in terms of a particular isolated set of processes, but the rise is a much deeper collective effect.

In impact parameter space, the rise of the total cross-section comes from the region around $b \simeq 1$ fm. we emphasize here again that this peripherality phenomenon is a dynamical effect, since the central absorption does not saturate the unitarity limit. The inelastic overlap function may be written (Chapter IV) as the sum of "disk" plus "ring" components, and the peripheral increment of the inelastic overlap function may come from an expanding "disk" component with radius $\simeq$ 1 fm, or from a growing "ring" component centred at 1 fm.

The association of "disk" or "ring" components with diffractive or non-diffractive productions is model dependent (e.g., in the inelastic overlap function of Sakai & White it is possible to identify the "ring" component with inelastic diffraction and the "disk" component with non-diffractive production). The question of the physical origin of the rising cross-section is one of the most interesting problems of hadron's today, and by solving it we hope that we will be able to learn a lot about hadron physics.

REFERENCES

1. A.N. Diddens XVII International Conference on high energy physics London (1974) (41-70).

2. C.W. Akrelov et al, preprint Michigan (UM-HE-74-20 (1974) paper 492 submitted to Ref (1).

3. Measurements of elastic scattering of hadrons on protons from 50 to 175 Gev/c, FERMILAB-Pub 75/48-EXP 7100.096.

4. U. Amaldi et al, phys. lette. 43B (1973) 231.

5. Recent experimental results from the CERN-ISR, FERMILAB-Pub-74/106-Exp 2000,000.

6. U. Amaldi,elastic and inelastic processes at ISR, NP internal report 73-19 (1973).

7. U. Amaldi et al, phys. lette. 44B (1973) 112.

8. G. Barbiellini et al, phys. lette. 39B (1972) 663.

9. S.R. Amendolia et al, phys. lette 44B (1973) 119.

10. P.D.B. Collins et al, Nucl. phys. B80 (1974) 135-163.

11. A. Martin, high energy theorem of particle-particle and particle-antiparticle scattering and the ISR data. In "the pomeron" proceeding of the Eighth Rencontre de Moriond France, March 1973.

12. U. Amaldi, Elastic scattering and low multiplicities in "Second International Conference on Elementary Particles" Aix-En-Provence, Sept. 1973.

13. V. Barger, Reaction mechanism at high energy, in Ref. (1).

14. P.D.B. Collins et al, phys. lette. 47 B (1973) 171.

15. P.D.B. Collins et al, The pomeron in elastic Meson-Baryon Scattering Phys. Dept., University of Durham (1974).

16. V. Barger & R.J.N. Phillips, Nucl. Phys. B 32 (1971) 93.

17. A. Martin Nucl. Phys. B77 (1974) 226.

18. W.R. Frazer, D.R. Snider, Chung-I Tan. Phys. Rev. D8 (1973) 3180.

19. D. Amati et al Nucl. Phys. B62 (1973) 173.

20. H. Cheng and T.T. Wu, Phys. Rev. Lette. 24 (1970) 1456.

21. J.L. Cardy, Nucl. Phys. (1971) 455.

22. N. Sakai & J.N.J. White, Nucl. Phys. B59 (1973) 511.

23. H.I. Miettinen, s-channel phenomenolgy of diffraction scattering, in Ref (12).

24. H.I. Miettinen, Impact structure of diffraction scattering, Ref. TH. 1864-CERN (1974).

25. E.H. de Groot & H.I. Miettinen, shadow approach to diffraction scattering, RL-73-003, Rutherford laboratory.

26. T. Inami, R.J.N. Phillips & R.G. Roberts, Two Component analysis of the inelastic overlap function, RL-74-112, Rutherford Laboratory.

27. R.J.N. Phillips, high energy elastic scattering, RL-74-113, Rutherford Laboratory.

28. R. Henzi & P. Valin, phys. lette. 48B (1974) 119.

29. F.S. Henyey et al, Nucl. phys. B70 (1974) 445.

30. Edelstein et al, phys. Rev. D5 (1972) 1073.

31. P. Heckman and Henzi, phys. lette. 41B (1972) 189.

32. D. Roy & R.G. Roberts, Nucl. phys. B77 (1974) 240.

33. H.I. Miettinen, Geometrical distribution of hadronic collision, Ref. TH. 1906-CERN.

34. V. Barger et al, Nucl. phys. B88 (1975) 237.

35. A.J. Buras, J. Dias de Devs, Nucl. phys. B71 (1974) 481.

36. J. Dias de Deus, Nucl. phys. B59 (1973) 231.

37. Uni Maon, Comments on the systemics of pomeron exchange reactions, "proceedings of the tenth Rencontre de Moriond" France, March 1975 (Phenomenology of hadronic structure).

38. P. Kroll, Geometrical scaling in proton-proton scattering (in Ref (37)).

39. A. Martin, Does the pomeron obey geometrical scaling (in Ref (37)).

40. V. Barger & R.J.N. Phillips, Geometrical aspects of the high energy elastic scattering. Wisconsin preprint (1975).

41. A. Martin, Testing Geometrical Scaling, Phys. Dept., Univ. of Durham.

42. Z. Koba, H.B. Nielsen, and P. Olesen, Nucl. Phys. B40 (1972) 317.

43. G. Auberson, T. Kinoshita and A. Martin, phys. Rev. D3 (1971) 317.

44. P. Kroll, Nucl. Phys. B82 (1974) S10, W. Grein, R. Guigas, and P. Kroll to be published in nucl. phys. B.

45. J. Dias de Deus, Nuovo Cimento Lette. 7 (1973) 476.

46. E.L. Berger, Multiplicities production processes at high energy Ref. TH. 1737-CERN (1973).

47. Chung-I Tan, Nucleon-Antinucleon production as the cause of rising Proton-proton total cross section at ISR, presented at the IX Recontre de Moriond, March 3-9 (1974).

48. Mahiko Suzuki, "Decomposition of intercept of Regge trajectory according to multiplicities of produced particles. Comparison with proton-proton collision data at CERN". Department of physics, University of California, Berkeley, California 94720.

49. F.S. Henyey, Elastic Scattering from the two component picture. Ann Arbor, Mich., U.S.

50. A. Capella & Min-Shihchen, increasing cross section, diffractive excitation and the triple pomeron coupling. phys. Review D8 (1973) 2097.

51. L. Caneschi & M. Ciafaloni, Models for rising cross-sections. In Ref. 12.

52. D.P. Roy, phenomenology of diffraction, in Ref. 1.

53. I.G. Halliday, strong interaction dynamics, in Ref. 1.

54. M. Bishari and J. Koplik, A perturbative description of the pomeron suggested by the two-component model of multi particle production. phys. lette. 44B (1973) 175.

55. R. Blankenbecler, Threshold effects of diffractive production phys. Rev. lette. 31 (1973) 964.

56. T.K. Gaisser & Chung-I Tan, phys. Rev. D8 3881 (1973).

57. Chung-I Tan & Don M. Tow, phys. Rev. D9 2176 (1974).

58. M. Antinucci et al., Nuovo Cimento Lett. 6 (1973) 121.

TABLE CAPTIONS

Table (1) Parameters of the fits shown in Figs. (20,21 22 and 24)

Table (2) Parameters of the fits shown in Fig. 23.

FIGURE CAPTIONS

Fig. 1 Total cross-sections of a) $\pi^{\pm}p$, b) $K^{\pm}p$ c) $p^{\pm}p$ (Ref.1).

Fig. 2 Energy dependence of the deference of total cross-sections for particle and anti-particle (Ref. 1).

Fig. 3 Comparison of diffraction scattering at various energies for $\pi^{\pm}p$, $K^{\pm}p$, $p^{\pm}p$.

(Ref. 1).

Fig. 4 Exponential slopes of diffraction scattering for $\pi^{\pm}p$, $K^{\pm}p$ and $p^{\mp}p$. The data have been fitted over the interval $0.07 \leqslant |t| \leqslant 0.3\ \mathrm{Gev}^2$

(Ref. 1)

Fig. 5 Differential cross-sections for elastic scattering at 100 Gev/c.

(Ref. 3)

Fig. 6 Logarithmic slopes at $|t| = 0.2\ \mathrm{Gev}^2$ as a function of S. (Ref. 3)

Fig. 7 The apparatus used at the CERN-ISR by the CERN-Rome Collaboration to measure pp elastic scattering at very small angles (Ref. 4)

Fig. 8 The differential elastic cross-sections at E_{cm} = 23.6 and 30.8 Gev in the Coulomb-Nuclear interference region (Ref. 4)

Fig. 9 The ratio of the real to imaginary part of the forward scattering amplitude for pp elastic scattering versus Lab-momentum. The dotted line is a result of dispertion calculation, while the continuous line represents the result of the calculation in which it was assumed that $\sigma_t \sim (\ln s)^2$. (Ref. 6)

Fig. 10 Total proton-proton cross-sections measured at the ISR by the CERN-Roma collaboration, and by the Pisa Stony Brook Collaboration (Ref. 6)

Fig. 11	(a) The large angle PP elastic scattering at various laboratory momenta. (b) Features of $\frac{d\sigma}{dt}$ (PP) in ISR range.
Fig. 12	Results of a dispersion relation calculation of the ratio ρ of the real to the imaginary part of the nuclear amplitude. The various curves refer to various hypothesis on the high energy behaviour of the total proton-proton cross-section (Ref. 6)
Fig. 13	Total, inelastic and elastic proton-proton cross-sections versus the Lab.momentum. (Ref. 12)
Fig. 14	Compilation, interpolation and extrapolation of existing data on elastic proton-proton scattering at the maximum and minimum ISR energies. (Ref. 12)
Fig. 15	Partial wave amplitude as a function of the proton-proton impact parameter at the minimum and maximum ISR energies (Ref. 12)
Fig. 16	Proton-proton opaqueness at the two extreme ISR energies. In the lower part of the figure the opaqueness increment in the ISR energy range is plotted versus the impact parameter.
Fig. 17	Data on proton-proton elastic scattering from ISR together with some lower energy points.
Fig. 18	The effective trajectory for pp scattering obtained from the ISR data. (Ref. 10).
Fig. 19	The effective trajectory for pp scattering for $S < 50\ GeV^2$ (Ref. 10)
Fig. 20	Fit (i) "Chapter III. Sec. 2" using eqs. (9, 10, 11), to the ISR data, and lower energy data for $\lvert t \rvert < 1\ GeV^2$. (Ref. 10)
Fig. 21	Fit (ii) "Chapter III. Sec. 2" using eqs. (9, 10, 11, 13). (Ref. 10)
Fig. 22	Fit (iii) "Chapter III. Sec. 2" using eqs. (9, 11, 14). (Ref. 10)
Fig. 23a, b)	Fit the (PP) data to Regge cut model (Chapter III Section 3.2). using eqs. (9, 10, 27). The figures also show the fits of πP, $K p$ data using eqs. (9, 10). (Ref. 15).
Fig. (23 c)	The effective trajectory for pp scattering at ISR with $\alpha_{P}(t) = 1.07 + 0.22\ t$ and $\alpha_c(t) = 1.14 + 0.11\ t$ (Ref. 15).

Fig. 24	Fit the pp data to Regge cut model "Chapter III, Section 3.3" using eqs. (28, 17, 14) (Ref. 10).
Fig. 25	The imaginary parts of the impact parameter amplitudes corresponding to fit (i) (Chapter III) to the ISR data (Ref. 10).
Fig. 26	Solution of the s-channel unitarity relation "Chapter 4. eq. 5". (Ref. 25)
Fig. 27	Ratios of pp cross-sections and elastic slope. The Van Hove limits correspond to a Gaussian overlap function of maximum strength allowed by unitarity. (Ref. 13).
Fig. 28	Inelastic overlap function at P_{Lab} = 1500 Gev/c. The solid points are calculated from the ISR data. The solid curve is the Two-component parameterization, "Chapter IV. eq. 15" (Ref. 25).
Fig. 29	(A) Results of fits "eq.17, Chapter IV" to data, a, b, c, and d represent the parameters P, P_1, B, and B_1 respectively. (B) The upper solid curve represents $G = G_{Gau} + G_{edg}$, ---- represents G_{Gau}, ..., represents fit with $G = G_{Gau}$ for $o \leqslant -t \leqslant 0.6$ $(Gev/c)^2$, the lower solid curve represents $5 \times G_{edg}$ (Ref. 28)
Fig. 30	(A) Impact structure of proton-proton scattering at $\sqrt{S} = 53$ Gev. (B) The amplitude, inelastic overlap function and eikonal extracted from experimental data at $\sqrt{s} = 53$ (Ref. 24)
Fig. 31	(A) Inelastic overlap functions calculated from the $\sqrt{s}$ = 21, 31, 44 and 53 Gev ISR data. (B) Difference of the $\sqrt{s}$ = 53 and 31 Gev inelastic overlap function. (Ref. 24)
Fig. 32	The decomposition of the imaginary part of the elastic amplitude into its various components. "eq. (19). Chapter IV". (Ref. 22).
Fig. 33	Inelastic overlap function H_{in} (s, b) and its two components at two energies s = 940, 2840 Gev^2 in impact parameter space. (Ref. 26).
Fig. 34	Difference of the inelastic overlap function at two energies s = 28406 s = 940. The experimental curve is that obtained from the analysis of Miettinen & Pirilla. (Ref. 26).

Fig. 35 (A) plot of $d\sigma/dt$ at the lowest and highest ISR energies (Ref. 12)

(B) plot of $\Phi(\tau,s) \equiv \frac{1}{\sigma_{in}^2}\frac{d\sigma_{el}}{dt}$ as a function of τ for the lowest and highest ISR energies. The points everywhere fall into a unique curve. (Ref. 35).

Fig. 36 Compilation of PP cross-sections and slope parameter (for $|t| \leqslant 0.15$). (Ref. 13).

Fig. 37 Evaluation of geometrical scaling predictions for σ_{el}/σ_t and B/σ_t (Ref. 34).

Fig. 38 Evaluation of geometrical scaling predictions for secondary maximum and dip location "eqs. 24, 25, Chapter V" (Ref. 34).

Fig. 39 Effective Regge trajectory as deduced from: (a) the geometrical scaling prediction of the right hand side of eq. (26) "Chapter V".

$$\alpha_{eff}(s,t) - 1 = \left(1 + \frac{1}{2}Bt\right)\frac{d\ln R^2}{d\ln s}$$

(values denoted by shaded region)

(b) $$\alpha_{eff}(s,t) = \frac{\partial}{\partial\ln s}\left(\ln\frac{d\sigma}{dt}\right)$$

(values represented by data points). (Ref. 34).

Fig. 40 Comparison of the geometrical scaling predictions with α_{eff} obtained from the ISR data "eq. 33 Chapter V" (Ref. 41).

Fig. 41 The structure of the real part in t and b space. (Ref. 38).

Fig. 42 Im $\tilde{F}$ and G_{in} at b = 0 as a function of Lab. momentum (solid lines). The dashed line represents a result for Im $\tilde{F}$ belonging to the same G_{in} but without taking into account the real part. (Ref. 38)

Fig. 43 The momentum dependence of the total, elastic and inelastic proton-proton cross-sections. The dashed lines are the results for σ_t and of calculation without the real part. (Ref. 38).

Fig. 44 $\sigma_t B/\sigma_{in}$ compared with the energy dependence of σ_{in} (solid line). The dashed-dotted line represents the energy dependence of the slope itself (Ref. 38).

Fig. 45	The shaded region in this figure corresponds to the increase in σ_D which we go from energy s_1 to s_2 (Ref. 46)
Fig. 46	$\langle n \rangle$ σ $(N\bar{N})$ from (Ref. 47)
Fig. 47	(a) MP production of a single $N\bar{N}$ pair. (b) MP production of a two $N\bar{N}$ pairs (Ref. 47).
Fig. 48	Non diffractive total cross-section without $N\bar{N}$ pairs. (Ref. 47).
Fig. 49	Illustration of how central channels opening up may generate a peripheral ΔG_{in} (s, b). (a) The inelastic cross-section stays constant but $d\sigma/dt$ shrinks. G_{in} (s, b) decreases at b = o and increases at b $>$ 1 fm. (b) The new central channels compensates the above central decrease. As a result, the cross-section increase appears peripheral. (c) The difference of the two overlap functions of b. (Ref. 24).
Fig. 50	Inelastic overlap function at b = 0 vx. S. The curve is an illustration of our explnation for the constancy of G_{in} (s, b = o) over the ISR energy range, calculated using $\alpha_P(t) = 1.06 + 0.35\ t$. (Ref. 24).

Table 1 parameters of the fits shown in Figs. 20, 21, 22, and 24

Fits	(i)	(ii)	(iii)	(iv)
$\alpha_P(0)$	1.058	1.043	1.082	1.065
α_P'	0.254	0.203	0.220	0
G_P	27.03	30.71	22.42	31.10
a_P	2.25	2.76	1.72	2.24
x	0.55	0.42	0.72	0.57
a_1	3.07	5.06	3.52	2.66
y		− 1.21		0.252
a_2		− 0.76		7.96
$\alpha_{P_1}(0)$		1.0		
α_{P_1}'		0.47		
$\alpha_c(0)$	1.0	1.0	0.824	
G_c	0.162	0.243	2.230	
a_c	0.449	0.864	1.168	
$\alpha_R(0)$	0.433	0.440	0.543	0.391
α_R'	0.900	0.870	0.531	0.374
G_R	320.2	247.6	189.0	372.4
a_R	2.91	1.12	4.73	3.80
β	0.158	0.18	0.21	0.14
a_3	0.334	1.47	− 1.11	0.110
t_0	0.19	0.21	0.19	0.17
β_1			0.022	0.018
a_4			− 5.70	− 4.33
λ				0.80
χ^2/pt		1.8	2.2	2.1

The χ^2/pt is given for 1001 data points fitted. All parameters are in GeV units except G_p, G_c, G_R which are in mb.

Table 2

Parameters of the fits shown in Figs. 23, a, b

	$\alpha_P(0)$	α_P'	G_P	a_P	x	a_1	$\alpha_R(0)$	α_R'	G_R	a_R	β	a_3	t_0	λ	b_1	b_2	χ^2/pt
pp (1)	1.07	0.22	24.85	2.05	0.65	3.39	0.50	0.90	103.0	4.16	0.40	-2.16	0.19	0.072	-1.16	-	1.9
pp (2)	"	"	24.94	1.73	0.73	3.38	"	"	"	"	"	"	"	0.069	-	-1.70	1.9
πp	"	"	14.80	1.00	0.65	3.20	"	"	49.2	1.50	0.13	16.3	0.13				1.6
Kp	"	"	12.75	1.00	0.66	2.80	"	"	26.4	-0.54	0.62	3.6	0.11				1.2

The G's are in mb, all other quantities are in GeV units. The two pp fits are indistinguishable at small $|t|$, but have different cut contributions, as described in the text.

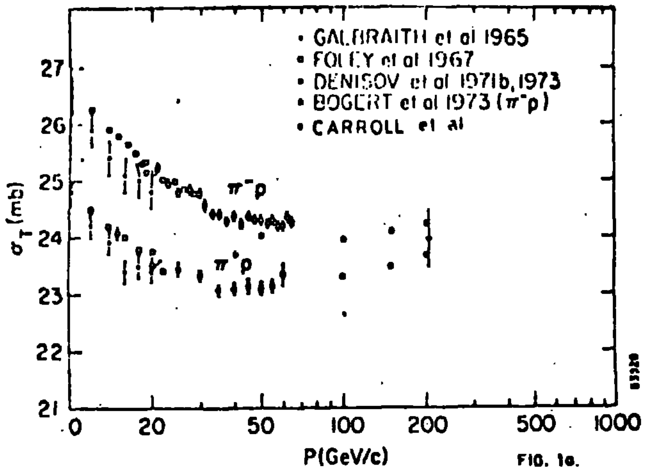

FIG. 1a.

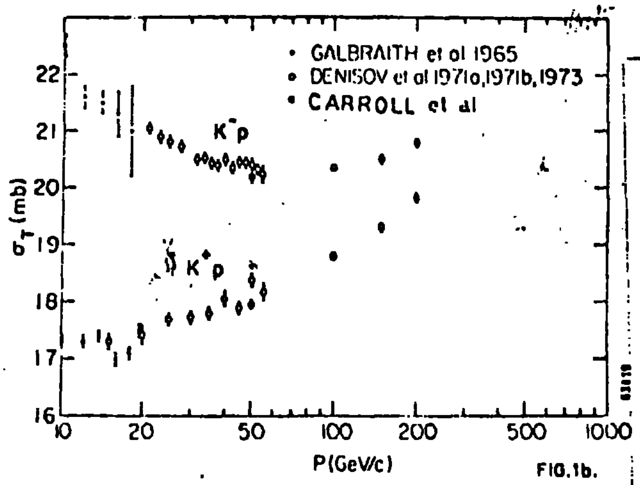

FIG.1b.

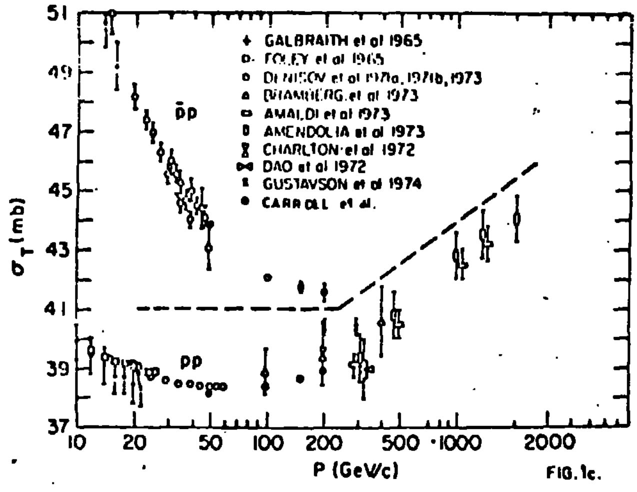

FIG.1c.

Fig.1

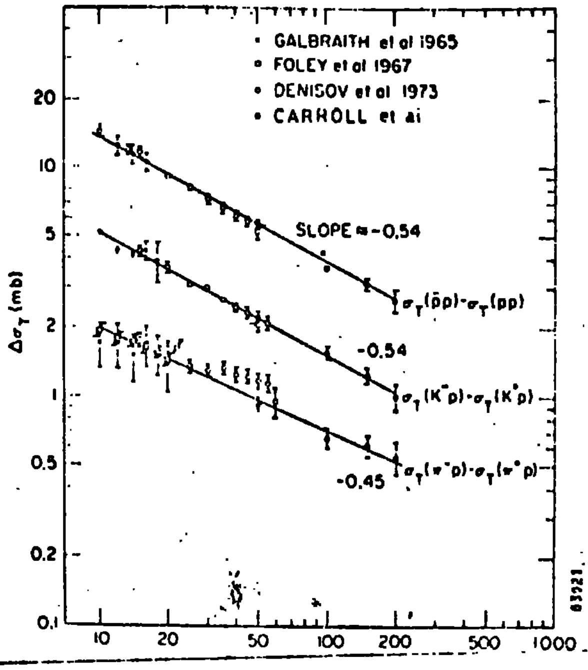
GALBRAITH et al 1965
FOLEY et al 1967
DENISOV et al 1973
CARROLL et al
20
10
5
2
1
0.5
0.2
0.1
$\Delta\sigma_T$ (mb)
10
20
50
100
200
500
1000
SLOPE ≈ -0.54
$\sigma_T(\bar{p}p)-\sigma_T(pp)$
-0.54
$\sigma_T(K^-p)-\sigma_T(K^+p)$
-0.45
$\sigma_T(\pi^-p)-\sigma_T(\pi^+p)$
83921

Fig. 2

Fig. (3)

Comparison of diffraction scattering at various energies for $\pi^{\pm}p$, $K^{\pm}p$ and $p^{\pm}p$.

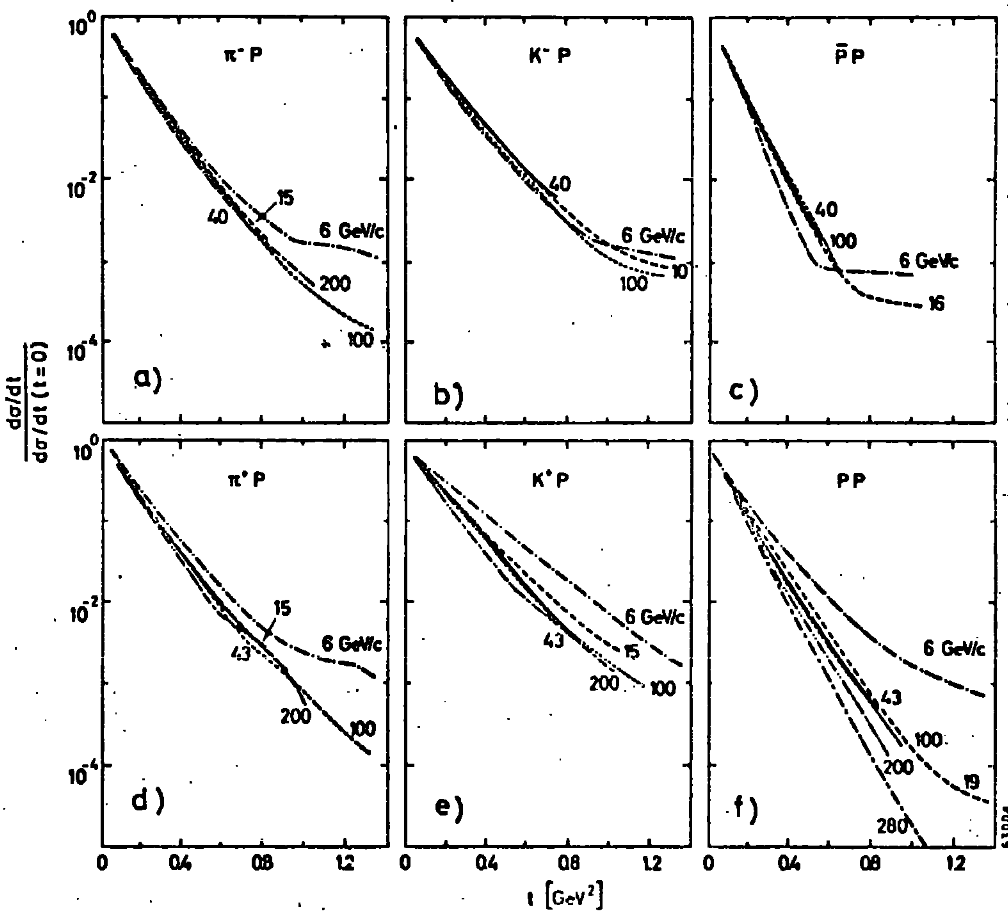

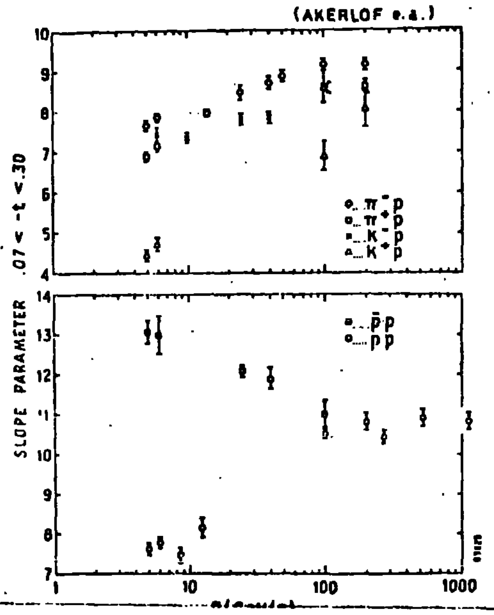
(AKERLOF e.a.)
SLOPE PARAMETER .07 < -t < .30
10
9
8
7
6
5
4
14
13
12
11
10
9
8
7
1
10
100
1000
o.. π⁻ p
o... π⁺ p
▪... K⁻ p
▵... K⁺ p
▪... p̄ p
o.... p p

Fig. 4

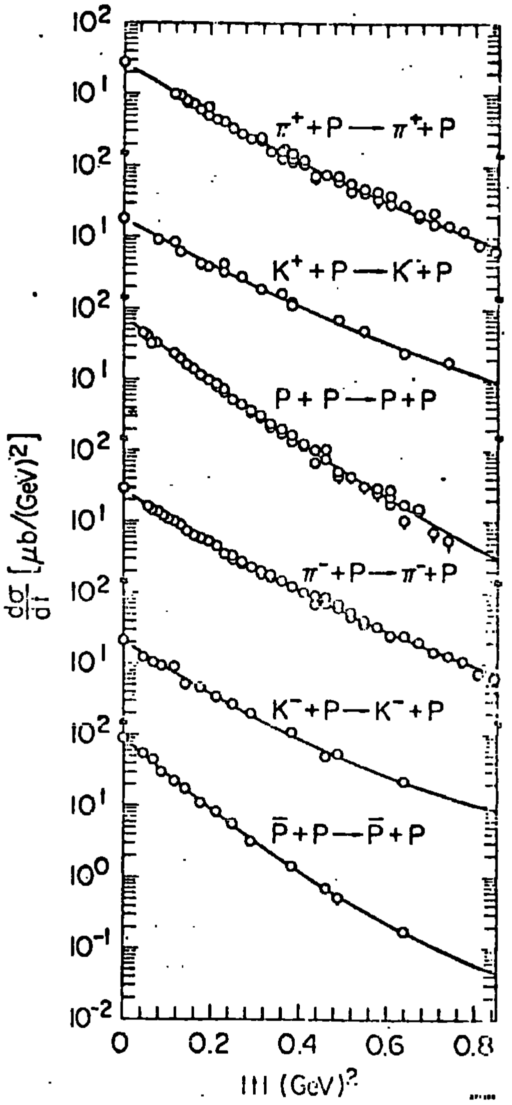
10^2
10^1
10^0
10^{-1}
10^{-2}
$\frac{d\sigma}{dt}$ [μb/(GeV)^2]
$\pi^+ + P \to \pi^+ + P$
$K^+ + P \to K^+ + P$
$P + P \to P + P$
$\pi^- + P \to \pi^- + P$
$K^- + P \to K^- + P$
$\bar{P} + P \to \bar{P} + P$
0
0.2
0.4
0.6
0.8
|t| (GeV)^2

Figure 5

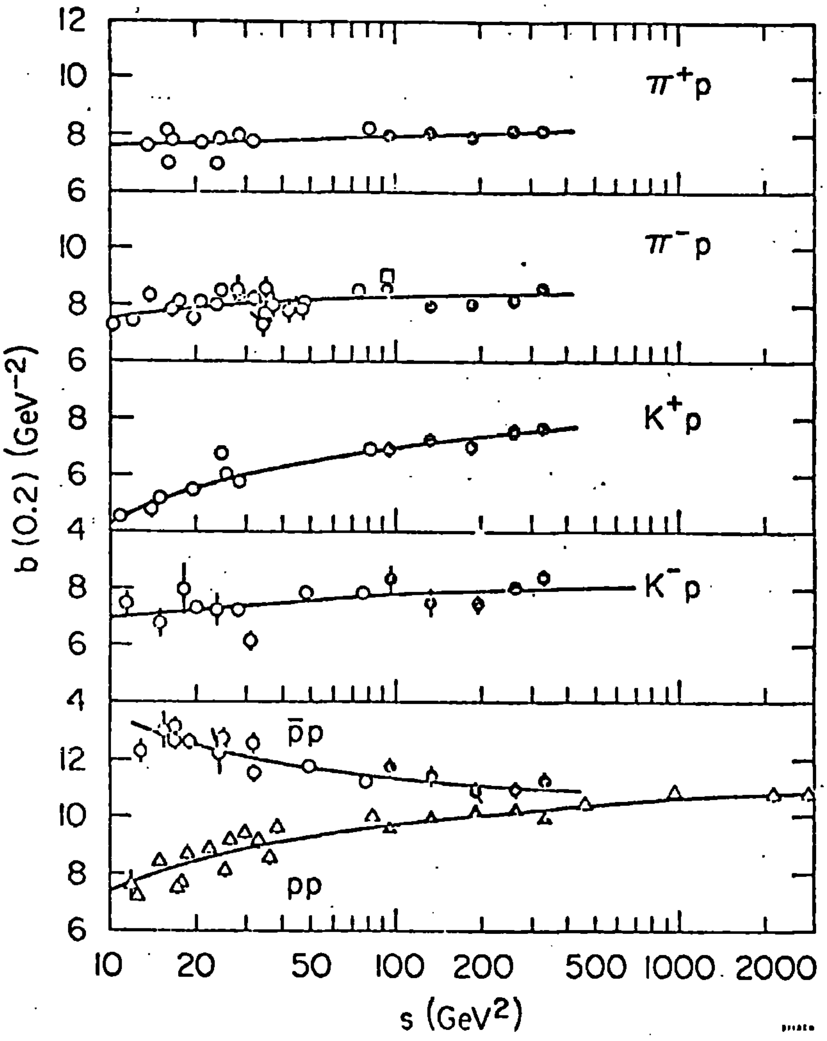
b (0.2) (GeV^{-2})
s (GeV^2)
π^+p
π^-p
K^+p
K^-p
$\bar{p}p$
pp
12
10
8
6
4
10
20
50
100
200
500
1000
2000

Figure 6

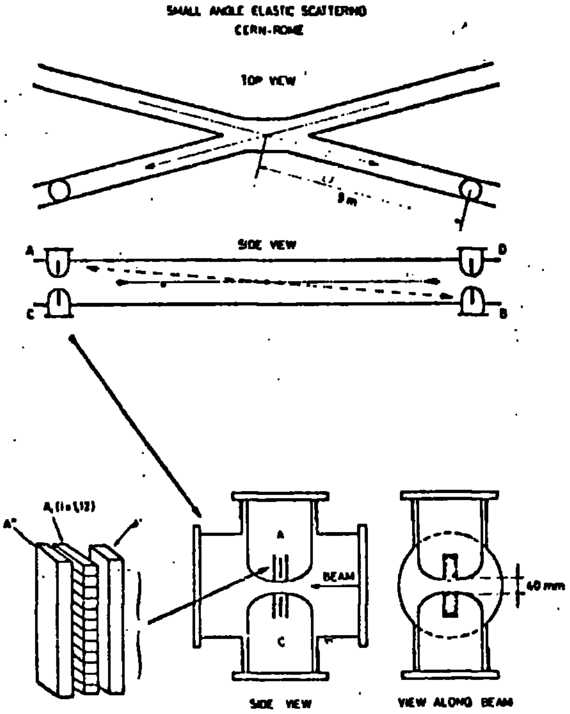
SMALL ANGLE ELASTIC SCATTERING
CERN-ROME
TOP VIEW
9 m
SIDE VIEW
A
D
C
B
A°
A_i (i=1,12)
A'
A
BEAM
C
40 mm
SIDE VIEW
VIEW ALONG BEAM

Fig.7. General layout of experimental apparatus and sketch of disposition of hodoscopes in their special vacuum chamber sections.

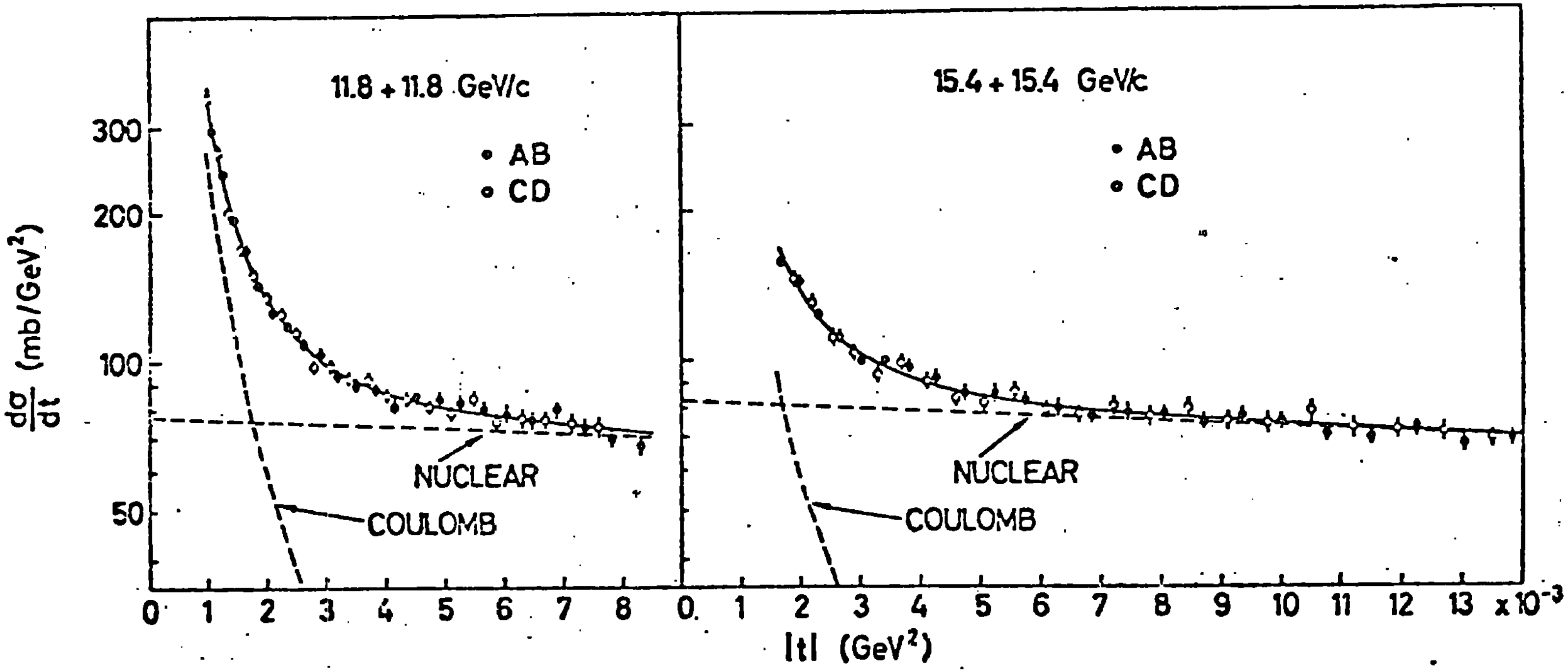
11.8 + 11.8 GeV/c
• AB
○ CD
15.4 + 15.4 GeV/c
• AB
○ CD
NUCLEAR
COULOMB
NUCLEAR
COULOMB
$\frac{d\sigma}{dt}$ (mb/GeV^2)
300
200
100
50
0
1
2
3
4
5
6
7
8
0
1
2
3
4
5
6
7
8
9
10
11
12
13
x 10^{-3}
|t| (GeV^2)

Fig. 8

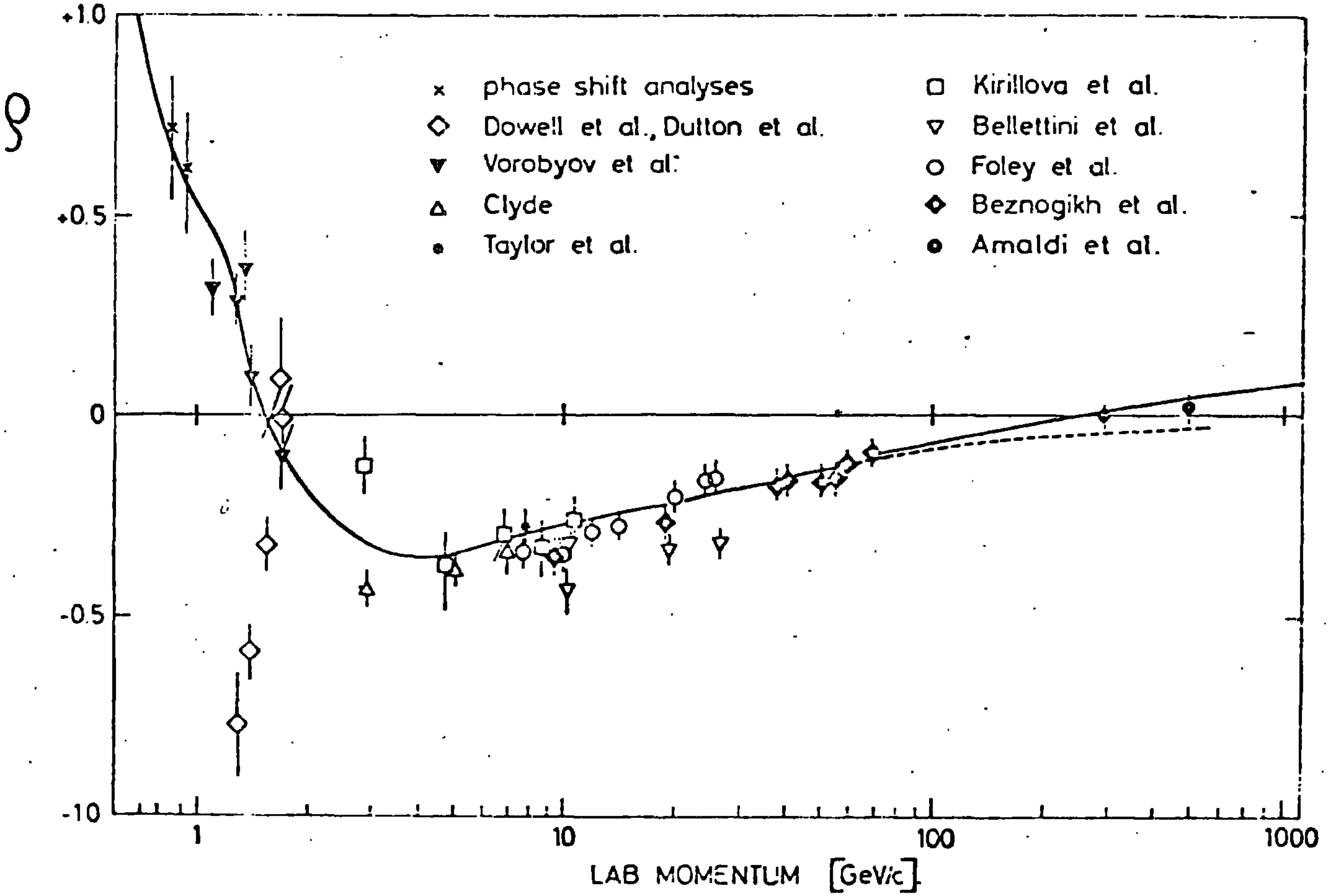
ρ
+1.0
+0.5
0
-0.5
-10
1
10
100
1000
LAB MOMENTUM [GeV/c]
× phase shift analyses
◇ Dowell et al., Dutton et al.
▼ Vorobyov et al.
△ Clyde
• Taylor et al.
□ Kirillova et al.
▽ Bellettini et al.
○ Foley et al.
◆ Beznogikh et al.
⊙ Amaldi et al.

Fig. 9

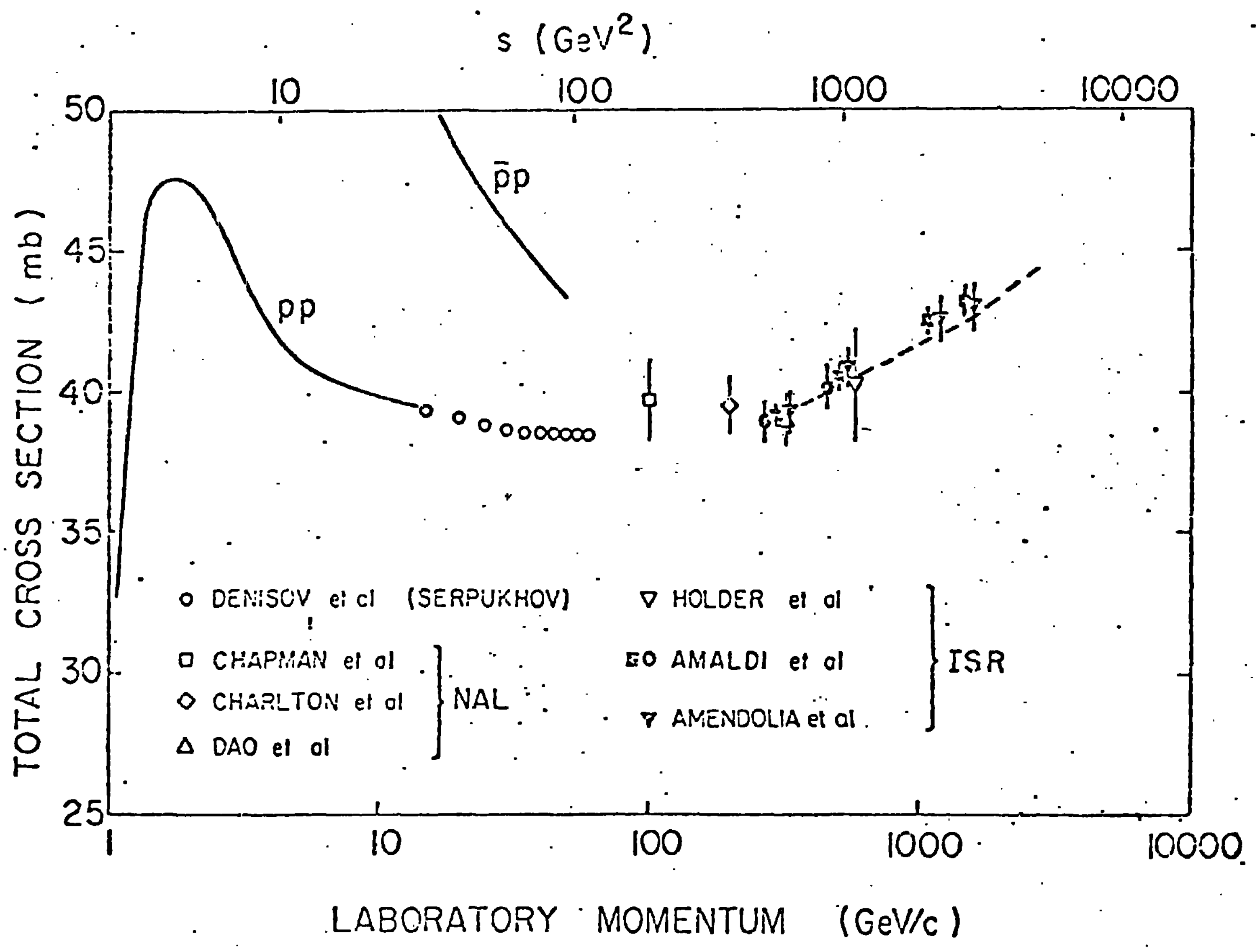
s (GeV^2)
10
100
1000
10000
TOTAL CROSS SECTION (mb)
50
45
40
35
30
25
pp
$\bar{p}p$
○ DENISOV et al (SERPUKHOV)
□ CHAPMAN et al
◇ CHARLTON et al
△ DAO et al
NAL
▽ HOLDER et al
□○ AMALDI et al
▼ AMENDOLIA et al
ISR
1
10
100
1000
10000
LABORATORY MOMENTUM (GeV/c)

Fig. 10

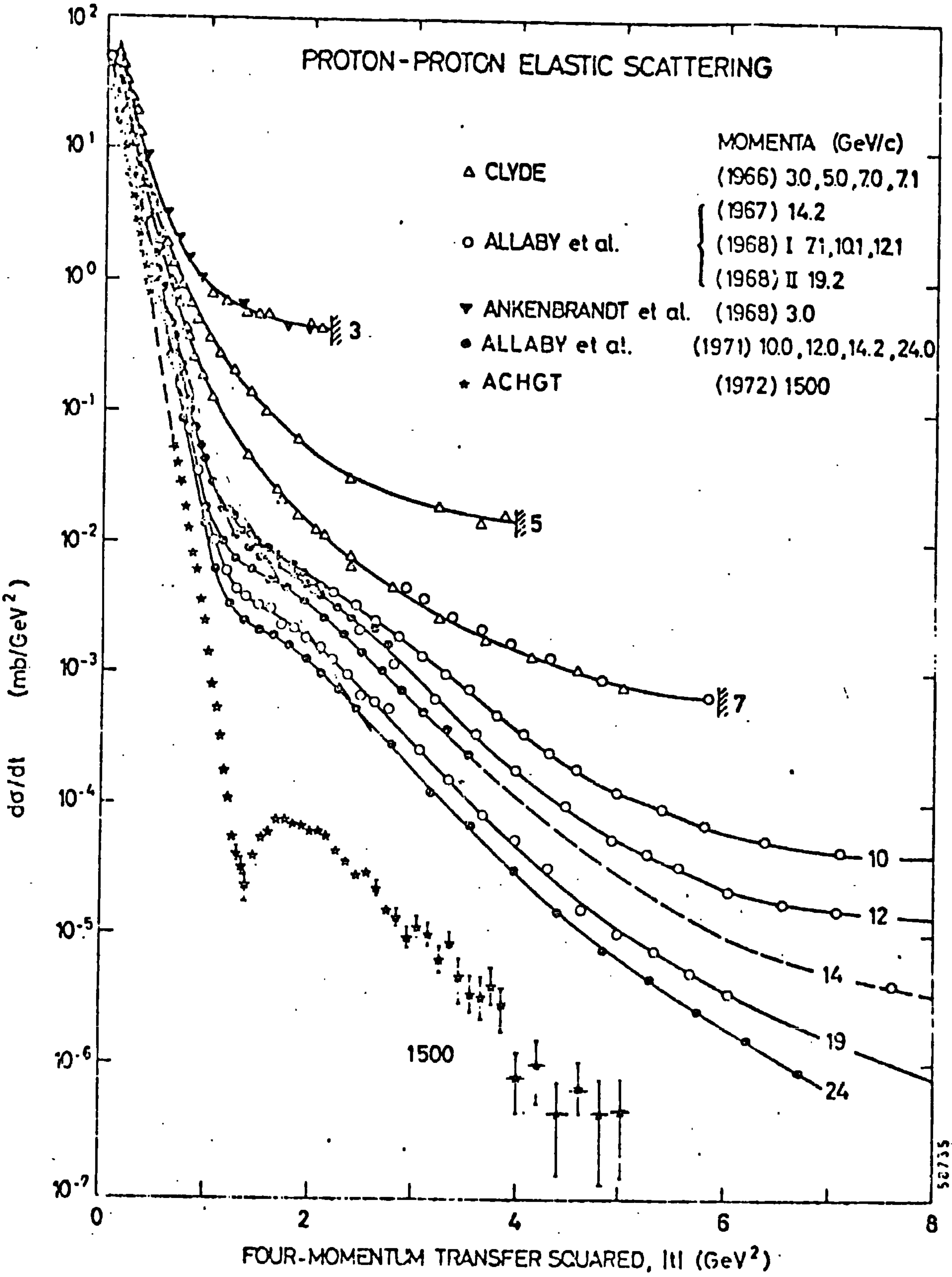

Fig. 12(a) The large angle pp elastic scattering at various laboratory momenta.

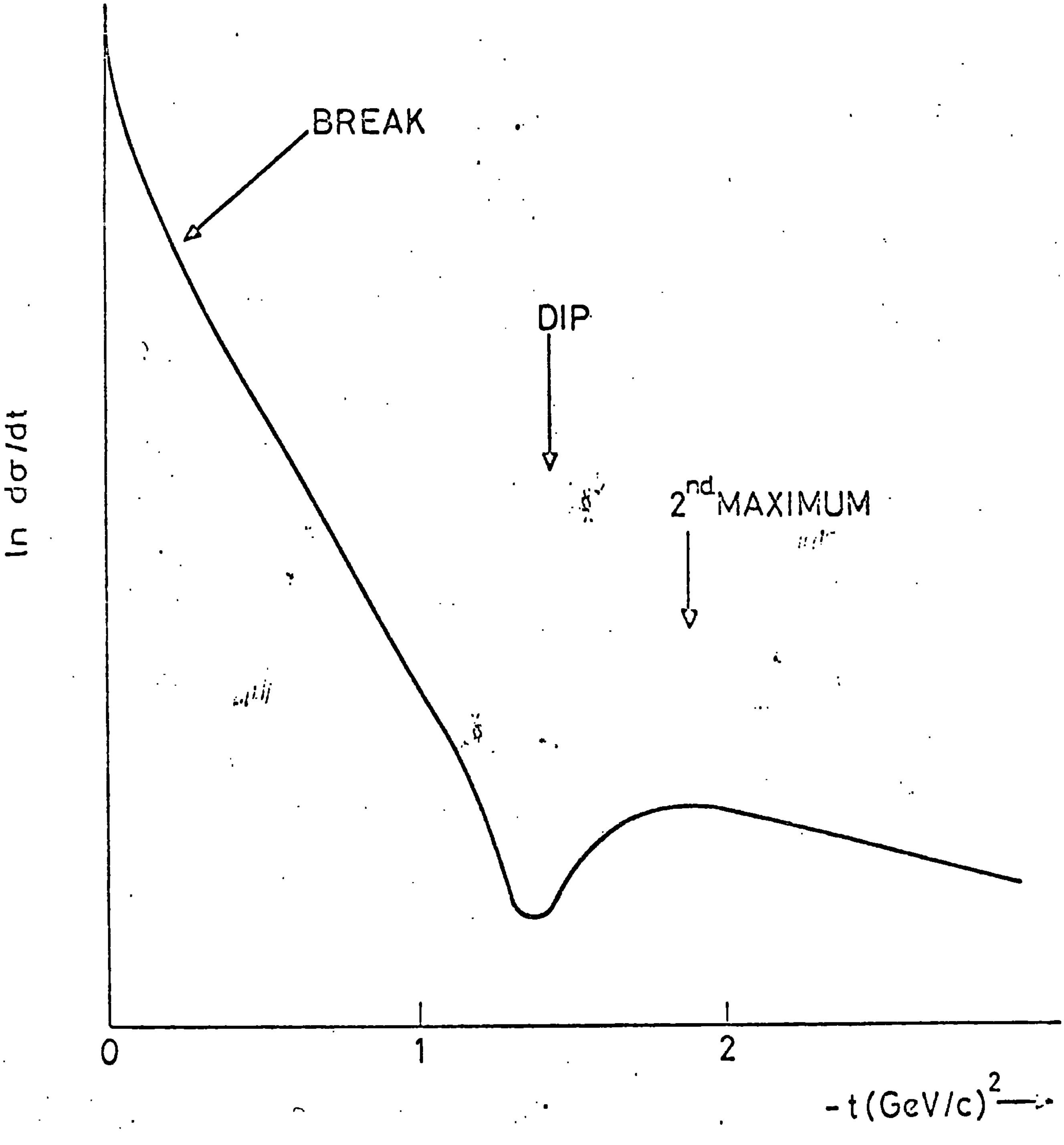

FIG. II(b). FEATURES OF $\frac{d\sigma}{dt}(pp \rightarrow pp)$ AT ISR

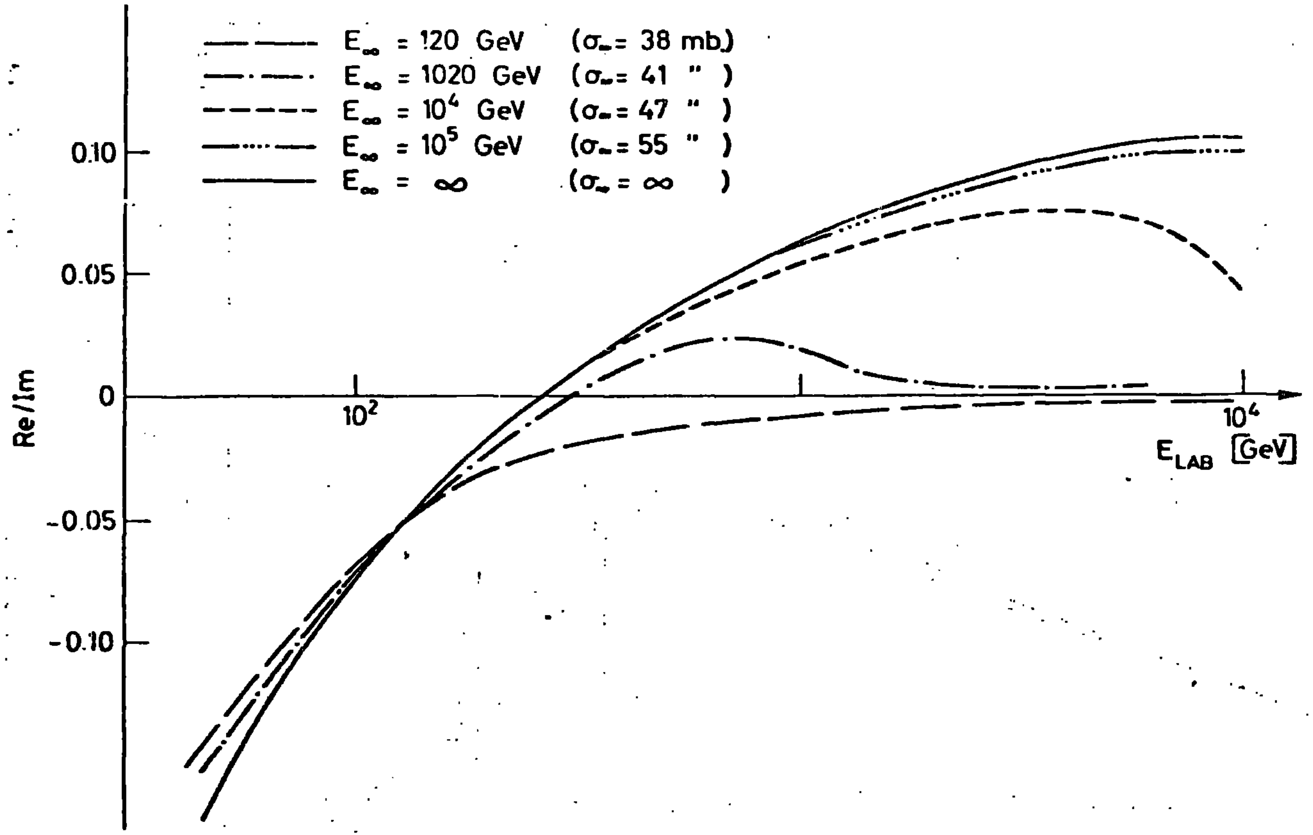
E_∞ = 120 GeV (σ_∞ = 38 mb)
E_∞ = 1020 GeV (σ_∞ = 41 ")
E_∞ = 10^4 GeV (σ_∞ = 47 ")
E_∞ = 10^5 GeV (σ_∞ = 55 ")
E_∞ = ∞ (σ_∞ = ∞)
Re/Im
0.10
0.05
0
-0.05
-0.10
10^2
10^4
E_{LAB} [GeV]

Fig. 12

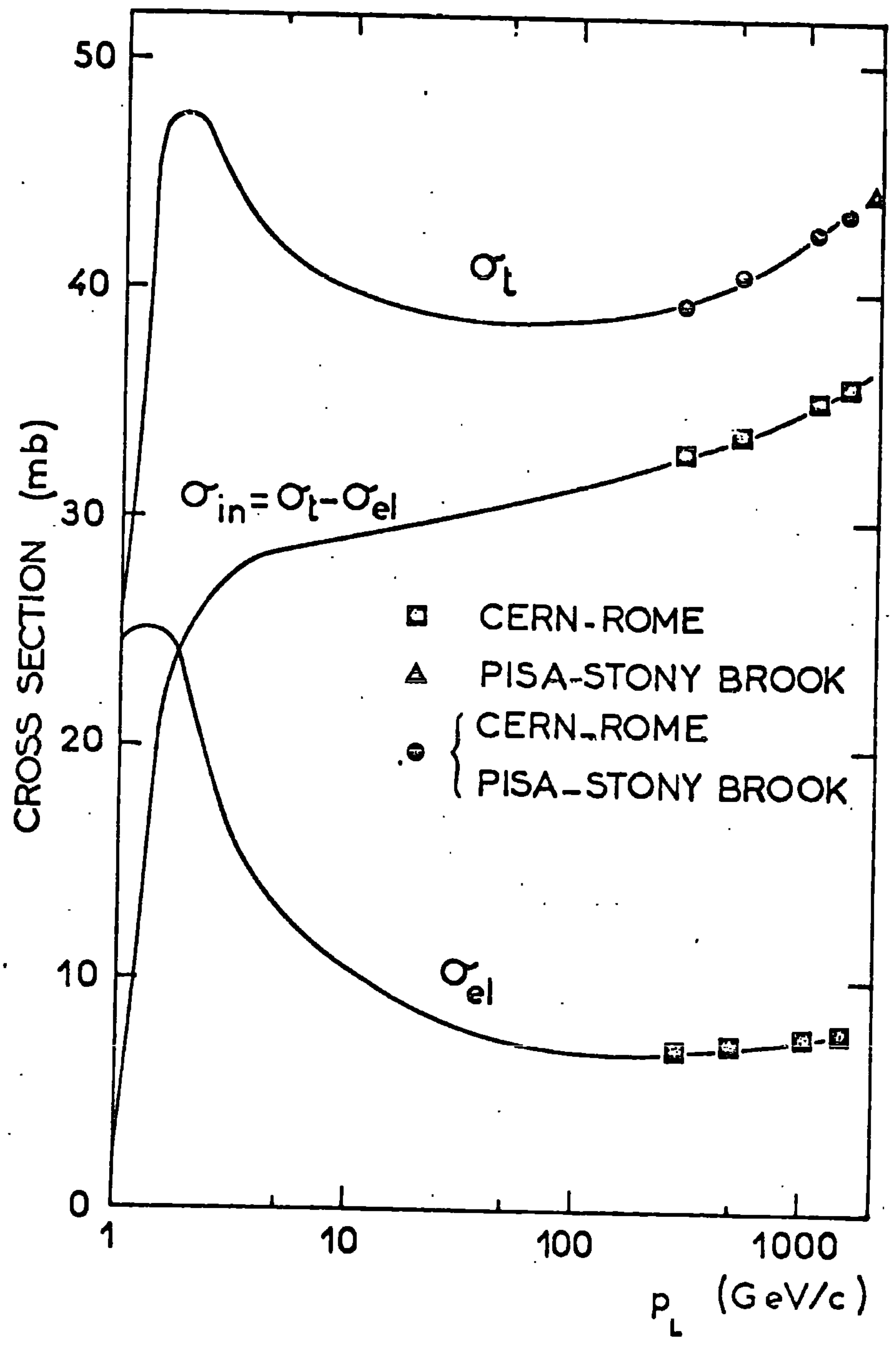

Fig. 13 Total, inelastic and elastic proton-proton cross-sections versus the laboratory momentum (Ref. 10).

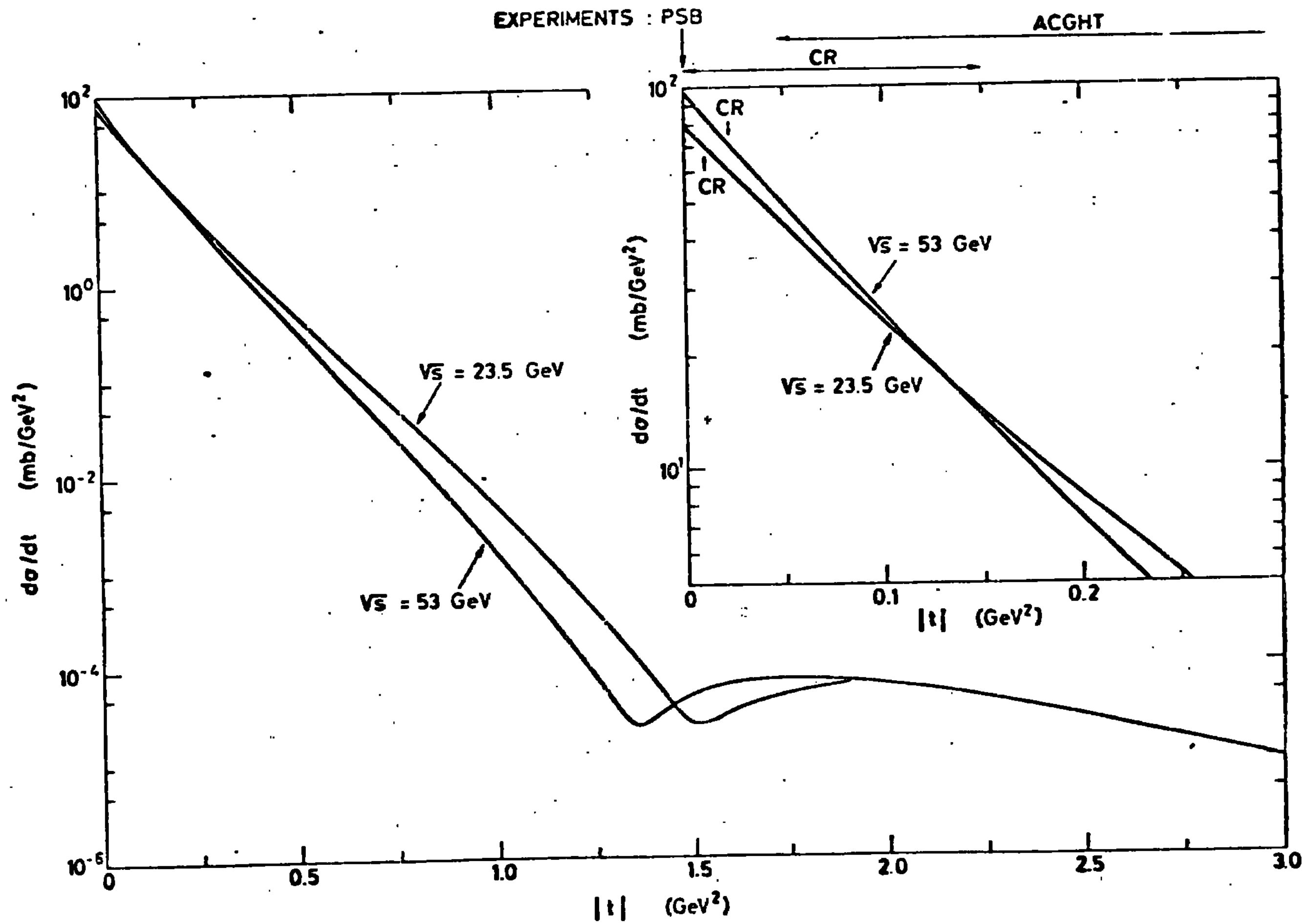
EXPERIMENTS : PSB
CR
ACGHT
10^2
10^0
10^{-2}
10^{-4}
10^{-6}
dσ/dt (mb/GeV²)
$\sqrt{s}$ = 23.5 GeV
$\sqrt{s}$ = 53 GeV
0
0.5
1.0
1.5
2.0
2.5
3.0
|t| (GeV²)
10^2
10^1
CR
CR
$\sqrt{s}$ = 53 GeV
$\sqrt{s}$ = 23.5 GeV
dσ/dt (mb/GeV²)
0
0.1
0.2
|t| (GeV²)

Fig. 14

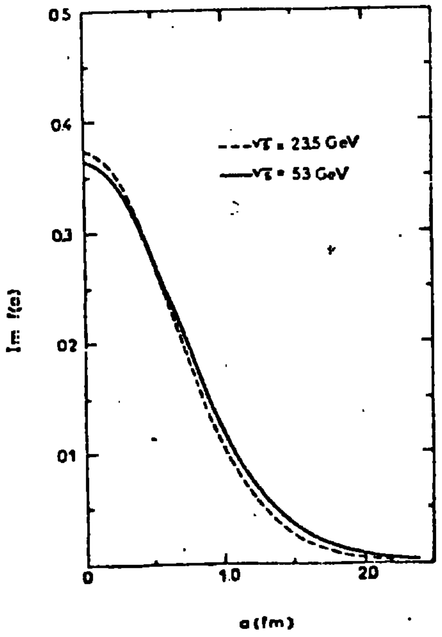
0.5
0.4
0.3
0.2
0.1
Im f(a)
---$\sqrt{s}$ = 23.5 GeV
—$\sqrt{s}$ = 53 GeV
0
1.0
2.0
a (fm)

Fig. 15

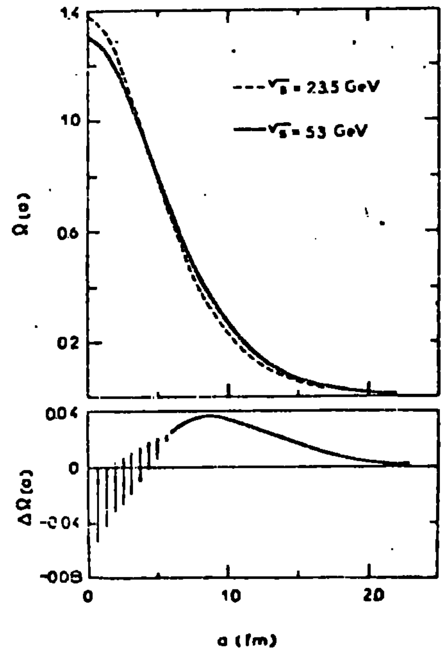
1.4
1.0
0.6
0.2
Ω(a)
---$\sqrt{s}$ = 23.5 GeV
—$\sqrt{s}$ = 53 GeV
0.04
0
-0.04
-0.08
ΔΩ(a)
0
10
20
a (fm)

Fig. 16

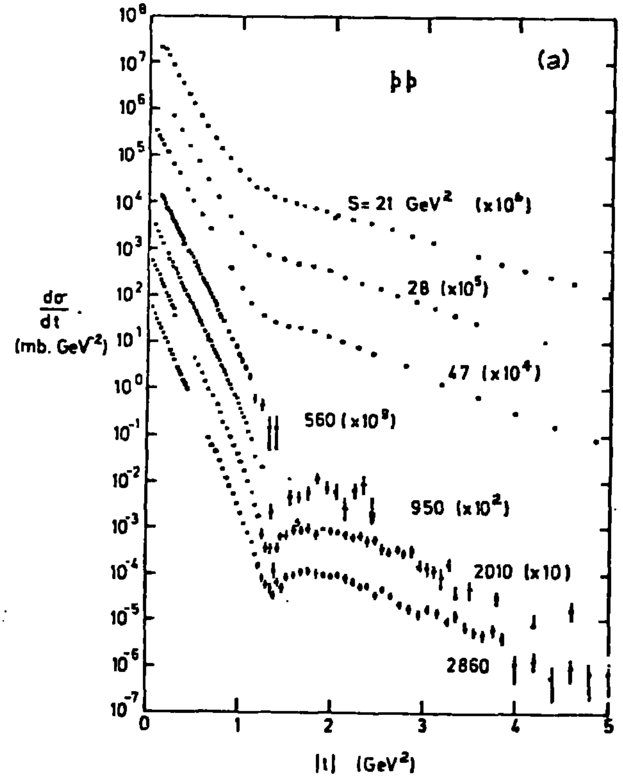
10^8
10^7
10^6
10^5
10^4
10^3
10^2
10^1
10^0
10^{-1}
10^{-2}
10^{-3}
10^{-4}
10^{-5}
10^{-6}
10^{-7}
$\frac{d\sigma}{dt}$ (mb. GeV^{-2})
(a)
$\bar{p}p$
S= 21 GeV^2 (x10^6)
28 (x10^5)
47 (x10^4)
560 (x10^3)
950 (x10^2)
2010 (x10)
2860
0
1
2
3
4
5
|t| (GeV^2)

Fig. 17

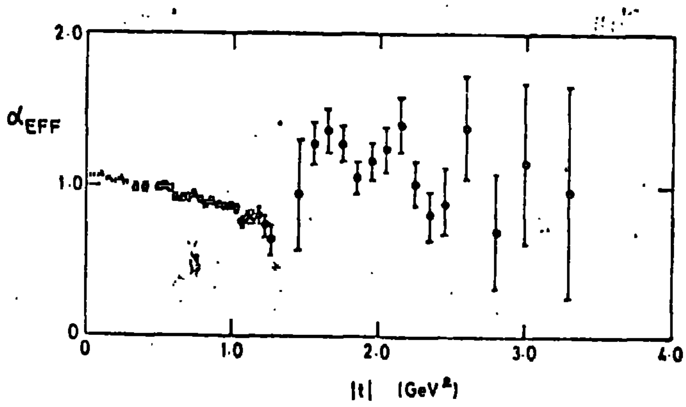

Fig.18. The effective trajectory for pp scattering obtained from the ISR data of fig. 17.

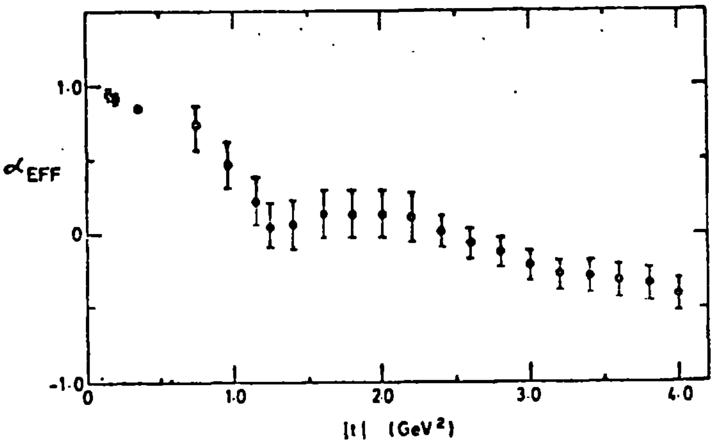

Fig.19. The effective trajectory for pp scattering for $s < 50$ GeV^2.

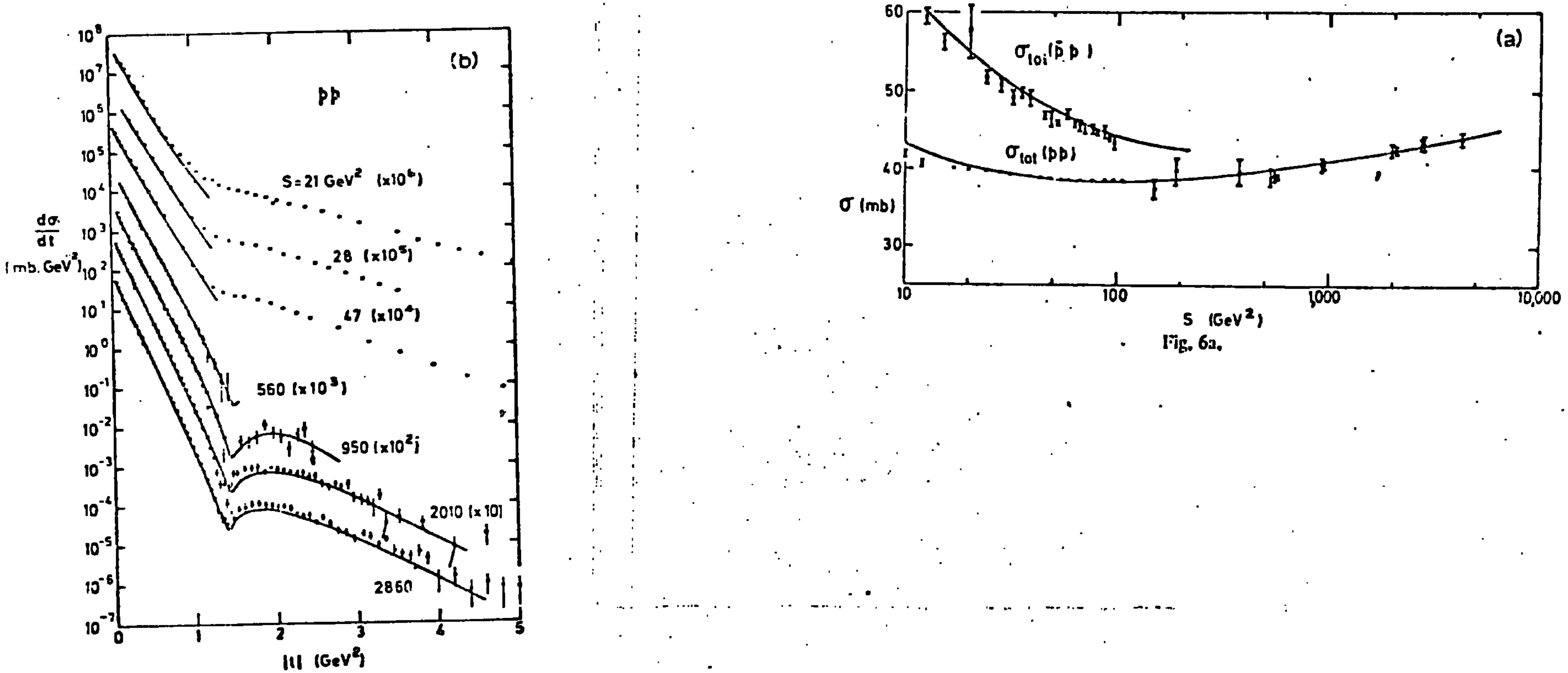
(b)
p̄p
$\frac{d\sigma}{dt}$ (mb. GeV^{-2})
10^8
10^7
10^5
10^5
10^4
10^3
10^2
10^1
10^0
10^{-1}
10^{-2}
10^{-3}
10^{-4}
10^{-5}
10^{-6}
10^{-7}
0
1
2
3
4
5
|t| (GeV^2)
S=21 GeV^2 (x10^6)
28 (x10^5)
47 (x10^4)
560 (x10^3)
950 (x10^2)
2010 (x 10)
2860
(a)
$\sigma_{tot}(\bar{p}p)$
$\sigma_{tot}(pp)$
σ (mb)
60
50
40
30
10
100
1,000
10,000
S (GeV^2)

Fig. 6a.

Fig. 20

21

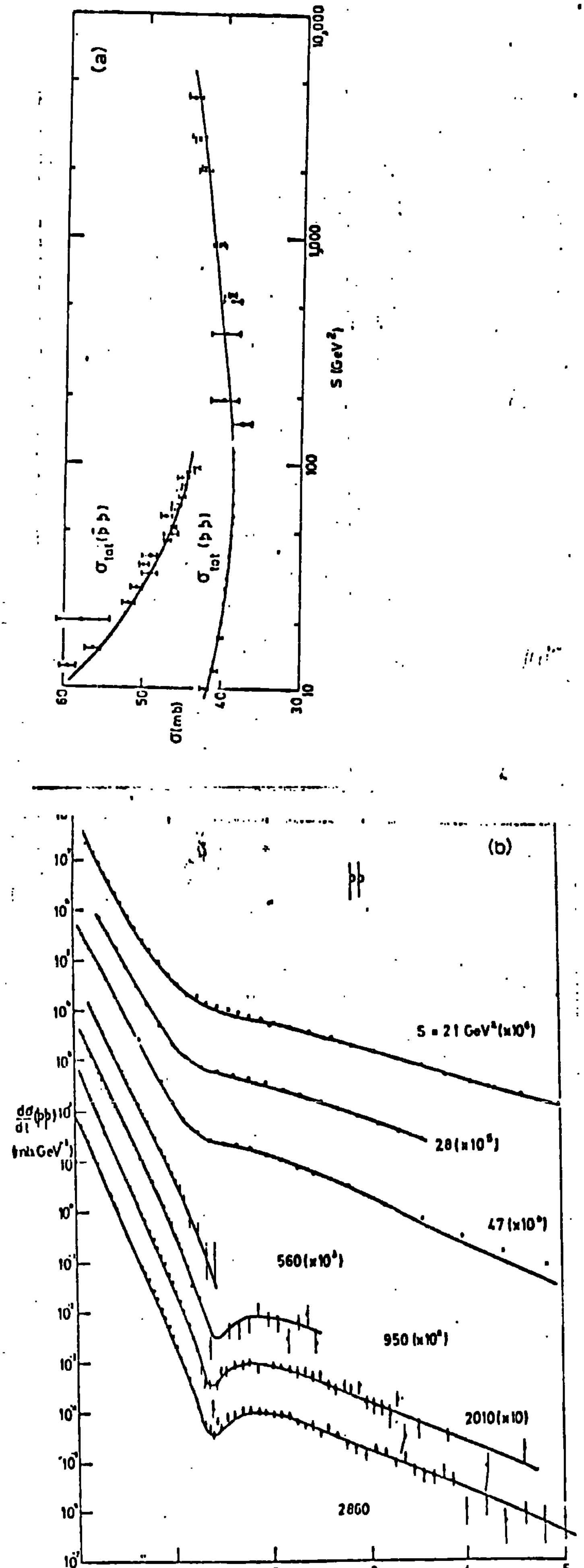

Fig. 7b.

Fig.21

DURHAM UNIVERSITY
SCIENCE
15 APR 1976
SECTION
LIBRARY

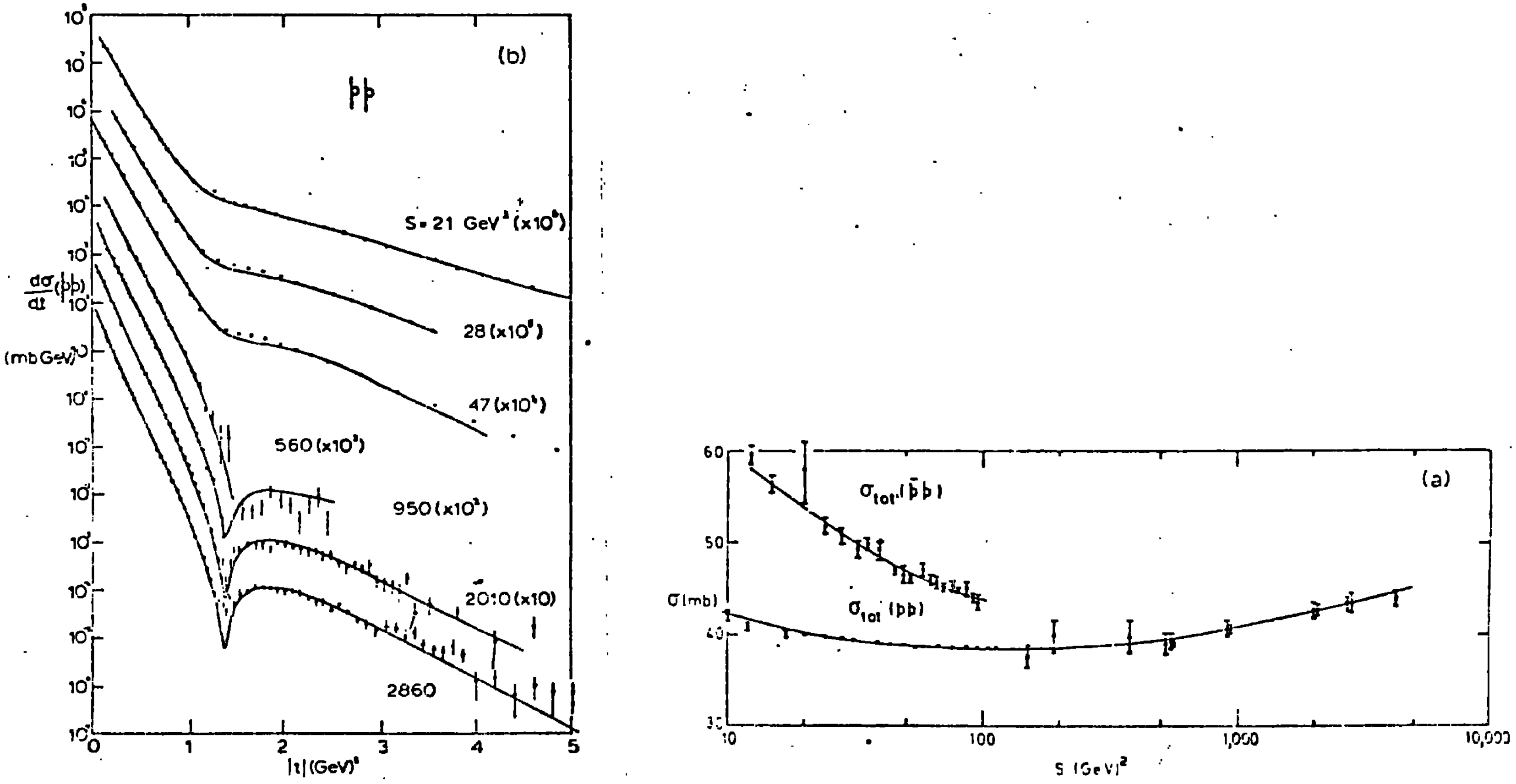
(b)
pp
S = 21 GeV² (x10⁸)
28 (x10⁶)
47 (x10⁴)
560 (x10³)
950 (x10²)
2010 (x10)
2860
dσ/dt (pp)
(mb GeV⁻²)
|t| (GeV)²
0
1
2
3
4
5
(a)
σ_tot (p̄p)
σ_tot (pp)
σ (mb)
60
50
40
30
10
100
1,000
10,000
S (GeV)²

Fig.22

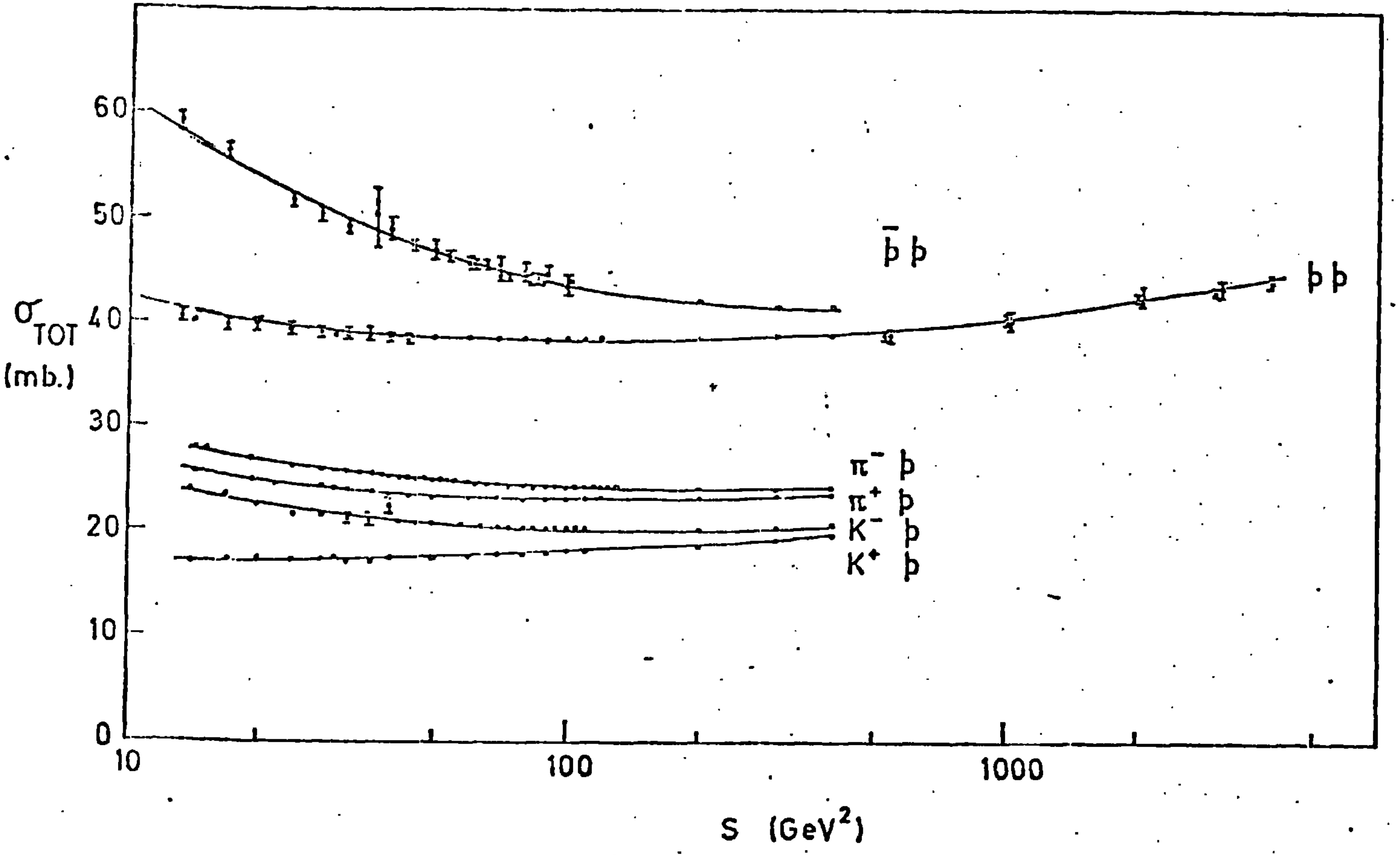
σ_{TOT}
(mb.)
60
50
40
30
20
10
0
10
100
1000
S (GeV^2)
$\bar{p}p$
pp
$\pi^- p$
$\pi^+ p$
$K^- p$
$K^+ p$

FIG. 23. a.

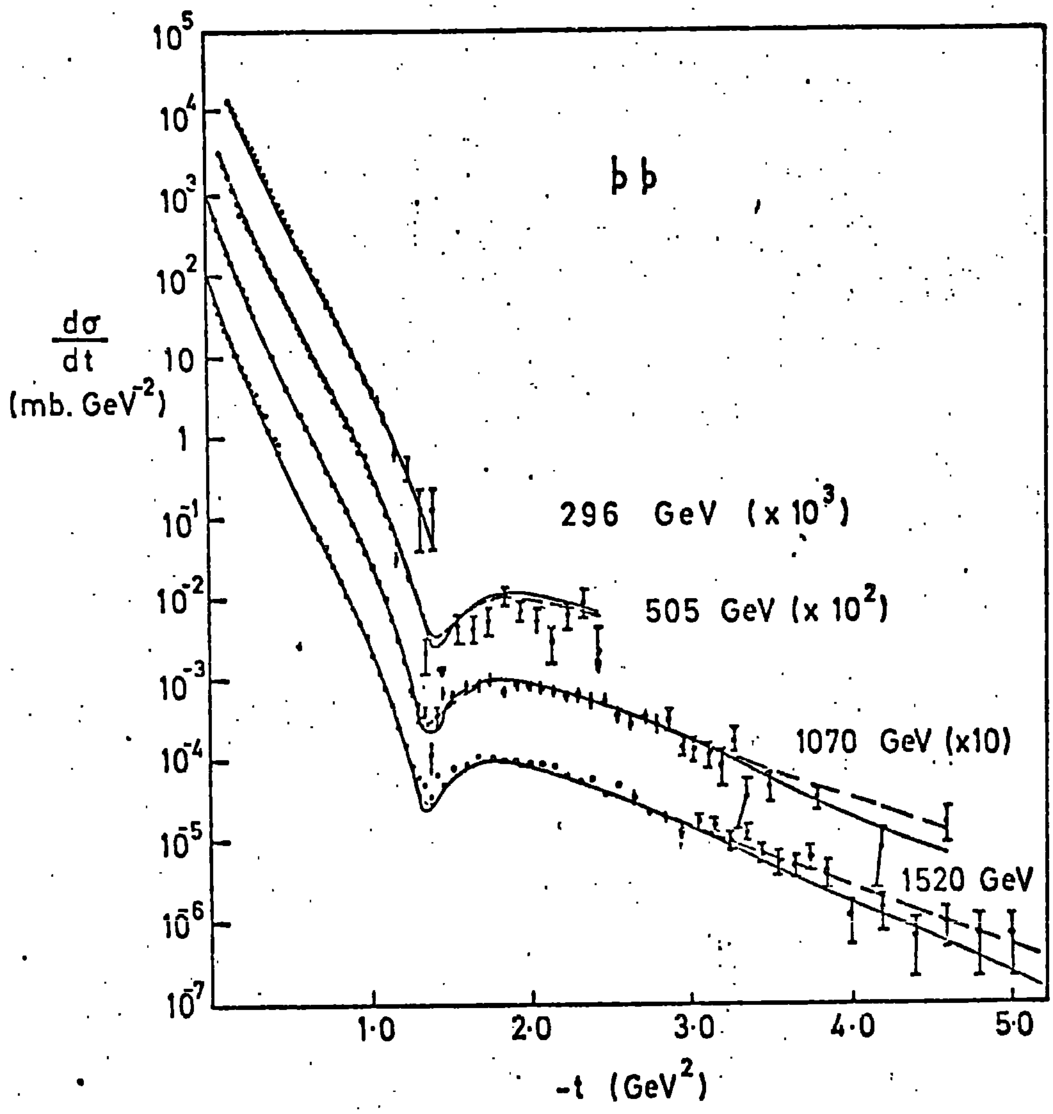

p̄ p
$\frac{d\sigma}{dt}$ (mb. GeV^{-2})
10^5
10^4
10^3
10^2
10
1
10^{-1}
10^{-2}
10^{-3}
10^{-4}
10^{-5}
10^{-6}
10^{-7}
296 GeV (x 10^3)
505 GeV (x 10^2)
1070 GeV (x10)
1520 GeV
1·0
2·0
3·0
4·0
5·0
-t (GeV^2)

FIG. 23.b.

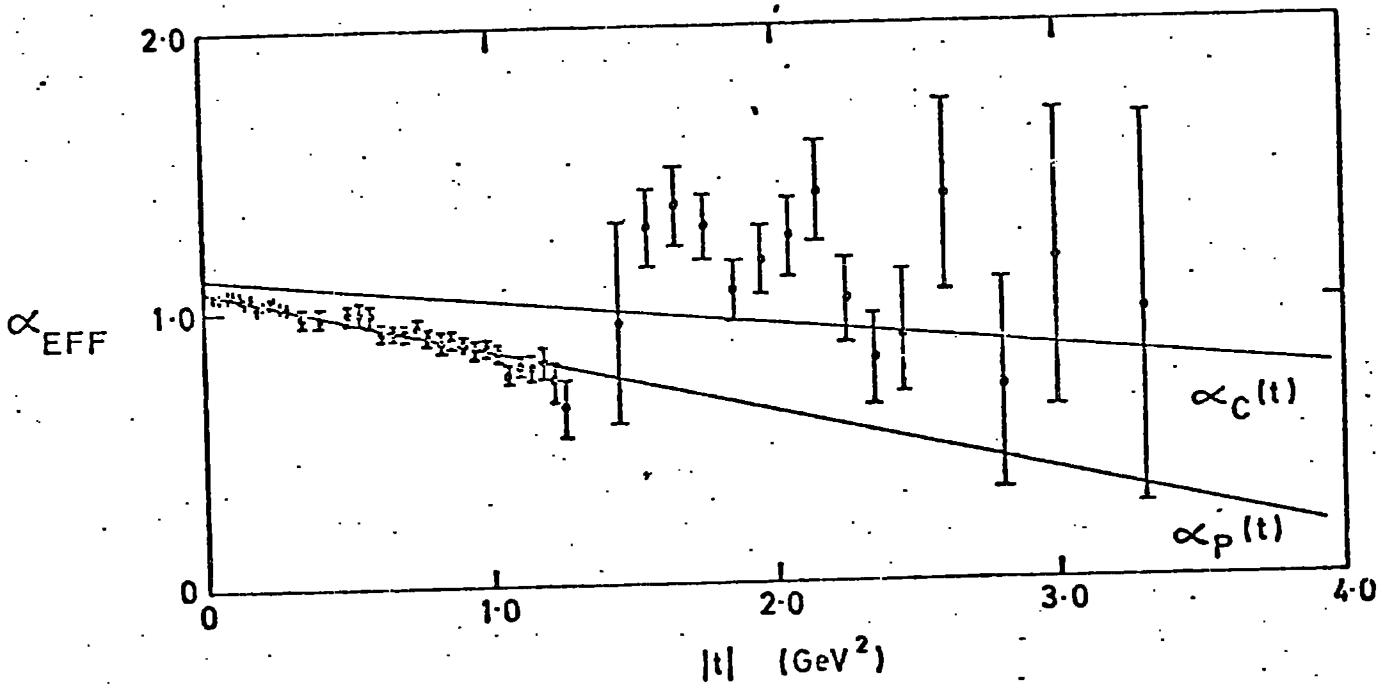

FIG. 23. C.

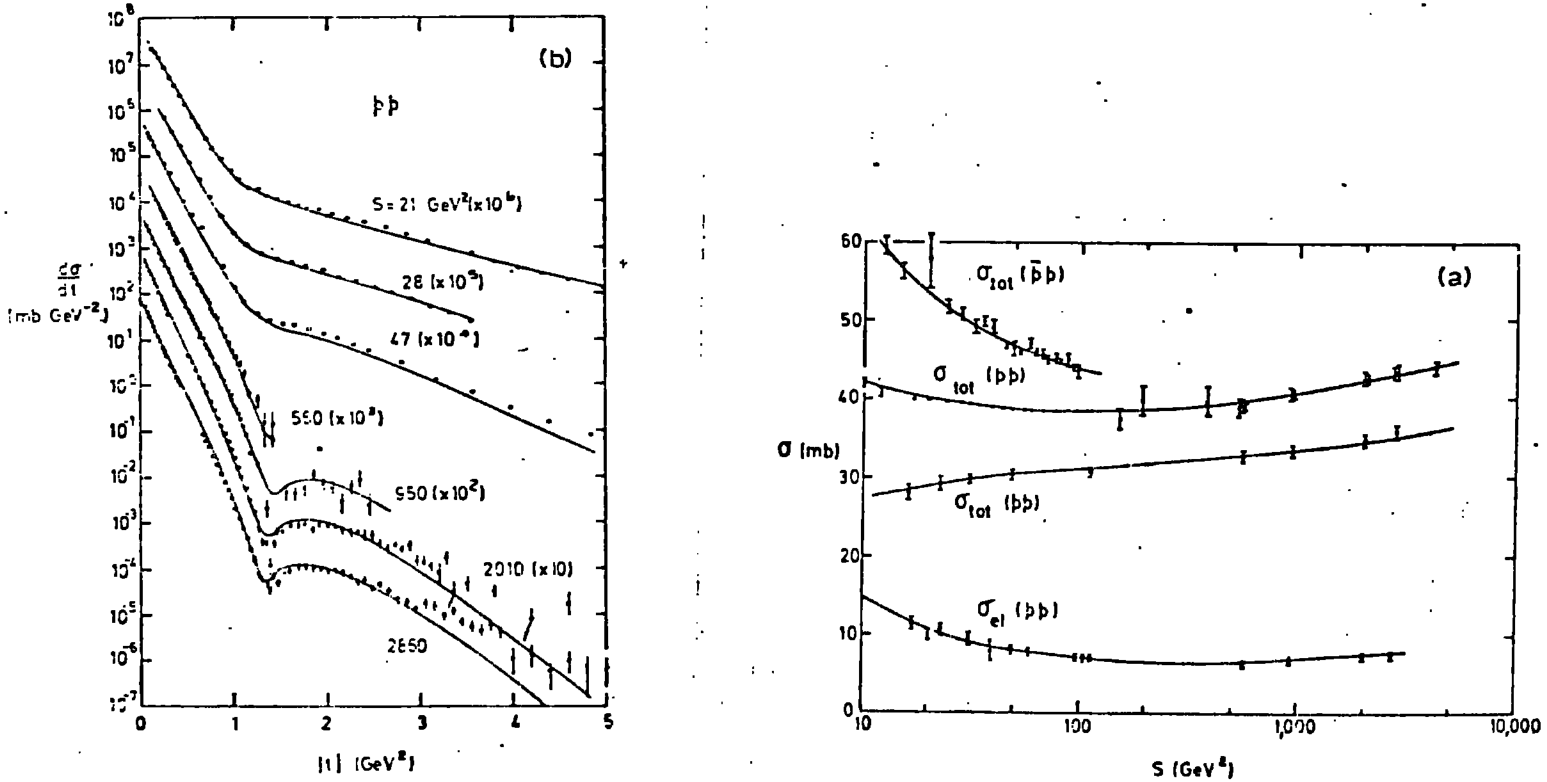
(b)
pp
$\frac{d\sigma}{dt}$ (mb GeV^{-2})
S = 21 GeV^2 (x 10^6)
28 (x 10^5)
47 (x 10^4)
550 (x 10^3)
550 (x 10^2)
2010 (x 10)
2850
|t| (GeV^2)
(a)
σ_{tot} ($\bar{p}p$)
σ_{tot} (pp)
σ_{tot} (pp)
σ_{el} (pp)
σ (mb)
S (GeV^2)
10
100
1,000
10,000

Fig. 21

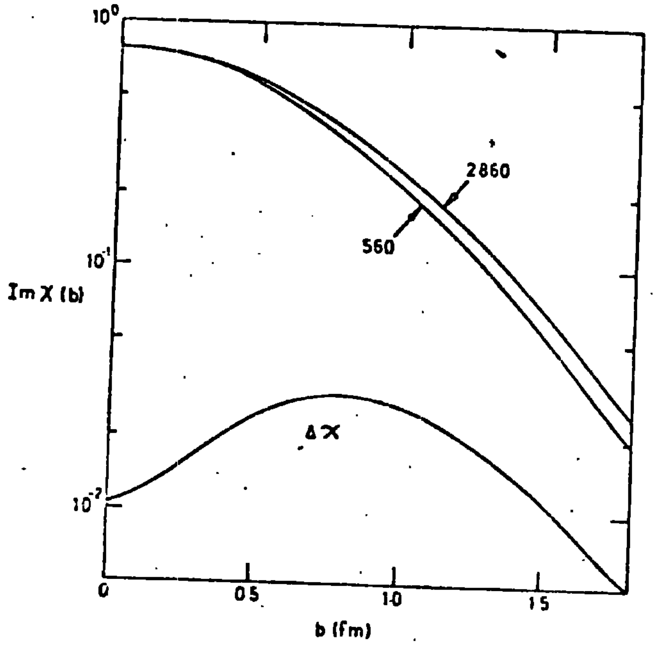

Fig. 25

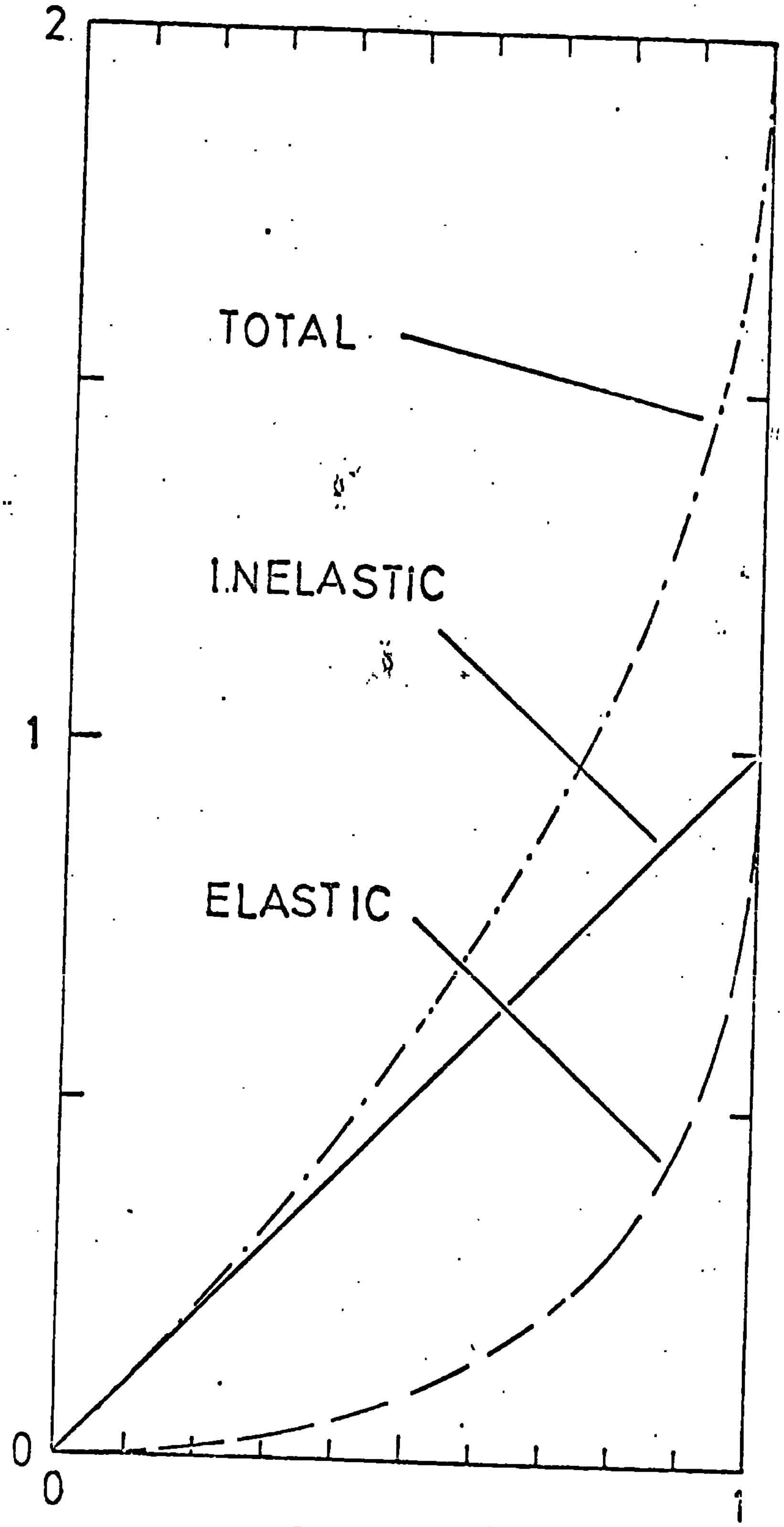

Fig. 28

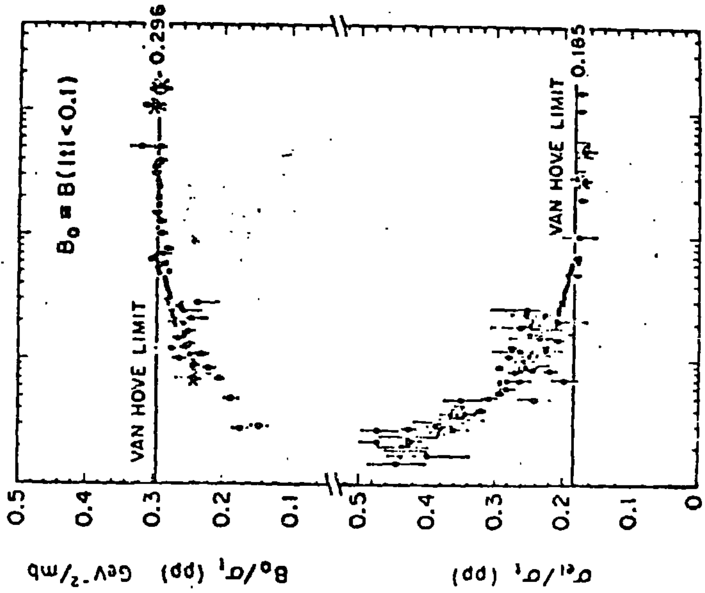
$B_o \equiv B(|t|<0.1)$
VAN HOVE LIMIT
0.296
VAN HOVE LIMIT
0.185
B_o/σ_T (pp) GeV^{-2}/mb
σ_{el}/σ_T (pp)
0.5
0.4
0.3
0.2
0.1
0.5
0.4
0.3
0.2
0.1
0
10^1
10^2
10^3
P_{LAB} (GeV)

Fig. 27

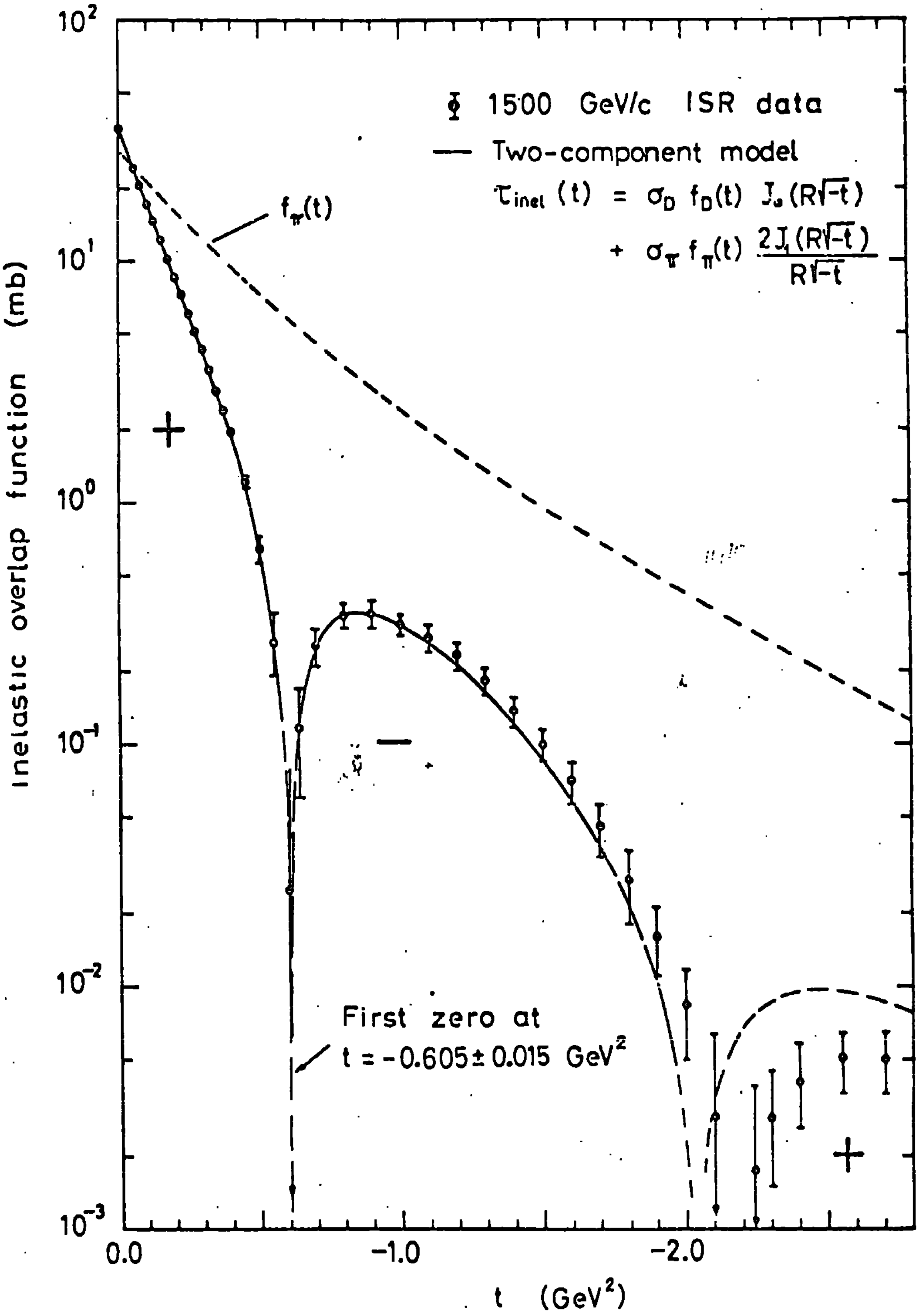
10^2
10^1
10^0
10^{-1}
10^{-2}
10^{-3}
Inelastic overlap function (mb)
0.0
−1.0
−2.0
t (GeV²)
1500 GeV/c ISR data
Two-component model
$\tau_{inel}(t) = \sigma_D f_D(t) J_0(R\sqrt{-t})$
$+ \sigma_\pi f_\pi(t) \frac{2J_1(R\sqrt{-t})}{R\sqrt{-t}}$
$f_\pi(t)$
+
−
+
First zero at
t = −0.605 ± 0.015 GeV²

FIG. 28

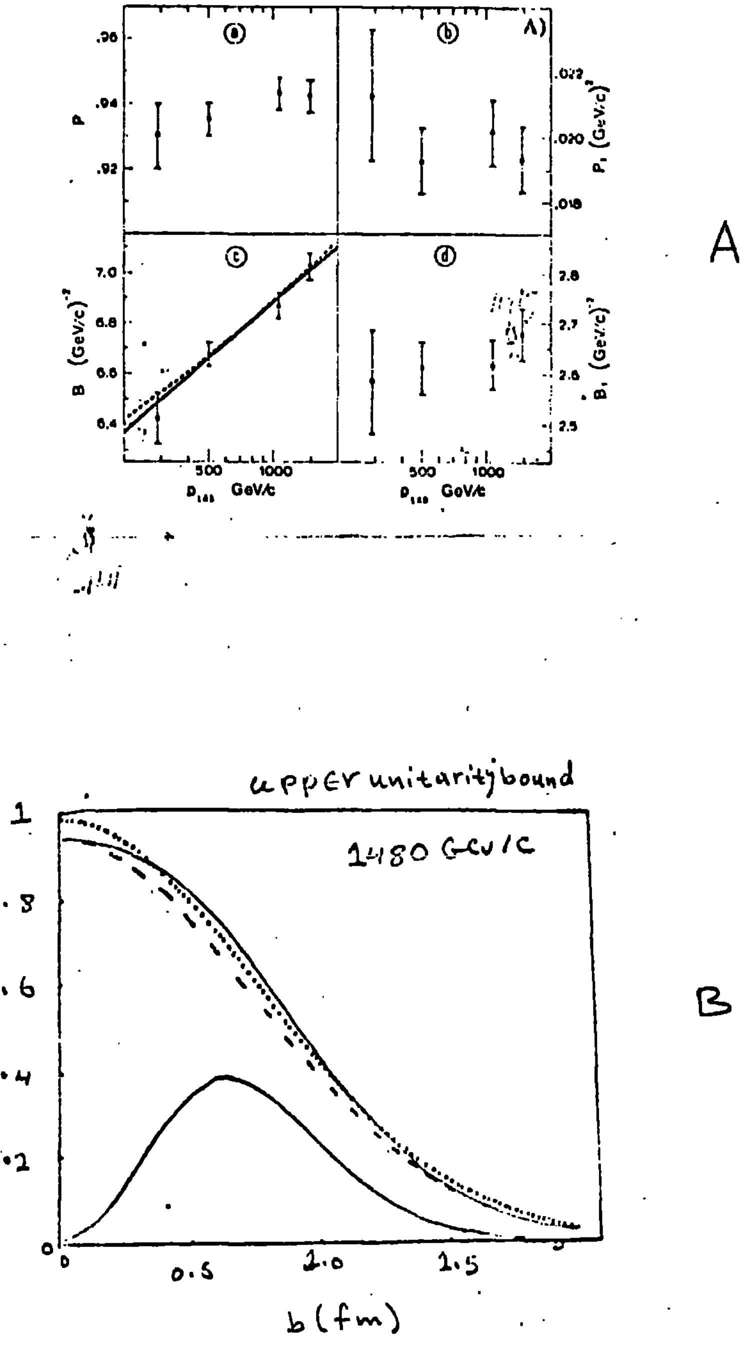
a
b
A)
P
.96
.94
.92
.022
.020
.018
P_1 (GeV/c)^2
c
d
B (GeV/c)$^{-2}$
7.0
6.8
6.6
6.4
B_1 (GeV/c)$^{-2}$
2.8
2.7
2.6
2.5
500
1000
p_{lab} GeV/c
A
upper unitarity bound
1480 GeV/c
1
0.8
0.6
0.4
0.2
0
0.5
1.0
1.5
b (fm)
B

Fig. 29

Fig. 30, A

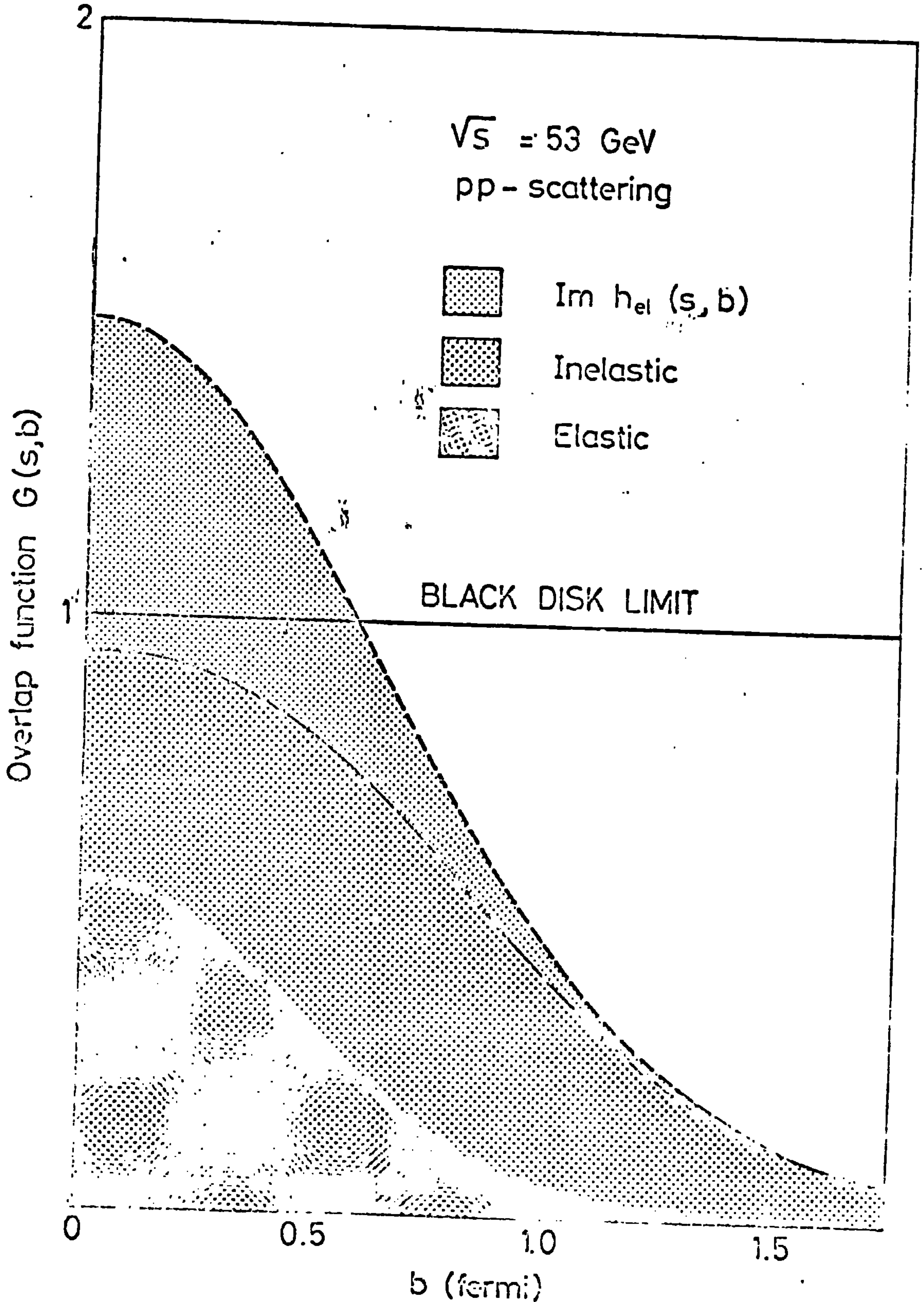

$\sqrt{s}$ = 53 GeV
pp - scattering
▨ Im h_{el} (s, b)
▨ Inelastic
▨ Elastic
BLACK DISK LIMIT
Overlap function G(s,b)
2
1
0
0.5
1.0
1.5
b (fermi)

Fig. 30, B.

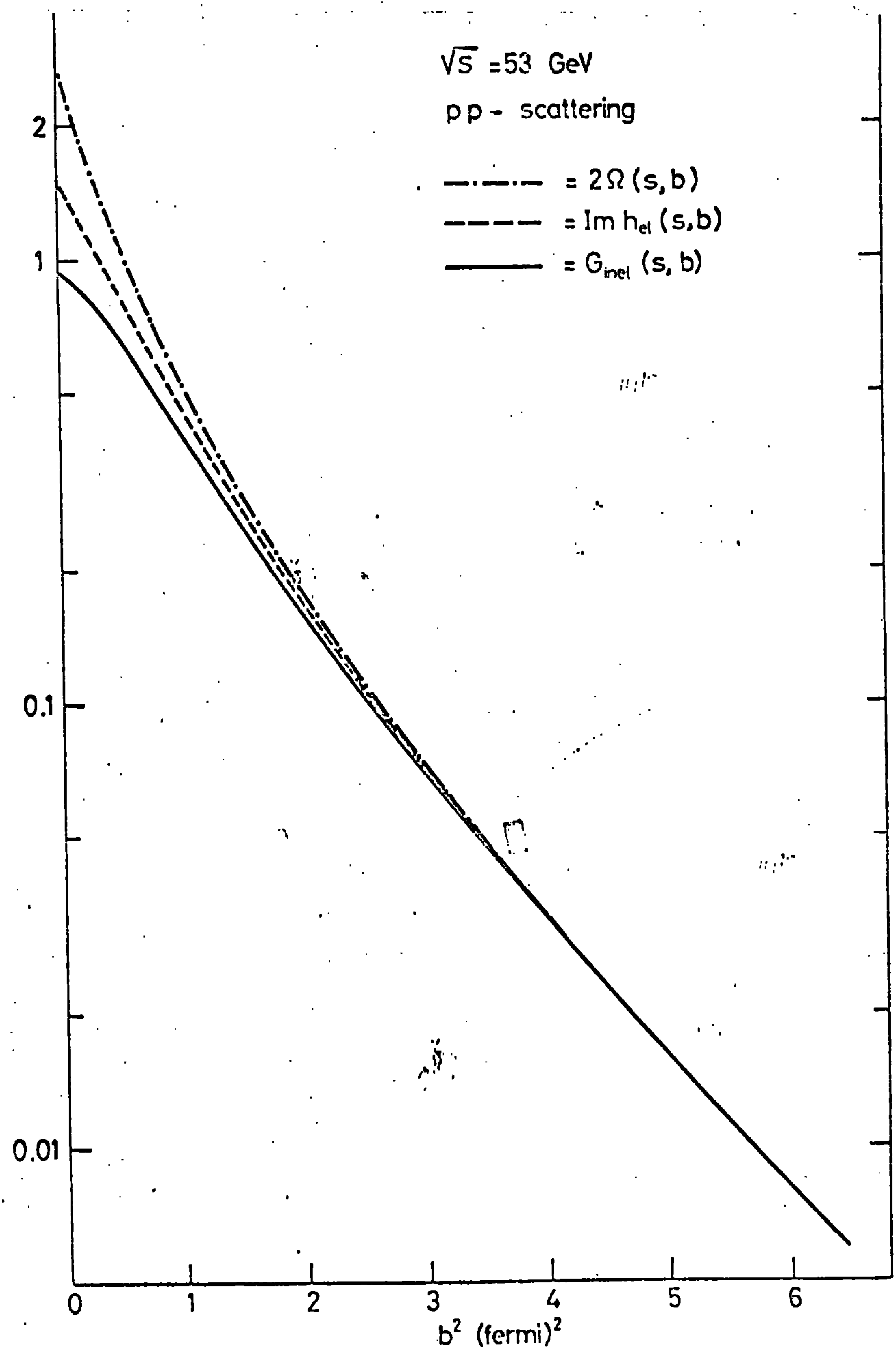
$\sqrt{s}$ =53 GeV
pp - scattering
—·—·— = $2\Omega(s,b)$
– – – – = $\mathrm{Im}\, h_{el}(s,b)$
——— = $G_{inel}(s,b)$
2
1
0.1
0.01
0
1
2
3
4
5
6
b^2 (fermi)^2

Fig. 31

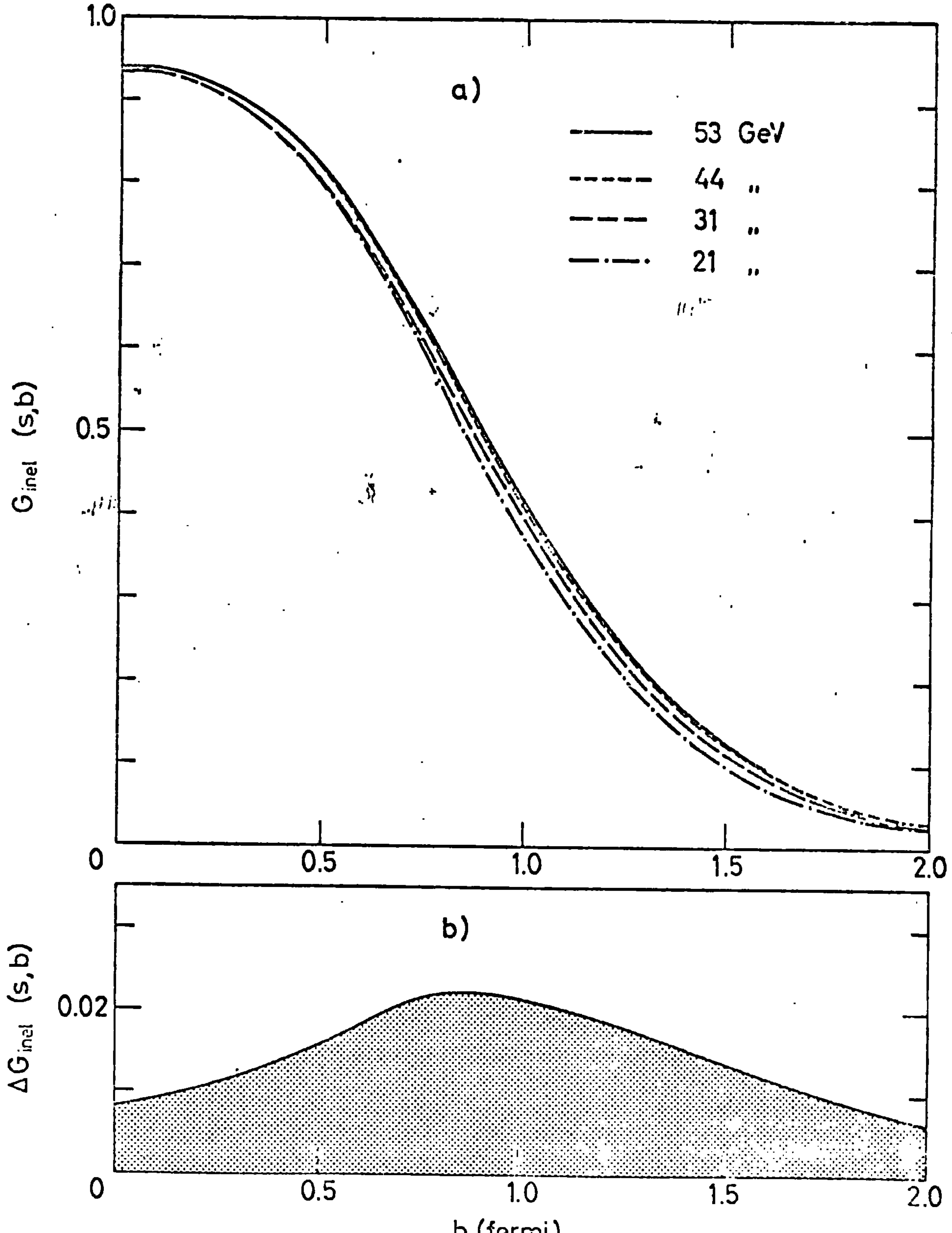
a)
53 GeV
44 "
31 "
21 "
1.0
0.5
0
G_{inel} (s,b)
0.5
1.0
1.5
2.0
b)
0.02
0
ΔG_{inel} (s,b)
0.5
1.0
1.5
2.0
b (fermi)

Fig. 31

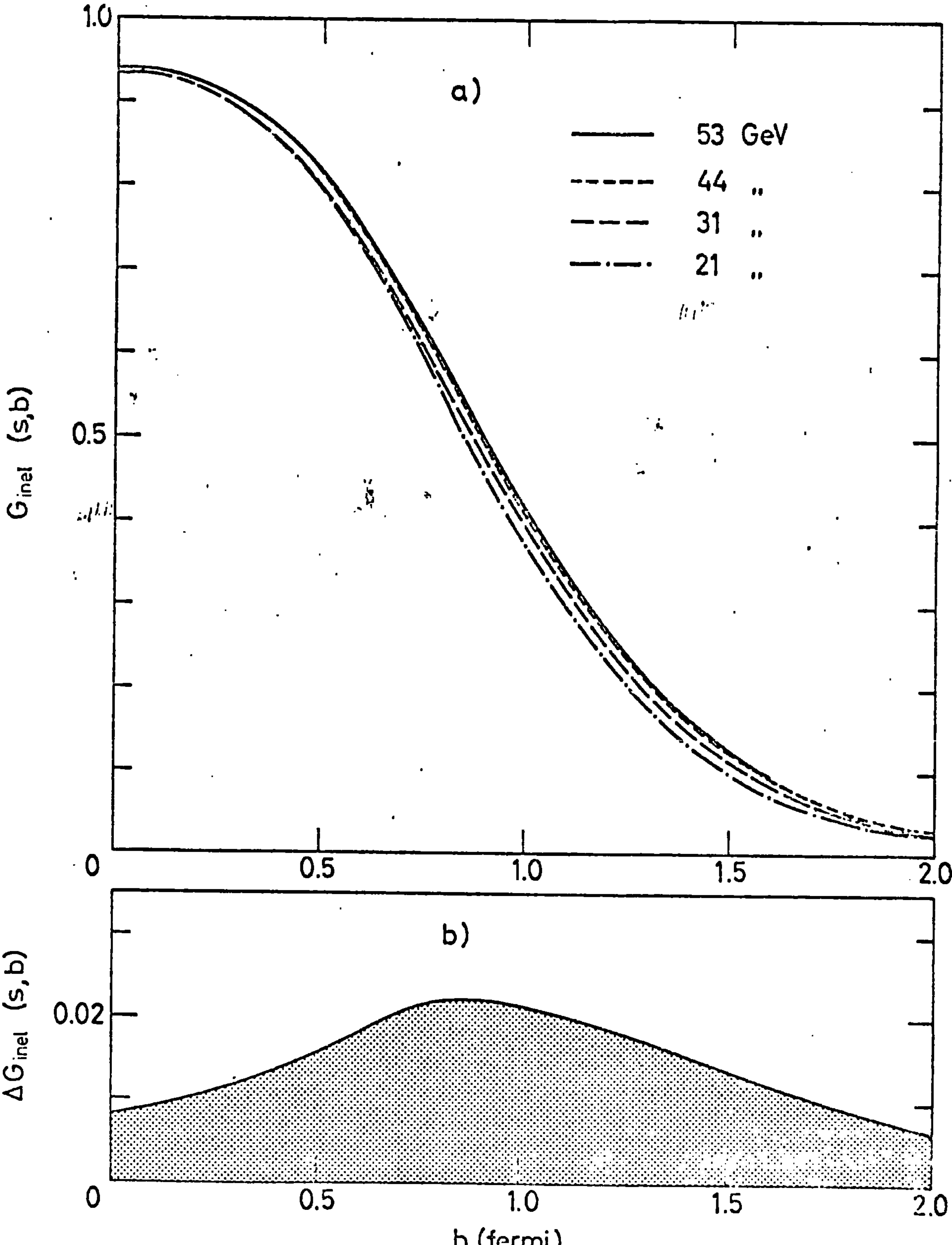
1.0
0.5
0
G_{inel} (s,b)
a)
53 GeV
44 ,,
31 ,,
21 ,,
0.5
1.0
1.5
2.0
b)
ΔG_{inel} (s,b)
0.02
0
0.5
1.0
1.5
2.0
b (fermi)

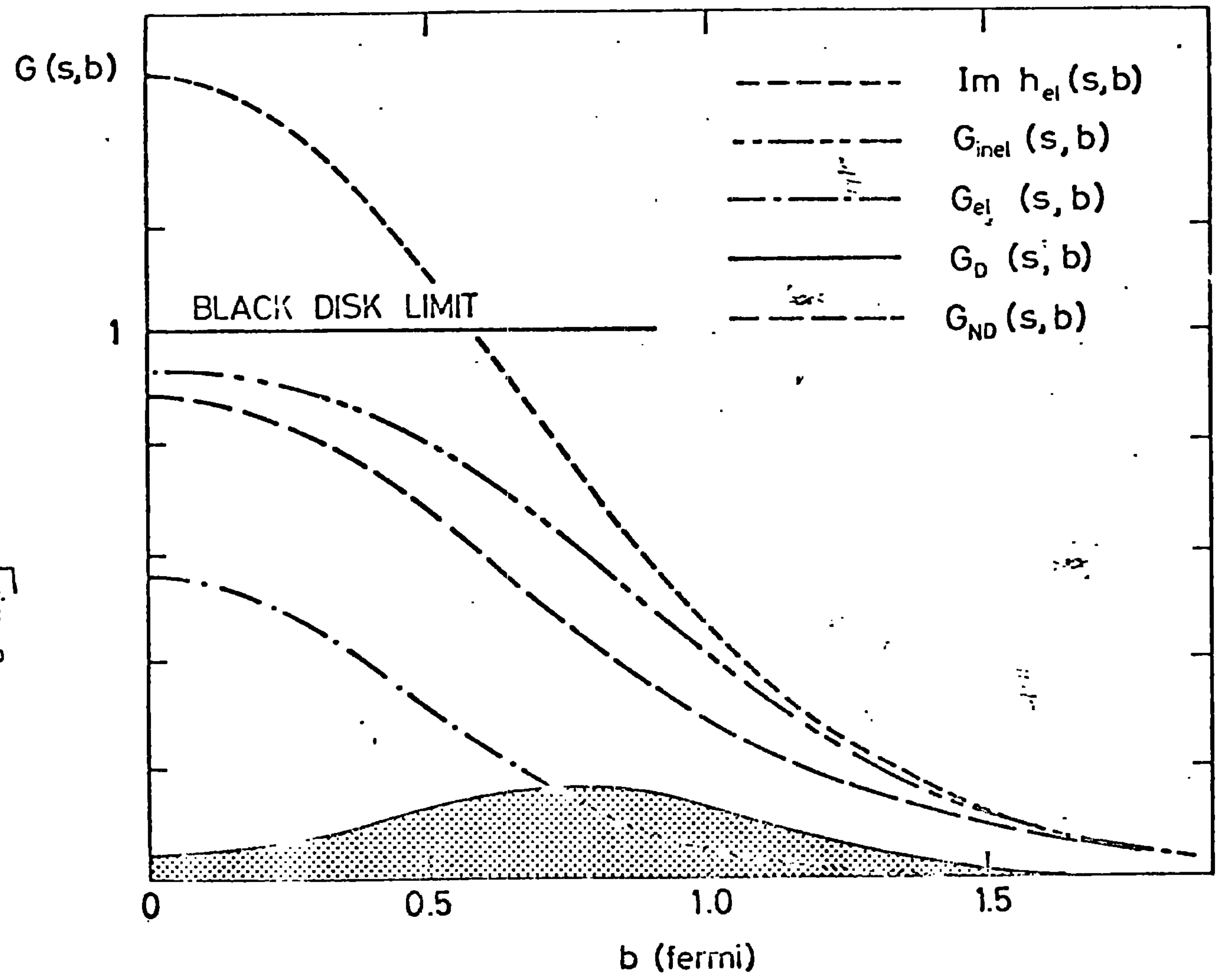
G (s,b)
1
BLACK DISK LIMIT
Im $h_{el}(s,b)$
$G_{inel}(s,b)$
$G_{el}(s,b)$
$G_D(s,b)$
$G_{ND}(s,b)$
0
0.5
1.0
1.5
b (fermi)

Fig. 32

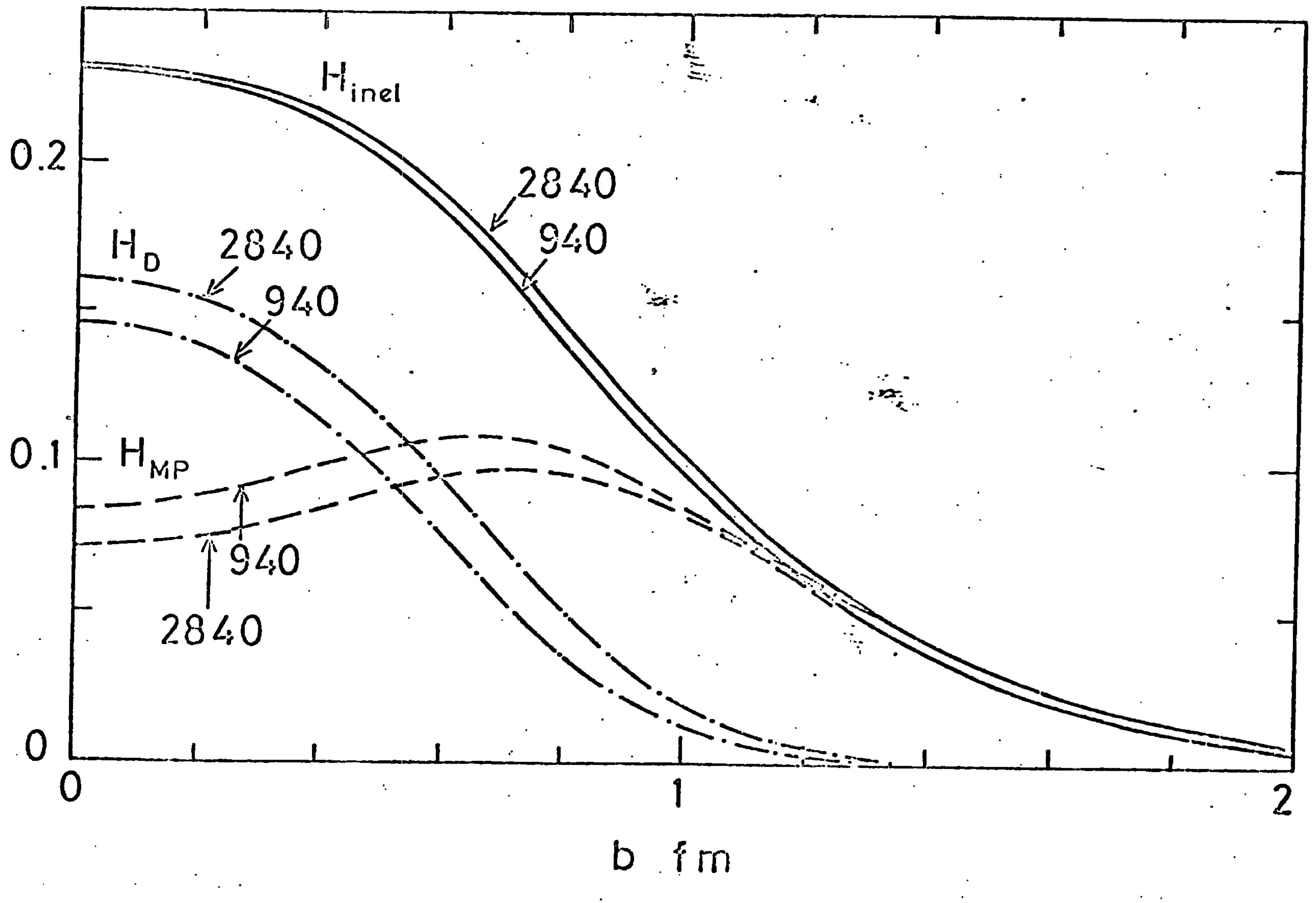

Fig. 33

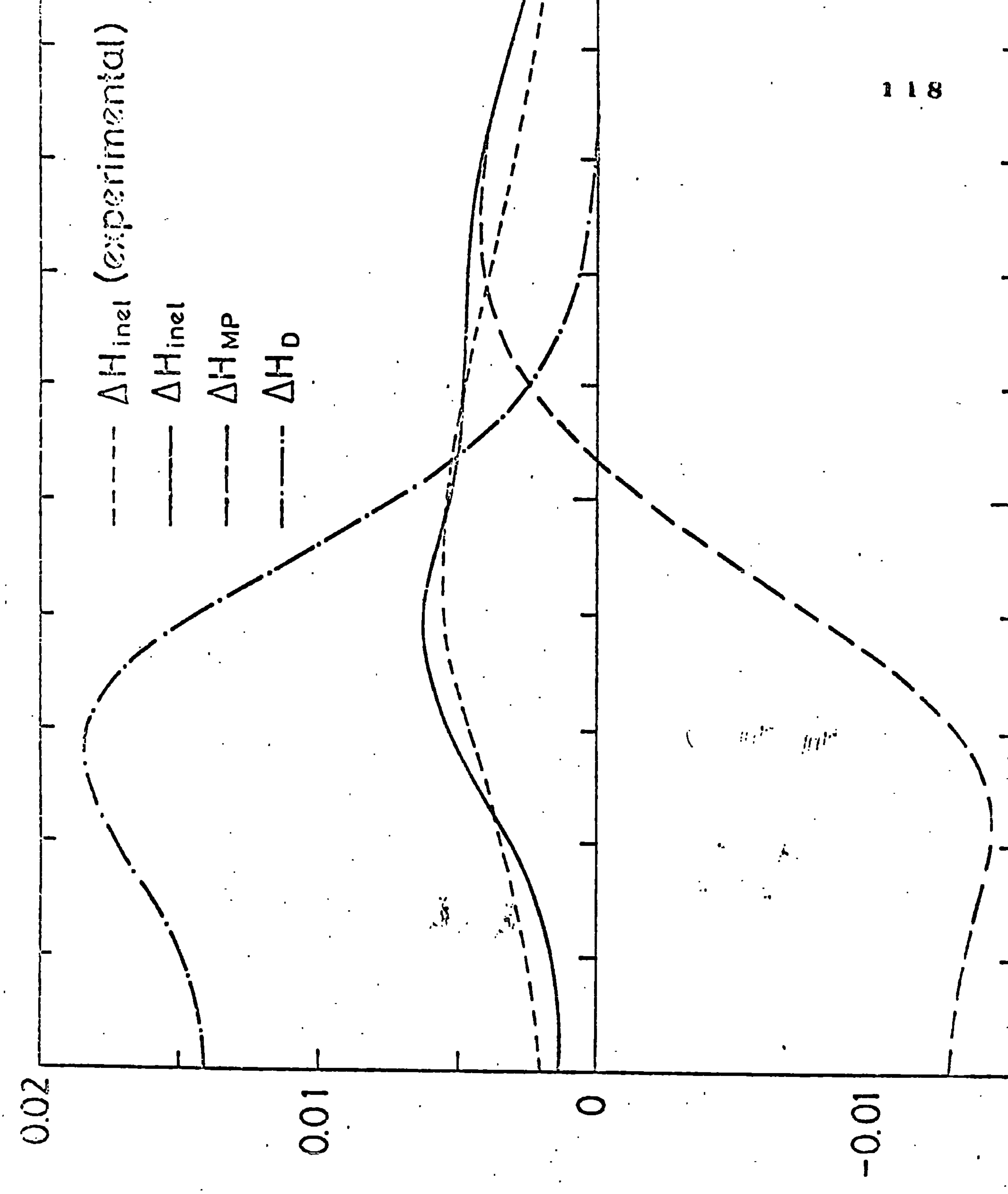

Fig. 34

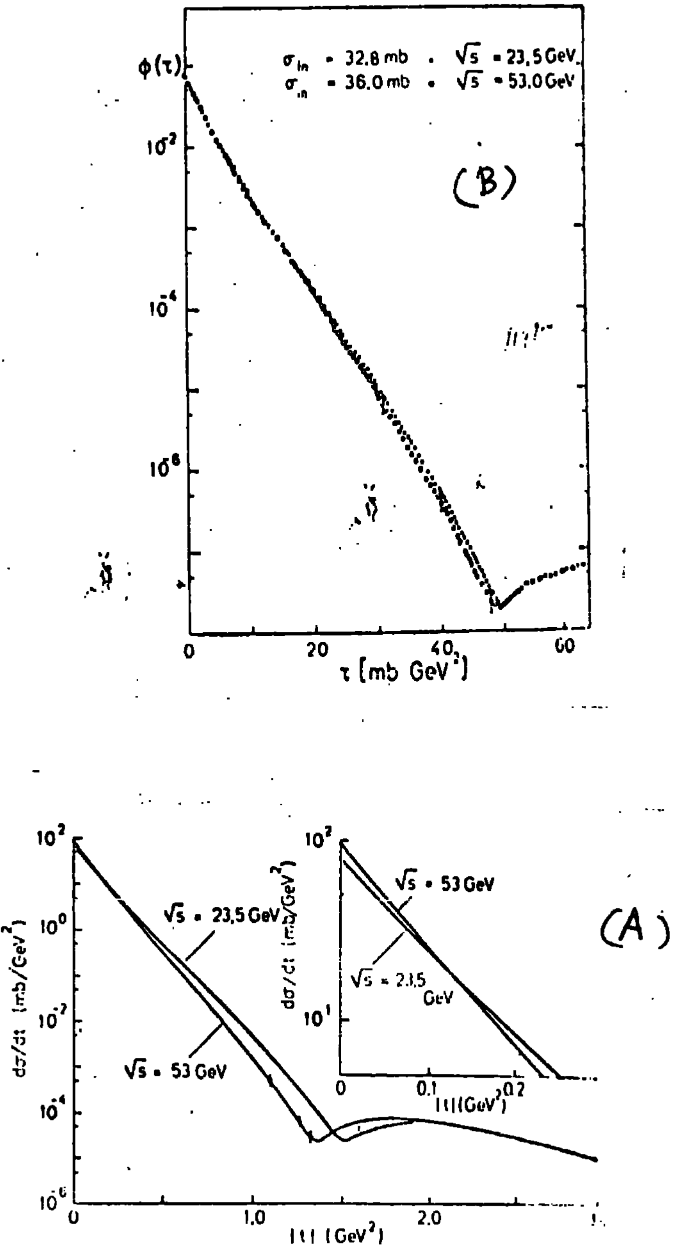
φ(τ)
σ_{in} = 32.8 mb , $\sqrt{s}$ = 23.5 GeV
σ_{in} = 36.0 mb , $\sqrt{s}$ = 53.0 GeV
10^{-2}
10^{-4}
10^{-6}
(B)
0
20
40
60
τ [mb GeV²]
10^2
10^0
10^{-2}
10^{-4}
10^{-6}
dσ/dt (mb/GeV²)
$\sqrt{s}$ = 23.5 GeV
$\sqrt{s}$ = 53 GeV
0
1.0
2.0
|t| (GeV²)
10^2
10^1
dσ/dt (mb/GeV²)
$\sqrt{s}$ = 53 GeV
$\sqrt{s}$ = 23.5 GeV
0
0.1
0.2
|t| (GeV²)
(A)

Fig. 35

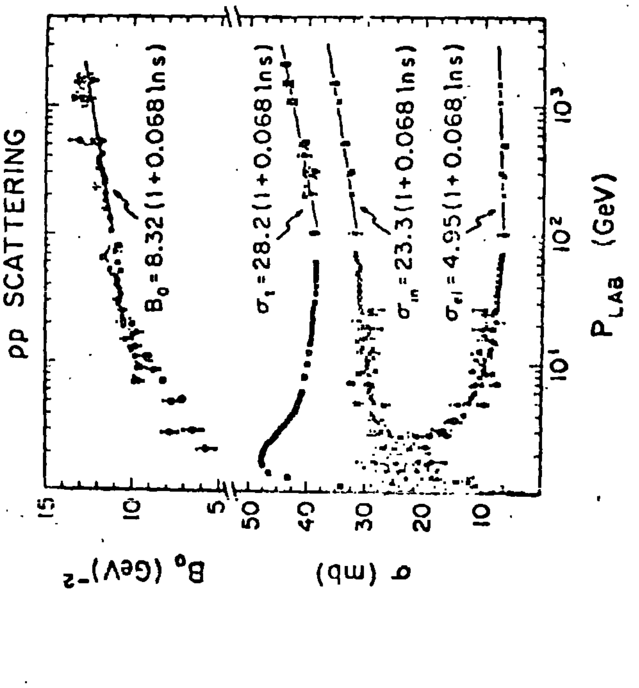
pp SCATTERING
$B_0 = 8.32(1+0.068\ln s)$
$\sigma_t = 28.2(1+0.068\ln s)$
$\sigma_{in} = 23.3(1+0.068\ln s)$
$\sigma_{el} = 4.95(1+0.068\ln s)$
B_0 (GeV)$^{-2}$
σ (mb)
P_{LAB} (GeV)
15
10
5
50
40
30
20
10
10^1
10^2
10^3

Fig. 36

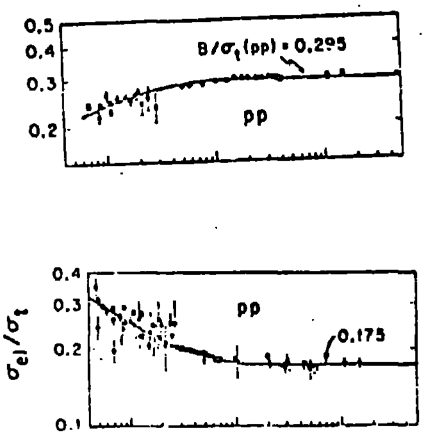
0.5
0.4
0.3
0.2
B/σt(pp) = 0.295
pp
σel/σt
0.4
0.3
0.2
0.1
pp
0.175

Fig. 37

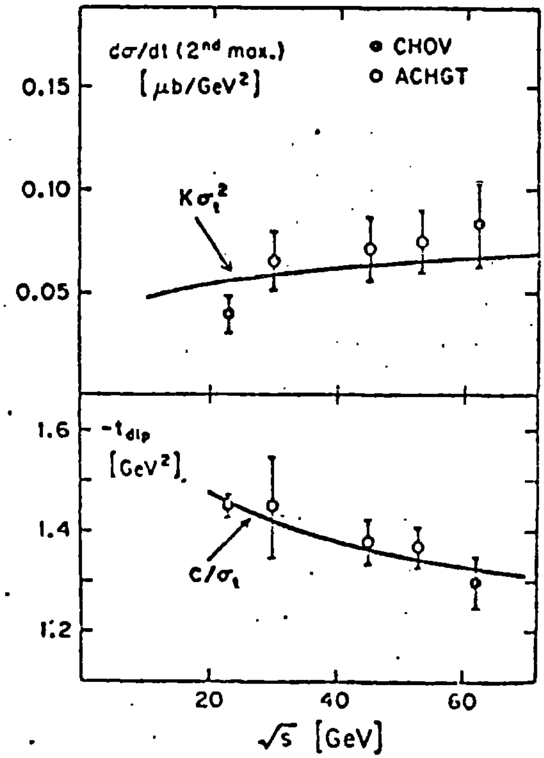
dσ/dt (2nd max.)
[μb/GeV²]
● CHOV
○ ACHGT
0.15
0.10
0.05
Kσt²
-tdip
[GeV²]
1.6
1.4
1.2
c/σt
20
40
60
√s [GeV]

Fig. 38

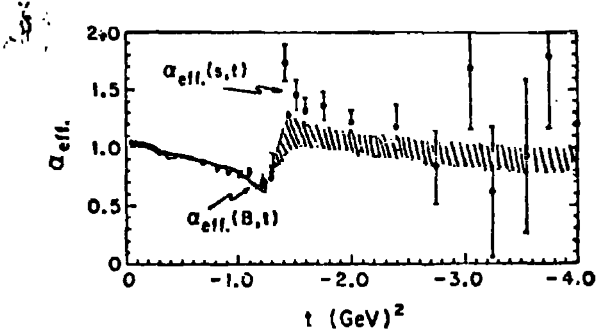

Fig. 1. Effective Regge trajectory α_{eff} as deduced from: (a) the geometric scaling relation of eq. (11)

$$\alpha_{eff}(B,t) - 1 = (1+\tfrac{1}{2}Bt)\frac{d(\ln R^2)}{d(\ln s)},$$

(values denoted by shaded region);

(b) $\alpha_{eff}(s,t) = \frac{\partial}{\partial \ln s}\left(\ln\frac{d\sigma}{dt}\right)$,

(values represented by data points).

Fig. 39

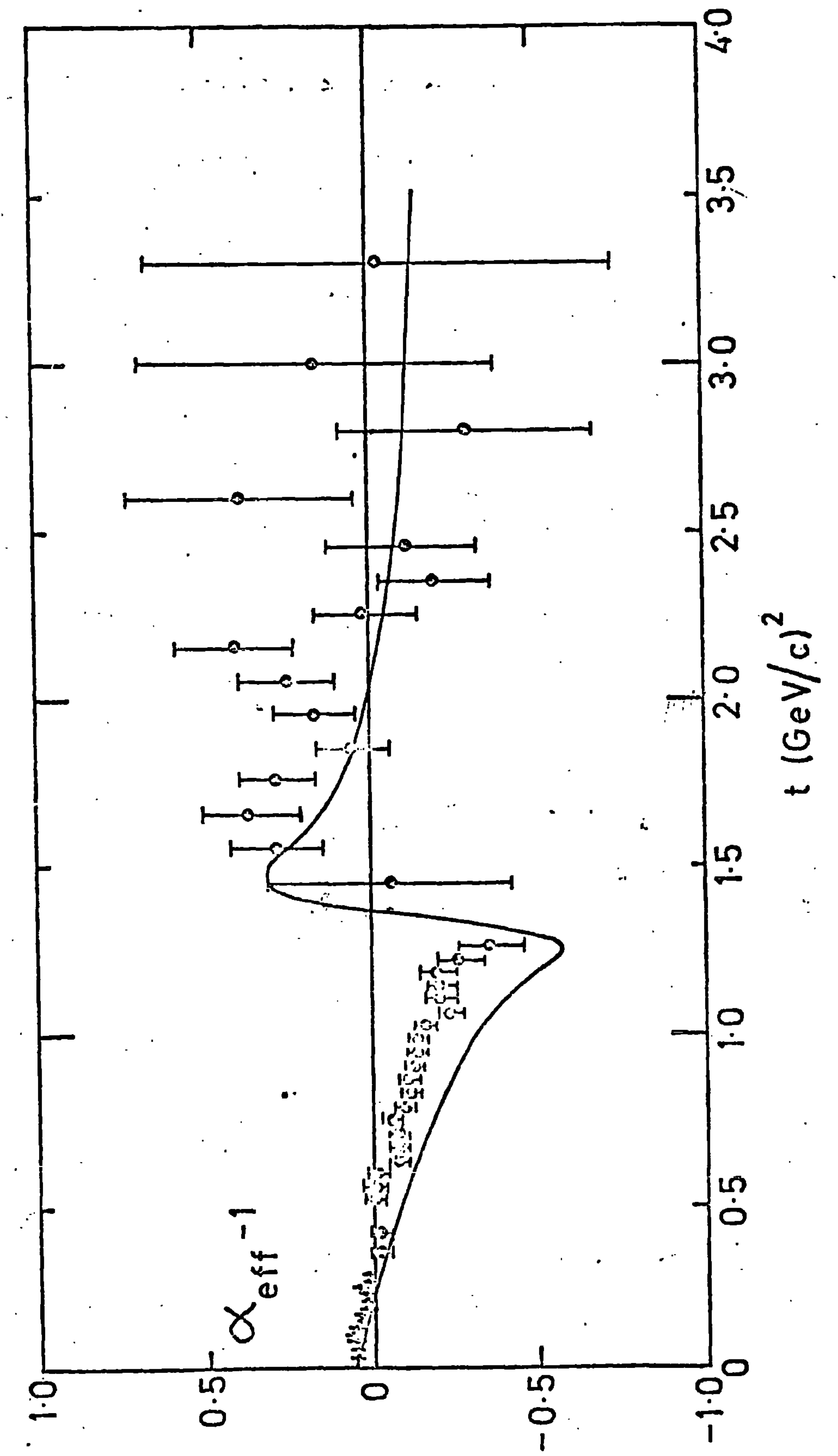

Fig. 40

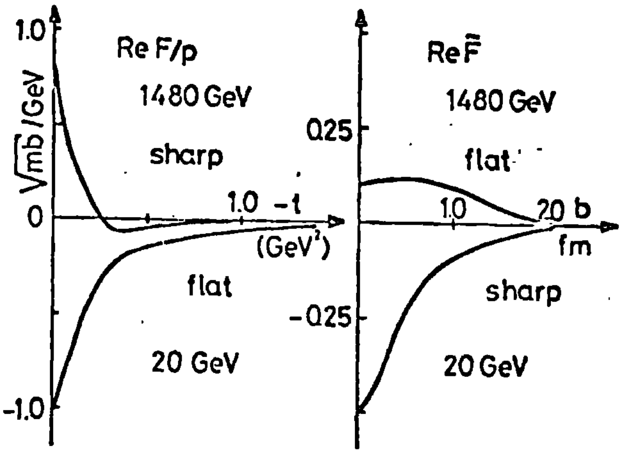
1.0
0
-1.0
√mb /GeV
Re F/p
1480 GeV
sharp
1.0
-t
(GeV²)
flat
20 GeV
Re $\tilde{F}$
1480 GeV
0.25
-0.25
flat
1.0
20 b
fm
sharp
20 GeV

Fig. 41

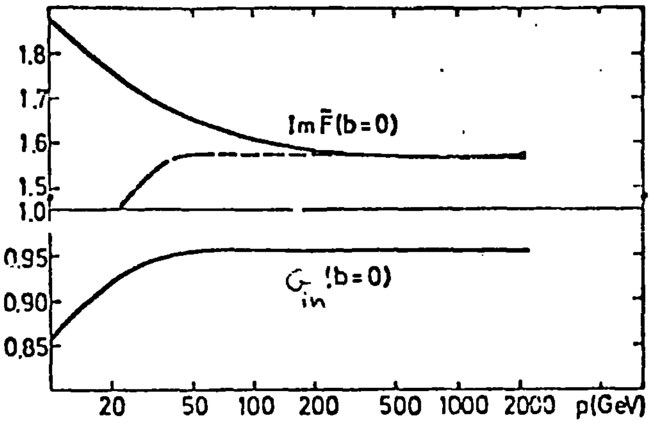
1.8
1.7
1.6
1.5
1.0
0.95
0.90
0.85
Im $\tilde{F}$(b=0)
G_{in}(b=0)
20
50
100
200
500
1000
2000
p(GeV)

Fig. 42

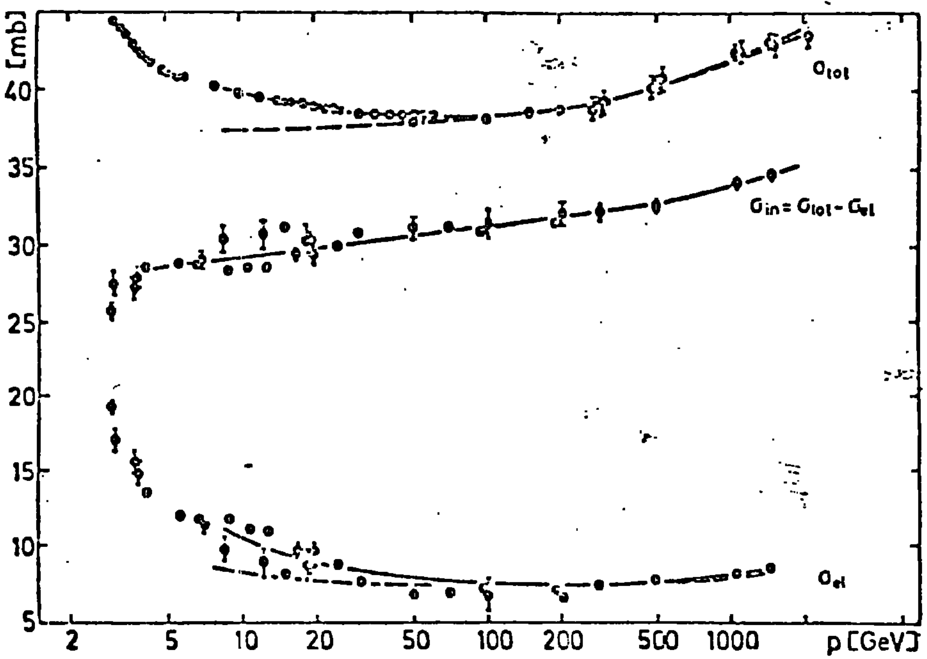
[mb]
40
35
30
25
20
15
10
5
2
5
10
20
50
100
200
500
1000
p [GeV]
σ_{tot}
$\sigma_{in} = \sigma_{tot} - \sigma_{el}$
σ_{el}

Fig. 43

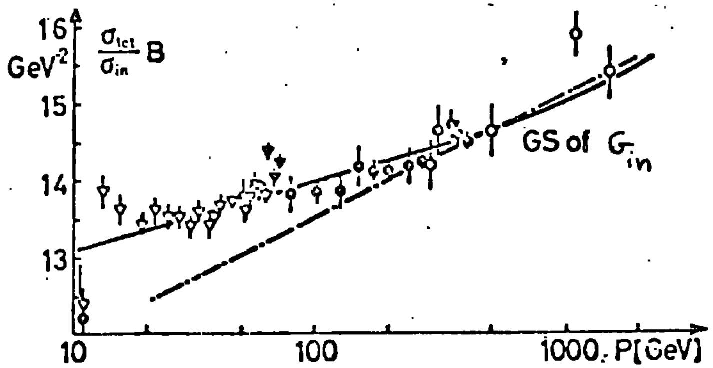
16
GeV^2
15
14
13
$\frac{\sigma_{tot}}{\sigma_{in}}B$
GS of σ_{in}
10
100
1000.
P[GeV]

Fig. 44

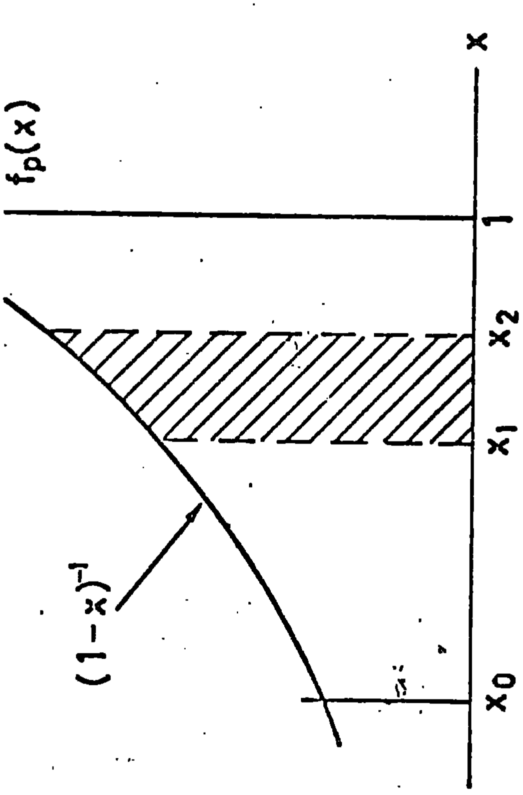

Fig. 45

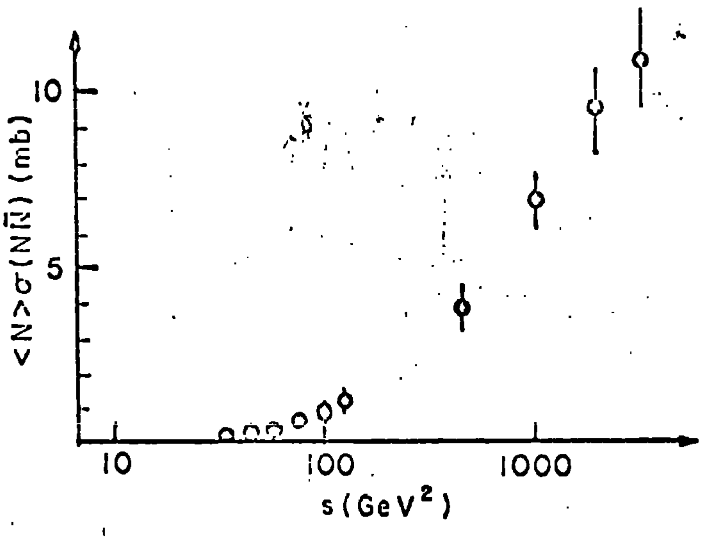

Fig. 46

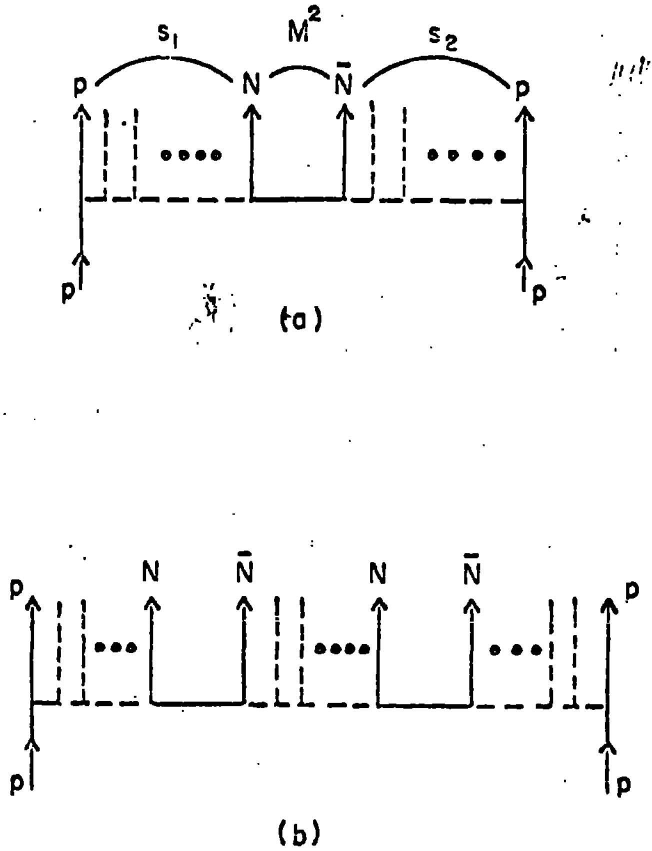
s₁
M²
s₂
p
N
N̄
p
p
p
p
N
N̄
N
N̄
p
p
p

(a)

(b)

Fig. 47

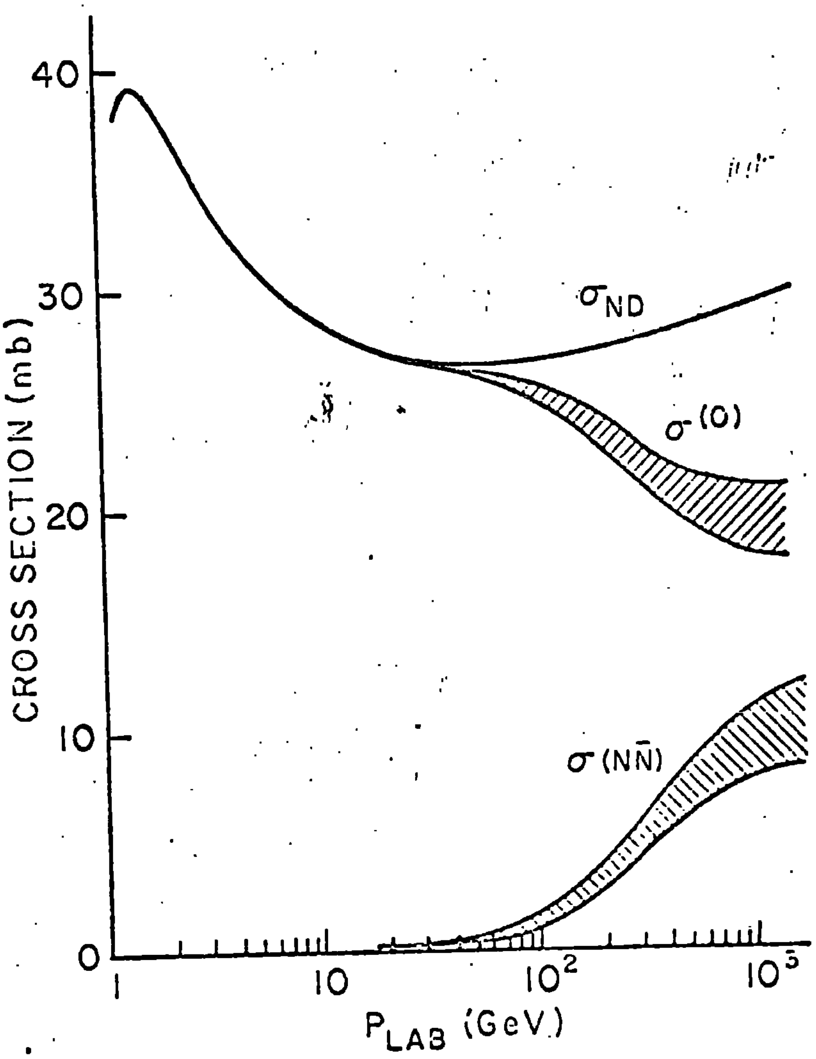
40
30
20
10
0
CROSS SECTION (mb)
σ_{ND}
$\sigma^{(0)}$
$\sigma(N\bar{N})$
1
10
10^2
10^3
P_{LAB} (GeV)

Fig. 48

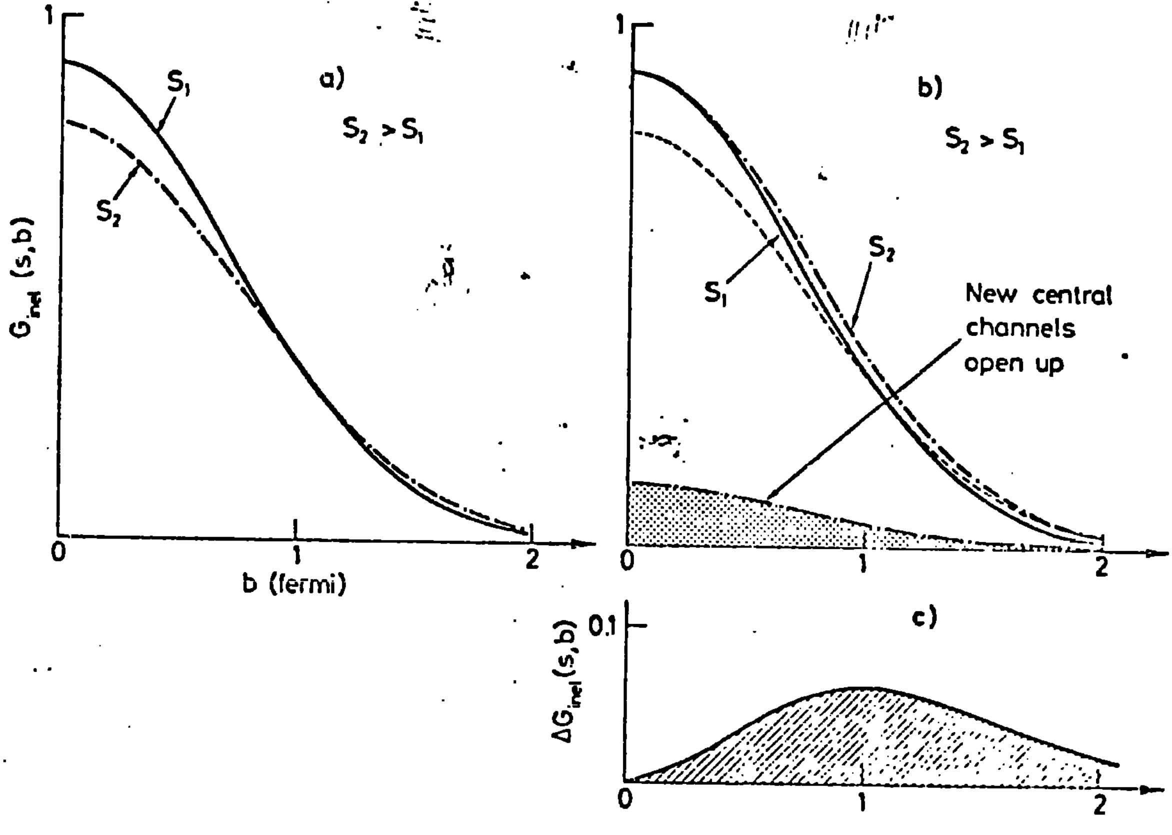
a)
$S_2 > S_1$
S_1
S_2
$G_{inel}(s,b)$
1
0
1
2
b (fermi)
b)
$S_2 > S_1$
S_1
S_2
New central channels open up
c)
$\Delta G_{inel}(s,b)$
0.1

Fig. 49

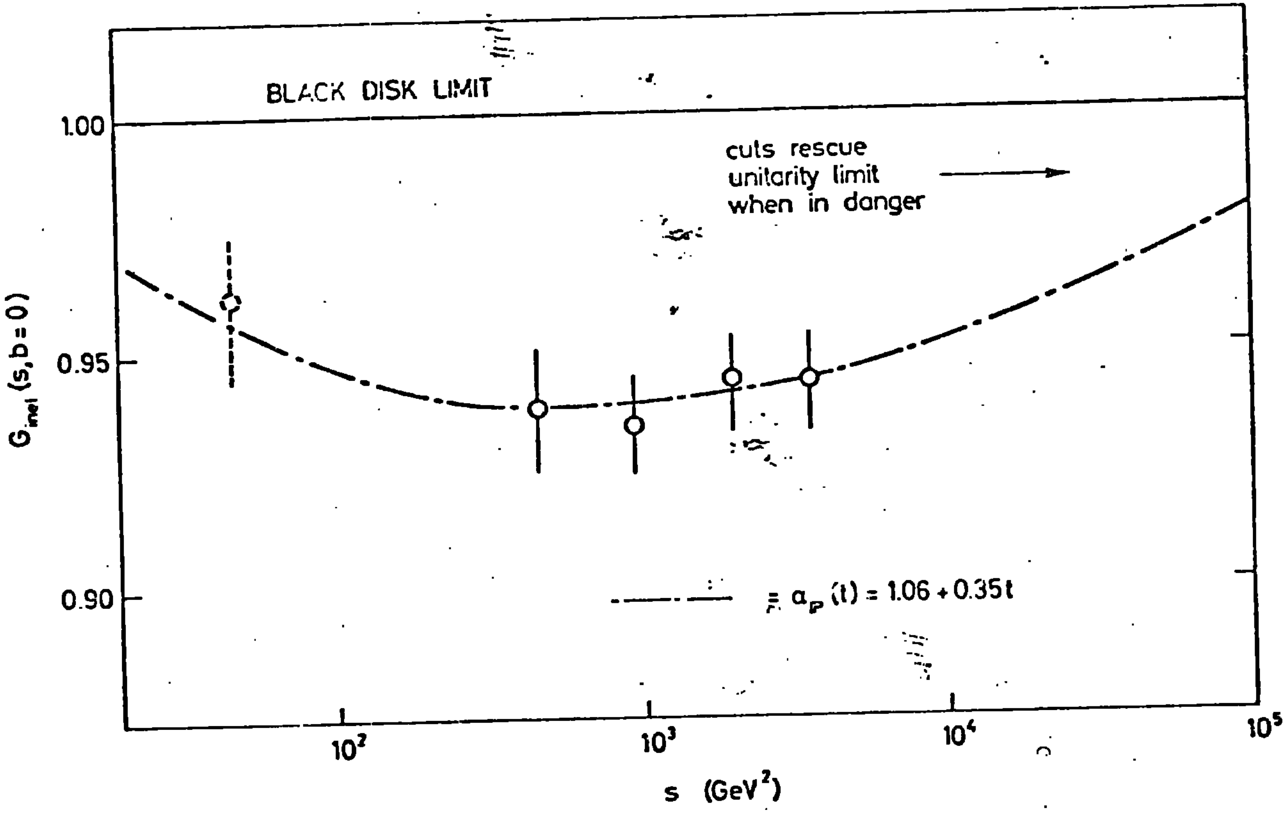

Fig. 50

DURHAM UNIVERSITY
SCIENCE
15 APR 1976
SECTION
LIBRARY